Applied Physics Reviews

REVIEW ARTICLE | JULY 10 2024

Advancements in miniaturized infrared spectroscopic-based volatile organic compound sensors: A systematic review

Special Collection: Volatile Organic Compounds and their Applications

Lipeng Xia ; Yuheng Liu ; Ray T. Chen ; Binbin Weng ; Yi Zou

Appl. Phys. Rev. 11, 031306 (2024)
https://doi.org/10.1063/5.0197236

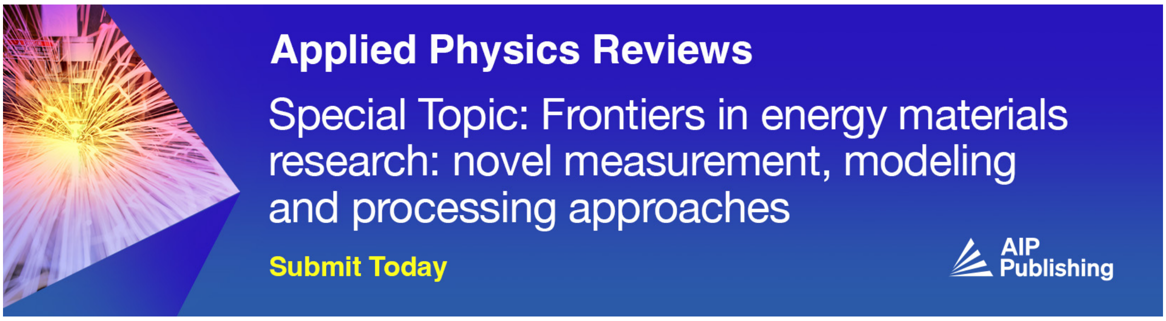

Applied Physics Reviews REVIEW pubs.aip.org/aip/are

Advancements in miniaturized infrared spectroscopic-based volatile organic compound sensors: A systematic review

Cite as: Appl. Phys. Rev. **11**, 031306 (2024); doi: 10.1063/5.0197236
Submitted: 12 January 2024 · Accepted: 7 June 2024 ·
Published Online: 10 July 2024

Lipeng Xia,[1,2,3] Yuheng Liu,[1,2,3] Ray T. Chen,[4] Binbin Weng,[5,a)] and Yi Zou[1,a)]

AFFILIATIONS

[1]The School of Information Science and Technology, ShanghaiTech University, Shanghai 201201, China
[2]Shanghai Institute of Microsystem and Information Technology, Chinese Academy of Sciences, Shanghai 200050, China
[3]University of Chinese Academy of Sciences, Beijing 100049, China
[4]Department of Electrical and Computer Engineering, The University of Texas at Austin, Austin, Texas 78758, USA
[5]School of Electrical and Computer Engineering, University of Oklahoma, Norman, Oklahoma 73019, USA

Note: This paper is part of the APR Special Topic on Volatile Organic Compounds and their Applications.

[a)]**Authors to whom correspondence should be addressed:** binbinweng@ou.edu and zouyi@shanghaitech.edu.cn

ABSTRACT

The global trends of urbanization and industrialization have given rise to critical environmental and air pollution issues that often receive insufficient attention. Among the myriad pollution sources, volatile organic compounds (VOCs) stand out as a primary cluster, posing a significant threat to human society. Addressing VOCs emissions requires an effective mitigation action plan, placing technological development, especially in detection, at the forefront. Photonic sensing technologies rooted in the infrared (IR) light and matter interaction mechanism offer nondestructive, fast-response, sensitive, and selective chemical measurements, making them a promising solution for VOC detection. Recent strides in nanofabrication processes have facilitated the development of miniaturized photonic devices and thus sparked growing interest in the creation of low-cost, highly selective, sensitive, and fast-response IR optical sensors for VOC detection. This review work thus serves a timely need to provide the community a comprehensive understanding of the state of the art in this field and illuminate the path forward in addressing the pressing issue of VOC pollution.

TABLE OF CONTENTS

I. INTRODUCTION

A. Definition and features of VOCs

Volatile organic compounds (VOCs) constitute a subset of organic compounds characterized by high vapor pressure and low water solubility. This diverse group encompasses hydrocarbons, aromatic hydrocarbons, alcohols, ketones, ethers, halogenated hydrocarbons, nitrogen-based compounds, and so on. Different definitions for VOCs exist across countries and organizations. The United States (U. S.) Environmental Protection Agency (EPA) describes VOCs as organic compounds participating in atmospheric photochemical reactions, excluding carbon monoxide, carbon dioxide, carbonic acid, metallic carbides or carbonates, and ammonium carbonate.[1] The European Environment Agency (EEA) defines VOCs as organic chemical compounds that, under normal conditions, are gaseous or can vaporize and enter the atmosphere.[2] For the sake of this introduction, the infrared (IR) sensors discussed in this article are those monitoring organic compounds that evaporate or vaporize under normal atmospheric conditions of temperature and pressure.

The comprehensive overview provided in Fig. 1 highlights the myriad sources of VOCs, underscoring their diverse origins arising from both natural processes and various human activities in contemporary society.[3] In natural processes, organisms release a diverse array of VOCs as a result of metabolic activities, playing a crucial role in facilitating interactions with the environment. In plants, there are four significant VOC biosynthetic pathways: shikimate/phenylalanine, mevalonic acid, methylerythritol phosphate, and lipoxygenase pathways. These pathways give rise to the emission of various VOC classes, including benzenoids/phenylpropanoids, sesquiterpenes, monoterpenes, hemiterpenes, diterpenes, volatile carotenoid derivatives, and methyl jasmonate/green leaf volatiles.[4] These emissions serve various functions, such as attracting pollinators and seed dispersers, as well as protecting against pathogens, parasites, and herbivores.[5] For instance, sage plants exhibit an increased release of terpenes at elevated temperatures.[6] Furthermore, the co-occurrence of multiple stressors or threats can directly or indirectly impact VOC emissions.[7] Humans, too, contribute to VOC emissions, releasing numerous odorous and non-odorous compounds influenced by lifestyle, age, or medical conditions. Common sources of human VOC emissions include breath, feces, and bodily secretions. For example, individuals with different diseases emit distinctive VOCs, such as acetone in the case of diabetes,[8] mercaptans associated with liver disease,[9] dimethylamine and trimethylamine in instances of uremia,[10] and alkanes indicative of lung cancer.[11] These emitted VOCs provide unique "odor-fingerprints," holding potential for applications in health monitoring.[12]

Apart from natural processes, human activities in both industrial production and daily life contribute significantly to VOC emissions. The combustion of biomass fuels is a notable contributor to alkane emissions.[13] For instance, in the pursuit of multiple growing seasons and pest control, farmers find open-burning rice straw an appealing practice. However, these uncontrolled burning events unavoidably release vast pollutants, including polycyclic aromatic hydrocarbons.[14] Similarly, fossil fuels contribute to alkane release through incomplete combustion and fuel evaporation in automobiles.[13] Beyond combustion, the production processes of various industrial raw materials, such as crude oil, gas, paint solvent, and metals, result in the release of VOCs. In the realm of oil and gas exploration and extraction, a range of hydrocarbons, including methane and n-hexane, is emitted throughout the production, transportation, processing, and storage phases.[15] Post-production, the utilization of materials like those used in automobile painting releases aromatic hydrocarbons, alcohols, glycol ether, ketones, and esters.[16] Furthermore, routine activities like cooking, painting, and cleaning in everyday life also contribute to heightened indoor VOC levels.[17]

While not all VOCs directly contribute to environmental pollution, they play a role in atmospheric photochemical reactions, leading to the generation of secondary pollutants. Oxidized VOCs can form

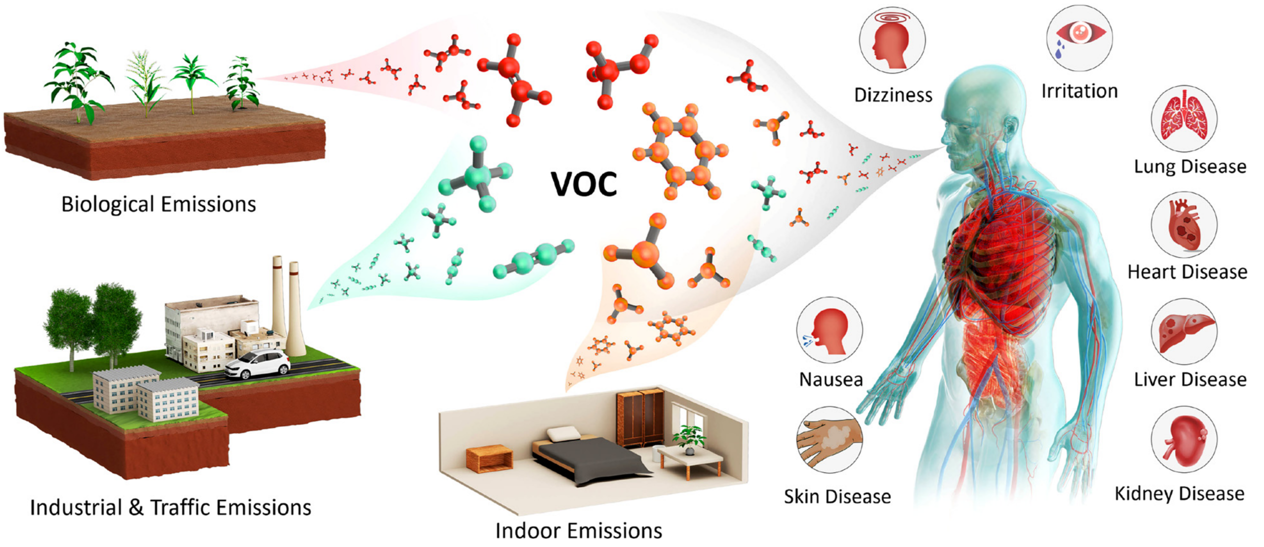

FIG. 1. Schematic illustration of VOC emission sources and associated health hazards. Natural processes, incomplete combustion of fuels, and decorative materials contribute significantly to VOC emissions. Some VOCs actively participate in photochemical reactions, generating secondary pollutants, while others directly pose health risks to humans. Both types of pollutants have detrimental effects on both human health and the environment.

secondary organic aerosols, contributing to ground-level ozone and NO_2 production, crucial components of photochemical smog.[18] Some VOCs, such as aromatic compounds and ketones, pose health risks, particularly in indoor environments.[13] The total volatile organic compounds (TVOCs) are commonly used as a sum parameter for assessing indoor air quality.[19,20] According to the EEA definition, most non-methane VOCs (NMVOCs) are toxic gases present in the air.[21] Table I outlines VOC emission sources, atmosphere lifetimes, and hazards to human health. Indoor exposure to NMVOCs can lead to various effects, including ocular, nasal, and pharyngeal irritation, headaches, dizziness, nausea, allergic skin reactions, and potential harm to the liver, kidneys, and central nervous system.[22] Furthermore, it can increase susceptibility to certain types of cancer.

As a primary cluster of pollution sources, governments have taken proactive measures by enacting legislation to regulate VOC emissions. These measures include implementing process modifications and installing air pollution control equipment. Simultaneously, the identification of pollution sources and the precise detection of VOC levels stand as crucial prerequisites for effectively managing VOC discharge. In this context, VOC sensors play an indispensable role, serving as vital tools for collecting essential information in the pursuit of environmental control and regulation.

B. Miniaturization background for VOC detection

Accurate information regarding VOCs, encompassing their types and concentrations, holds significant value across diverse applications. Governments are increasingly focused on the detection of toxic VOCs in wastewater as part of comprehensive environmental monitoring initiatives. Understanding VOC concentrations from industrial and vehicular sources is critical to preventing their harmful reactions with nitrogen oxides or ozone. Additionally, in the oil and gas industries, VOC sensors play a pivotal role in detecting combustible gases, mitigating the risk of leaks, and enhancing the safety of transportation.

Beyond safety considerations, certain VOCs serve as crucial indicators in various applications. For instance, the concentration of VOCs in breath samples is utilized as biomarkers for diagnosing metabolic states in healthcare.[24] In production processes, monitoring VOC concentrations is essential to ensure product quality, as seen in applications like fruit ripening.[25] Consequently, the need to monitor VOC components and concentrations is undeniable, leading to a consistent increase in the demand for VOC sensors year by year. In 2022, the global VOC gas sensor market size reached approximately 154.1×10^6 U.S. dollars, experiencing robust growth with a compound annual growth rate (CAGR) of approximately 5.3%.[26]

Despite the diversity array of VOC sensor types available for commercial use, the performance assessment indicators for these sensors exhibit fundamental similarities. Therefore, before delving into detailed introductions, it is essential to understand the following key and common indicators of VOC sensors: limit of detection (LOD), sensitivity, selectivity, response time, and robustness. Understanding these indicators is crucial for evaluating the effectiveness of VOC sensors across various applications and ensuring their reliability in providing accurate and timely data.

The limit of detection (LOD), also referred to as the minimum detection limit in certain literature, serves as a key indicator of sensor performance, signifying the lowest concentration or quantity of a substance detectable by the analyte.[27] LOD is typically expressed in common units such as parts per million (ppm), parts per billion (ppb), and parts per trillion (ppt), occasionally adapting other forms like parts per million per volume (ppmv) when considering the detection volume. The determination of LOD and its corresponding integration time rely on the correlation nature with the signal integration process, often derived using the Allan deviation, represented as follows:[28]

$$\sigma_A^2(\tau) = \frac{1}{2(K-1)} \sum_{k=1}^{K-1} \left(\bar{y}_{k+1}(\tau) - \bar{y}_k(\tau)\right)^2, \tag{1}$$

where σ_A is the Allan deviation, K is the total number of time series, and $\bar{y}_k(t)$ denotes the average concentration within the time interval of τ of the time series at k.

Sensitivity is a critical aspect of sensor performance, represented by the calibration curve showcasing the average measured signals concerning concentration.[29] When utilized as a gauge for sensor performance, "sensitivity" specifically refers to the slope of the analytical calibration curve.[27] It also denotes the smallest concentration variation that can be considered a credible change in the measured signal. Sensitivity is expressed in various units, such as "dB/ppm"[30] in absorption spectroscopy to signify the change in light intensity due to analyte absorption and "nm/ppm"[31] in interferometry techniques to record the resonance wavelength shift caused by variations in background

TABLE I. Characteristic sources and hazards of selected VOCs. Data sourced from the World Meteorological Organization (WMO)[23] and the National Institute for Occupational Safety and Health (NIOSH).[22]

VOCs	Atmospheric lifetime (approx.)	Characteristic sources	Daily exposure limit (ppm)	Hazard
Acetylene	15 days	Vehicular emission, biomass burning	2500 (<15 min)	Asphyxia
Propane	11 days	Liquefied Petroleum Gas (LPG), Natural gas	1000	Asphyxiation
Benzene	10 days	Industrial and vehicle emissions, biomass burning	0.1	Cancer (leukemia)
Butane	5 days	Vehicle emissions, LPG	800	Drowsiness and other narcotic effects
Ethanol	4 days	Plants, biofuel	1000	Eye, respiratory, and skin irritation
Pentane	3 days	Vehicle emissions, gasoline evaporation	120	Skin and nervous system effects
Toluene	2 days	Solvents, vehicle emissions	100	CNS depression
Formaldehyde	1 day	VOC oxidation, biomass burning	0.016	Nasal cancer

refractive indices. Distinguishing itself from "LOD," sensitivity requires concurrent consideration of both sensitivity and noise level to accurately characterize sensing system performance, akin to the role of LOD. For example, at the same sensitivity, a lower signal-to-noise ratio (SNR) results in a higher LOD. However, at the same SNR, higher sensitivity may not alter the LOD, as it could also lead to increased noise levels. Sensitivity serves as an indicator of signal strength in data processing, yet it alone cannot fully signify system performance.

Selectivity is the capability of sensors to distinguish specific species from others. In refractive-index-based optical sensors, the properties of waveguides guiding light may undergo changes when exposed to various analytes, exhibiting poor selectivity.[29,32] To enhance this performance, it is common to employ intermediate chemical absorption transducers. These transducers, such as PDMS,[33] PMMA,[34] zeolites,[35] and polyethylene,[36] possess the ability to selectively trap analyte molecules, thereby improving differentiation in the response signal. In absorption-based optical sensors, the interaction between light and analytes relies on absorbance information at specific wavelengths. These sensors inherently boast excellent selectivity by carefully selecting different absorption transitions of analytes at specific wavelengths and controlling the bandwidth of the operating light source.

Response time, defining the duration from sensor exposure to the analyte to the output of the corresponding concentration-dependent electrical signal,[37] is primarily determined by the sensing principle and device structures employed by the sensor. A shorter response time is generally beneficial for real-time continuous monitoring, preventing the risk of missing critical information due to delayed detection.[32] However, a longer integration time is often necessary simultaneously to achieve a better SNR for more accurate sensing results, indicating a clear trade-off in practical application. Additionally, recovery time is another crucial time-related indicator, representing the duration for sensors to return to the initialization state.[32] This is particularly significant for sensors with absorption transducers, as the material properties of the sensing layers, influencing both recovery and response time, play a pivotal role.

Robustness is another critical and comprehensive feature of sensors, necessitating evaluation considering both external factors, such as temperature and humidity, and internal factors, like the nonlinear response of sensor components,[29] or sensor failure. External influences, including fluctuations in background temperature and humidity, can lead to the measurement instability. Variations in temperature may impact circuit or sensor resistance, and in resonance structures, temperature fluctuations can cause shifts in resonance frequencies. Humidity changes can influence detection intensity, particularly in methods like IR spectroscopy, where water molecules' IR absorption occurs within specific wavelength ranges. Additionally, the nonlinear response of sensors can introduce complexities in calibration processes.[29] To enhance sensor robustness, researchers have developed various solutions, including dual-wavelength configurations,[38] redundant sensor arrays,[39] and algorithm mitigation.[40]

Beyond these performance indicators, factors like cost and lifetime exert direct or indirect influences on the commercial utilization of these sensors. Moreover, size has gained increasing significance in sensor selection. We compare some commercial available sensors in Table II. In the context of the Internet of Things (IoTs), miniature, lightweight, and energy-efficient VOC sensors are more appealing than bulk VOC sensor systems.[41] Deploying numerous miniaturized VOC sensors strategically across various production sites and supply chains enhances feedback efficiency. Wearable and implantable sensors have gained popularity due to their ability to offer precise and continuous monitoring of various physiological parameters. Integrating miniaturized VOC sensors into wearable and implantable devices provides a nondestructive and convenient means to monitor disease-related VOC signals. Consequently, the combined assessment of these factors makes metal-oxide-semiconductor (MOS) VOC sensors, IR-based VOC sensors, and photo-ionization VOC sensors the primary choices for VOC detection.[26] MOS-based VOC sensors, the most common type of field effect transistor (FET) sensors, are highly favored in the industry for their compact size, affordability, and ease of integration. However, their selectivity remains a limiting factor when analyzing multiple components. Additionally, achieving results often requires high working temperatures during sensing. On the other hand, photo-ionization VOC sensors exhibit exceptionally low LOD in specific scenarios. Commercial photo-ionization sensors, with compact and portable designs, are advantageous for field applications. Nevertheless, their cost and limited selectivity pose challenges.[29,41] Meanwhile, IR sensors offer remarkable selectivity and the capability for multi-component analysis but are typically larger due to their discrete component configurations. However, in recent years, established nanofabrication technologies have not only demonstrated the potential for cost-effective, high-volume production of devices but have also indicated the feasibility of developing miniaturized VOC sensors. These technologies are also being explored to reduce the impact of these adverse factors on size and volume while keeping the selectivity of IR sensors, which is the focus of this review.

TABLE II. Comparison of commercial sensor types. Sensor information is taken from SGX SENSORTECH, EMERSON, ION SCIENCE, AMETEK MOCON, and Thermo Scientific. EC: Electrochemical, PID: Photo-ionization detection, MOS: Metal-oxide-semiconductor, IR: Infrared, MEMS: Micro-electromechanical systems.

Sensor type	EC	PID	MOS	IR[a]	MEMS
Package size (cm^3)	~6	~6	~0.05	~4	~0.04
Power consumption	+++	+	++	+	++
Selectivity	++	++	+	+++	+
Multi-component analysis	+	++	+	+++	+
LOD	ppb	ppb	ppm	ppm	ppm
On-chip integration	++	+	+++	++	+++

[a] Discrete optical components based IR sensor.

As a subset of IR-based VOC sensors, the distinguishing advantages of IR spectroscopic VOC sensors, highlighted in this review, are their remarkable selectivity and label-free detection capabilities.[42–45] These unique attributes effectively overcome selectivity limitations found in other sensors without resorting to destructive detection methods. Furthermore, IR spectroscopic sensors demonstrate compatibility with conventional IR-refractive index-based sensors and provide immunity to electromagnetic interference.[46] In recent years, advanced fabrication technologies, such as complementary metal-oxide semiconductors (CMOS), have played a critical role in the development of miniaturized IR spectroscopic sensor devices. Figure 2 illustrates the concept of miniaturization in the IR spectroscopic VOC sensor system. Compared to traditional bulk IR spectroscopic sensing systems, miniaturized IR spectroscopic VOC sensors offer several advantages, including the analysis of small samples,[47] multiplexing capabilities,[47] easy integration with other components,[46] and reduced cost and weight.

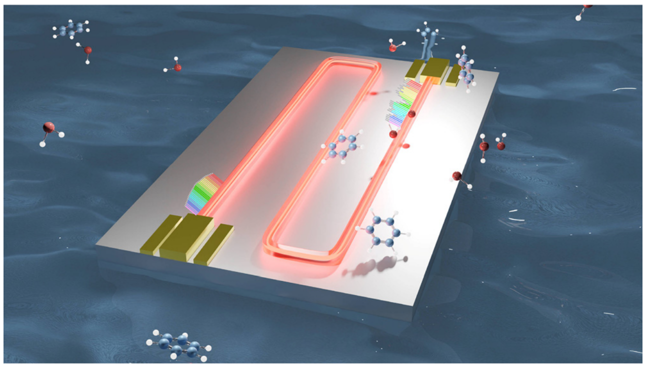

FIG. 2. Concept of miniaturization spectroscopic VOC sensor system. The IR light is emitted from an integrated laser and detected by an integrated detector. The substance to be measured around the sensor will absorb light at a specific wavelength.

These advantages underscore the potential for swift and convenient VOC analysis.

This article provides a comprehensive review of state-of-the-art IR spectroscopic-based VOC sensors, with a specific emphasis on the growing trend of miniaturization. Section II delves into the IR absorption-based detection mechanism and setup. In Sec. III, we explore the research advancements in selective, fast-response IR spectroscopic sensors with high LOD, encompassing fiber-based, integrated photonics-based, and surface enhancement-based technologies. Additionally, we will investigate the potential of monolithic integrated VOC sensor systems, address current challenges, and provide future perspectives in Sec. IV.

II. IR ABSORPTION-BASED DETECTION MECHANISM AND SETUP

This section provides an in-depth exploration of the infrared absorption-based detection mechanism and the corresponding setup employed in VOC sensors. Understanding these fundamental aspects is pivotal for comprehending the subsequent advancements discussed in the paper.

A. Why optical sensors focus on the IR spectrum?

The utilization of the infrared (IR) spectrum in optical sensors is rooted in the dual capacity of light as an information carrier, encompassing both communication and sensing functions. While the IR waveband is conventionally associated with optical communication, it is crucial to recognize that nearly every organic substance, including VOCs, exhibits specific vibrational absorption characteristics in the IR region. This inherent feature renders the IR spectrum exceptionally well-suited for sensing applications. We consider VOCs as an illustrative example. Vibrations within VOCs manifest two fundamental types: stretching and bending vibrations, as depicted in Fig. 3. When IR light interacts with those molecules, the photon energy of specific frequencies contributes to vibrational energy level transitions. In the case of VOCs, the total vibrations can be deconstructed into various harmonic vibrational modes, each corresponding to specific absorption lines. Notably, several functional groups within VOCs exhibit principal vibration absorption. Through a detailed analysis of the location, amplitude, and linewidth of these principal absorption peaks, it becomes possible to accurately and effectively determine the type of VOCs present and their respective concentrations.

Lights in the IR region with a wavelength range from 0.75 to 2 μm are commonly known as near-infrared (NIR), while the adjacent longer wavelength range from 2 to 20 μm falls into the categorized of mid-infrared (MIR).[43] While organic molecules exhibit absorption lines in both NIR and MIR,[48,49] the fundamental vibrations of most VOCs occur in the MIR, with NIR typically representing the overtones absorption region. In the overtone region, molecules absorb photons with twice or higher the energy of the original photons, facilitating transitions between two or more distinct energy levels. Due to the low probability of molecule transitions in the overtone region, VOC absorption in NIR can be orders of magnitude lower than in MIR. This feature theoretically endows MIR spectroscopy with an elevated signal-to-noise ratio, enabling the detection of lower limits. As such, MIR is often referred to as the "fingerprint region" and is a preferred region for VOC detection.[44] Common chemical bond absorptions in the MIR include the C–H stretching absorption peak of alkane at 3.33–3.52 μm, the C=C stretching vibration absorption peak in alkenes at 5.9–6.13 μm, and the C=O stretching vibration absorption peak in aldehydes at 5.7–6 μm.[50] Considering factors like mass effects, coupling effects, and ring strain that can influence the absorption peak's location, the optimal spectroscopic sensing approach involves detecting and comparing molecular fingerprint spectra with a set of combined peaks. Furthermore, when identifying mixed analytes, the component and concentration of the analyte could be recovered by combining the vibration fingerprint spectroscopy of different functional groups or molecules with machine learning algorithms. Fundamental fingerprints of many VOCs are depicted in Fig. 3. Additionally, due to the IR absorption influence from water, only the 3–5 and 8–12 μm regions, known as atmospheric transparent windows, are relatively transparent for IR detection.[43] These transparent wavebands are suitable for outdoor sensing environments, such as hyperspectral images, to obtain city-scale VOC fingerprints.[23,50]

In addition to its efficacy in vibration absorption, the choice of materials for the development of optical sensors in the IR wavelength offers distinct advantages. It is noteworthy that different dielectrics exhibit different responses across different IR subbands. Surprisingly, silicon (Si), a widely used semiconductor material, demonstrates transparency throughout the wavelength spectrum, ranging from 1 to 8.5 μm. Silicon dioxide (SiO_2), another common material, can also support IR wavelengths up to 3.6 μm.[51] These readily available materials feature transparent windows that cover either a substantial or complete portion of the VOC vibration line. To effectively address sensing wavebands within the MIR spectrum that may not be entirely covered, a strategic approach involves combining Si with other materials or opting for alternatives like germanium (Ge) and chalcogenide glass (ChG). Importantly, extensive research and practical applications related to these material platforms have steadily matured.[52–54] Furthermore, these materials exhibit noteworthy characteristics such as nonlinear effects and flexibility, opening up unexpected applications and paving the way for new opportunities and directions in development.

B. Measurement technologies of IR absorption spectroscopy

Spectroscopic sensing follows the Beer–Lambert Law, a combination of Lambert's law in 1760 and Beer's law in 1852. Lambert's law

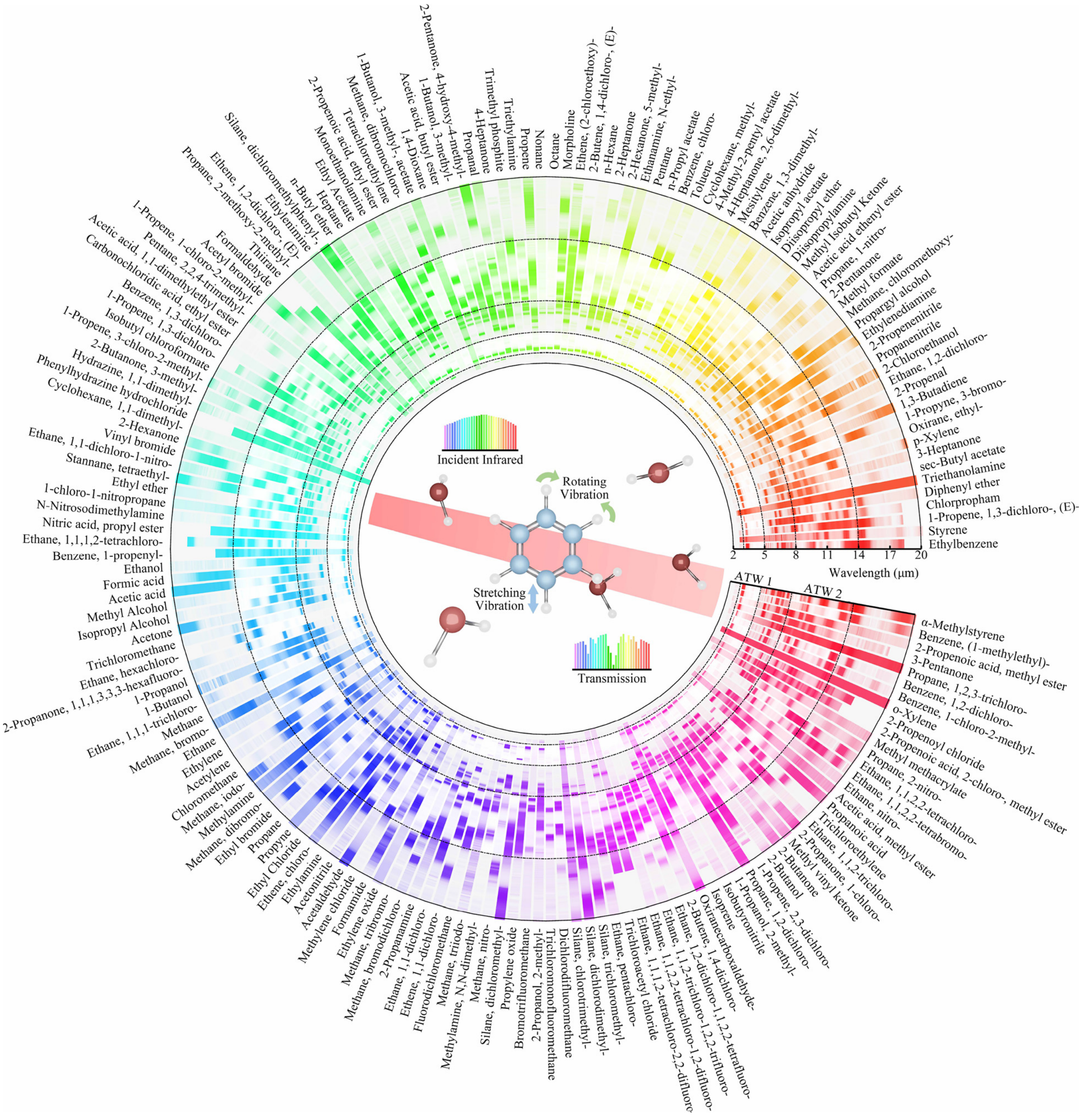

FIG. 3. Schematic spectral regime for VOC analysis. The varying depth of color signifies the intensity of absorption within the spectrum, and the bars indicate the optical atmospheric transparent windows (ATWs) of materials. The substances featured in the schematic are drawn from the VOCs list E761346 curated by the Environmental Protection Agency (EPA).[55] The corresponding IR spectra are sourced from the National Institute of Standards and Technology (NIST),[56] underscoring the relevance of the depicted spectral regions for the accurate identification and analysis of VOCs.

asserts that light attenuation is directly proportional to material thickness, while Beer's law states that light attenuation correlates with material concentration. The modern Beer–Lambert law expressed as Eq. (2) describes light transmission through an absorbing material[57–59]

$$I(\nu)_{out} = I(\nu)_{in} e^{-\alpha(\nu)} = I(\nu)_{in} e^{-\sigma(\nu)CL}, \tag{2}$$

where $I(\nu)_{out}$ and $I(\nu)_{in}$ are incident and transmitted light intensities, $\alpha(\nu)$ is the absorbance at optical frequency ν, $\sigma(\nu)$ is the absorption cross section at the corresponding frequency, C is the concentration, and L is the optical absorption path length.

Under a uniform line of sight, the absorbance $\alpha(\nu)$ is further expressed by the following equation:[60]

$$\alpha(\nu) = \sum_j S_j(T) P X \phi_j(\nu, T, P, X) L. \tag{3}$$

Here, j denotes a specific absorption transition, and $S(T)$ ($\mathrm{cm}^{-2} \times \mathrm{atm}^{-1}$) is the line strength as a function of temperature T (K), P (atm) is the pressure of the absorbing species, X is the species mole fraction, ϕ (cm) is the line shape function, and L (cm) is the absorption path length.

The line shape function ϕ is normalized to 1 [Eq. (4)].[61]

$$\int_{-\infty}^{+\infty} \phi \, d\nu = 1. \tag{4}$$

The integrated absorbance of an absorption transition A_j is given by the following equation:[62]

$$A_j = \int_{-\infty}^{+\infty} \alpha(\nu)\, d\nu = S_j(T) P X L \int_{-\infty}^{+\infty} \phi_j(\nu, T, P, X)\, d\nu = S_j(T) P X L. \tag{5}$$

With this understanding, we can delve into advanced systematic sensing applications based on IR absorption spectroscopy. Three main extended techniques in IR spectroscopy are tunable diode laser absorption spectroscopy (TDLAS), broadband absorption spectroscopy (BAS), and cavity ringdown spectroscopy (CRDS). Despite their unique achievements, the fundamental configuration of optical sensors remains consistent, comprising a light source, a sensing cell, and a detection unit.

1. Tunable diode laser absorption spectroscopy (TDLAS)

Tunable diode laser absorption spectroscopy (TDLAS) represents a classical optical sensing principle,[63] as illustrated in Fig. 4, distinguished by its unique light source configuration. The pivotal component in this setup is a tunable diode laser characterized by a narrow and singular linewidth. Complementing this, photodetectors tuned to the response spectrum corresponding to the laser's emission are integral to the system. To be more specific, TDLAS systems can be further categorized into two main types: direct absorption spectroscopy (DAS) and wavelength modulation spectroscopy (WMS). DAS offers notable advantages such as operational simplicity, wide applicability, straightforward data analysis, and the ability to determine absolute concentration.[64,65] On the other hand, WMS, while not directly providing absolute concentration values, excels in suppressing background noise. This characteristic enhances the LOD and overall robustness compared to DAS. In Secs. II B 1 a and II B 1 b, a more detailed exploration of these two systems will be presented.

a. Direct absorption spectroscopy (DAS). In the realm of DAS, the most important factor is the judicious selection of laser emission wavelength, a choice contingent upon identifying a suitably strong and isolated absorption line. Unlike keeping the wavelength constant over time, as observed in fixed-wavelength DAS, traditional DAS involves scanning the emitted light's wavelength around the absorption line during spectroscopic sensing. Fixed-wavelength DAS, due to its limited spectral information, is more susceptible to the inherent fluctuations of lasers and non-absorbing losses, rendering it less robust.[62] After the interaction between light and the analyte within the sensing cell, absorption spectroscopy is retrieved by scrutinizing the light intensity signal captured by a designated detector, such as a photodiode. The accurate determination of the absorption line shape relies on analyzing the spectral variation of light intensities. The fitting line–shape relationship between gas properties (e.g., concentration, pressure, and temperature) and absorbance is derived through the examination of integrated absorbance or absorbance at specific wavelengths. The LOD and corresponding integration time, indicative of the sensing system's stability and sensitivity, are determined through Allan deviation analysis.

Scanned DAS, achieved by faster or wider wavelength scanning around the absorption line, mitigates background fluctuations, such as variations in emitted light wavelength due to temperature instability.

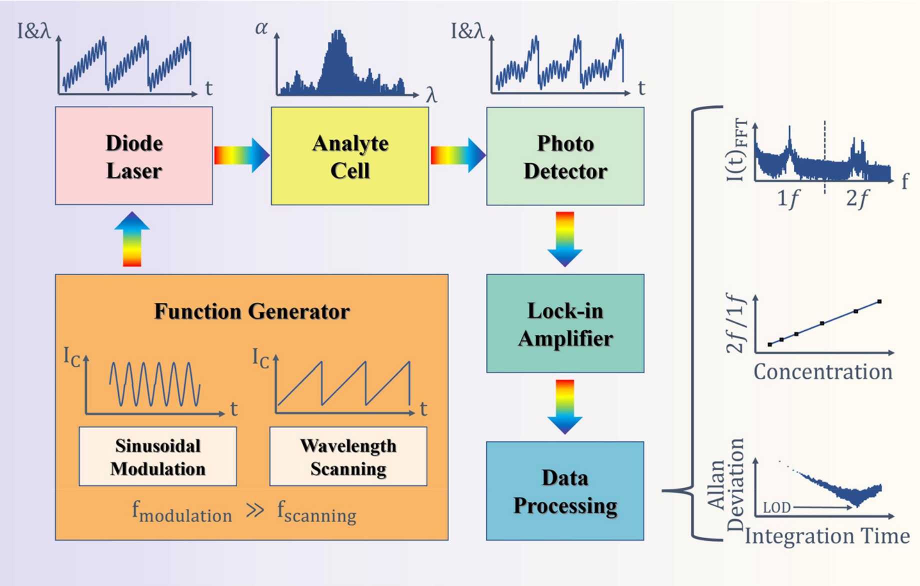

FIG. 4. Schematic of tunable diode laser absorption spectroscopy. Wavelength modulation spectroscopy in tunable diode laser absorption spectroscopy uses sinusoidal modulation at a significantly higher frequency than wavelength scanning around the selected absorption line. The extracted higher-order harmonics help reduce noise and enhance sensing robustness. It is also worth noting that, in comparison, direct absorption spectroscopy does not use sinusoidal modulation and directly determines analyte concentration by analyzing variations in light intensity. I: light intensity. I_C: Injection current. f: frequency. t: time. λ: wavelength. α: absorbance.

Nevertheless, it fundamentally relies on subtle variations in measured power, which is susceptible to non-absorbing losses like unintended beam deflection from vibration and transmission losses due to instrument aging. In scenarios of low SNR measurements, DAS faces challenges in distinguishing absorbed signals from background noise, potentially leading to longer integration time and introducing additional sources of instability.

b. Wavelength modulation spectroscopy (WMS). WMS constitutes another facet of TDLAS renowned for its efficacy in eliminating background noise, building upon the principles of DAS. In the WMS paradigm, the diode laser not only scans the wavelength around the selected absorption line but also undergoes simultaneous sinusoidal modulation at a significantly higher frequency f. Moreover, both the laser wavelength and output light intensity are modulated by the injection current that tunes the lasers.[66–68] After transversing the sensing cell, the light, now partially absorbed, is detected by a sensor. Subsequently, the signal undergoes processing through a lock-in amplifier to isolate the desired nth harmonic at the detection frequency nf, where n is an integer (e.g., 1, 2,…).[58] This enables the extraction of absorption information carried by the harmonics, effectively isolating it from noises outside the lock-in amplifier's filter bandwidth.

The harmonic technique improves resistance to non-absorbing losses by elevating the frequency above common noise sources operating at lower frequencies. In sensing applications, the first and second harmonic signals ($1f$ and $2f$) are frequently utilized to determine gas properties, particularly in low SNR situations.[69] The $2f$ harmonic is preferred due to its relatively stronger signal and lower non-absorbing background noise at higher frequencies, such as residual amplitude modulation (RAM).[62,69] The normalized $2f/1f$ ratio is a commonly employed technique to strengthen WMS immunity to non-absorbing variations in light intensities resulting from non-ideal laser and detector effects, which tend to vary more slowly than the modulation frequency f.[70] This technique contributes to improving the LOD and overall sensor robustness. Higher-order harmonics (beyond $2f$) are generally not adopted due to their lower signal strength. Nevertheless, some studies suggest that higher-order harmonics (e.g., $3f$, $4f$, …), giving a lower normalized ratio, may aid in mitigating the nonlinear response between light intensity and injection current, providing more accurate results.[71]

Compared with DAS, WMS does not directly yield absolute analyte concentrations.[72] The $2f$ signal in WMS is proportional to species concentration. Establishing the relationship between absolute concentration and signals traditionally involves sensor calibration with analyte line parameters, temperature, and pressure to obtain standard gas concentration. Recent advancements in WMS, however, introduce calibration-free techniques through developed models or spectral-fitting techniques.[73]

2. Broadband absorption spectroscopy (BAS)

When the incident light's linewidth is not sufficiently narrow, sensing methods commonly fall under the umbrella of broadband absorption spectroscopy (BAS). The schematic in Fig. 5 depicts the fundamental elements of BAS. Various wideband IR sources, including light-emitting diodes (LED), amplified spontaneous emission (ASE), thermal/IR emitters, and supercontinuum sources, find applications in developing measurement methods based on BAS. Notable examples include non-dispersive infrared (NDIR) spectroscopy and Fourier transform infrared (FTIR) spectroscopy.

a. Non-dispersive infrared (NDIR) spectroscopy. NDIR spectroscopy stands out as a cost-effective and efficient approach for analyte detection. This method involves the utilization of thermal emitters or IR LED paired with photodiodes (PD). Adhering to the Beer–Lambert law, the concentration of VOC is deduced by comparing the measured power difference under the exposure to VOC and non-VOC conditions. The setup, with or without an optical filter, can measure concentration, but the inclusion of filters designed for VOCs' characteristic spectral lines enhances component identification. Alternatively, configurations employing multiple LEDs and PDs contribute to increased measurement stability.

NDIR spectroscopy offers an economical solution for VOC sensing, particularly well-suited for single gas detection. However, its performance tends to be comparatively lower in multi-component identification when juxtaposed with other laser-based methods.

b. Fourier transform infrared (FTIR) spectroscopy. In contrast to NDIR, FTIR extends its focus beyond concentration detection to encompass mixture component analysis. When utilizing a broadband light (e.g., thermal emitter) as the carrier of VOC sensing information, instruments such as a spectrometer are employed to reconstruct absorbance. While tunable lasers in TDLAS typically have a narrow linewidth but a relatively limited measurement bandwidth, resulting in higher analysis precision but fewer detectable molecule types in the MIR, the spectrometer in FTIR offers a broader sensing range albeit with lower resolution.

Notably, the production of a high-quality tunable laser is a complex task, making the accessibility of a spectrometer considerably more straightforward. Consequently, in FTIR, the responsibility of

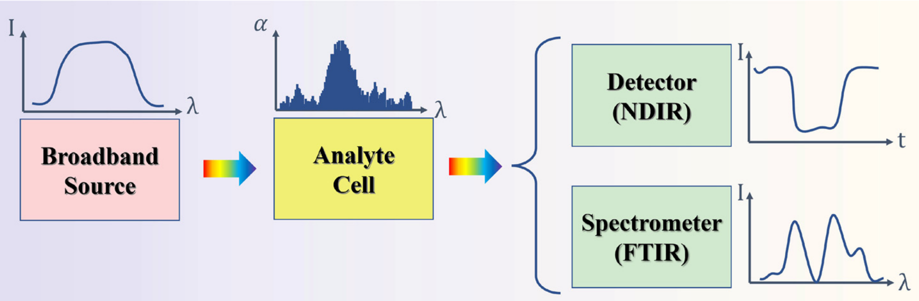

FIG. 5. Schematic of broadband absorption spectroscopy. NDIR uses a detector with or without an optical filter to detect broadband light intensity. FTIR uses a Fourier transform spectrometer to recover the broadband absorption spectrum. I: light intensity. t: time. λ: wavelength. α: absorbance.

measuring absorption wavelengths shifts from the tunable laser to the spectrometer. The spatial heterodyne Fourier transform spectrometer (SHFTS) is widely used in absorption spectrum reconstruction, operating on the principles of the Fourier transform. Designs such as the Michelson interferometer and Mach–Zehnder interferometer, both featuring dual optical pathways, are commonly employed in SHFTS. These pathways are split by a splitter and then recombined into a single channel. For monochromatic light, one optical path maintains a fixed length (reference path) with an optical phase φ, while the other varies linearly, changing the wave phase from φ to $\varphi + \Delta\varphi$. The resulting interference yields light intensity (I) with periodic variation within the 0–1 range, intrinsically linked to the corresponding phase difference ($\Delta\varphi$).

In the case of broadband sources, different IR wavelengths exhibit distinct output intensities due to their specific optical phase differences. Fourier transform spectrometry involves establishing the relationship between wavelength intensity and interferogram at different phase differences, enabling the measurement of absorption peaks in FTIR. In FTIR, the absorption peaks are measured via the Fourier transform spectrometer (FTS). In scenarios involving samples with multiple unknown VOC components featuring identical or closely situated absorption peaks, differentiation can be challenging with a low-resolution FTIR. Typically, a resolution between 2 and 4 cm^{-1} is generally adequate for the analysis of liquid-phase organic compounds, given their spectral bands naturally spanning several wavenumbers. However, achieving a resolution of $\leq 1\,\text{cm}^{-1}$ in gas-phase detection significantly enhances accuracy, particularly in scenarios requiring multi-component analysis.[74]

3. Cavity ringdown spectroscopy (CRDS)

Compared to TDLAS, the main difference in the sensor configuration of cavity ringdown spectroscopy (CRDS) lies in the requirement for its sensing cell to function as a cavity resonator, as shown in Fig. 6. CRDS-based sensors accommodate either pulsed or continuous wave (CW) laser. The operational sequence involves injecting light into a cavity resonator. Upon reaching resonance conditions and establishing stable resonance, the transmitted light experiences a significant increase. Subsequently, the incident light is extinguished, and the decay time of optical power exiting the cavity, both with and without the analyte, is measured to deduce species properties. The exponential decrease in light intensity is primarily determined by the reflectivity of cavity reflectors (R_m) and absorbance (α) and is quantified using a modified Beer–Lambert law for CRDS[62]

$$I(t)_{out} = I_{in} e^{-t/\tau} = I_{in} e^{-\frac{[(1-R_m)+\alpha(\nu)]ct}{L}}. \tag{6}$$

Here, τ represents the decay time with an analyte, c is the speed of light, and L remains the optical absorption path length, akin to the effective path length of the cavity with a physical distance d, where $L = \frac{d}{1-R_m}$, disregarding scattering losses. The absorbance is derived as

$$\alpha = \frac{L}{c}\left(\frac{1}{\tau} - \frac{1}{\tau_0}\right). \tag{7}$$

Here, τ_0 signifies the decay time without an analyte.

One of the most significant features of CRDS is its excellent LOD attributed to the extended actual path length, spanning meters or even kilometers, and the augmented light power facilitated by resonators. Furthermore, as analyte properties are assessed based on time differences rather than variations in measured power directly obtained from detectors, CRDS mitigates non-absorbing losses, particularly the amplitude fluctuations of lasers.

III. ADVANCES IN MINIATURIZATION OF IR ABSORPTION-BASED VOC SENSORS

In Sec. II, we provide a concise overview of common IR measurements, emphasizing the pivotal role of the sensor in various configurations. Optical fibers, photonic chips, and metamaterial antennas have emerged as promising components for miniaturized IR VOC absorption sensors. Notably, the NIR waveband, extensively used in communication applications, has witnessed significant advancements in miniaturized NIR devices, such as optical modulators, with Si and SiO_2 serving as standard and well-established material platforms for production.[75] The mature design and fabrication processes, particularly in the realm of optical fiber-based NIR sensors, have facilitated successful research, development, and commercialization.[32]

The evolution of compact and integrated communication devices has catalyzed the exploration of MIR sensing simultaneously. New platforms and fabrication technologies are being explored for miniaturized MIR sensors. However, the reduction in size of these devices inevitably leads to a diminished interaction region, influencing sensitivity and LOD. To mitigate these effects, specific measures are necessary. This section reviews advanced designs and techniques employed in these miniaturized sensors, aiming to attenuate or eliminate the challenges associated with size reduction and its impact on sensitivity and LOD.

A. Optical fiber-based absorption sensors

A conventional fiber-based sensor consists of a light source (typically a laser source), a sensing cell, measurement devices, and optical input/output components (I/O). Based on their function, fiber-based sensors can be classified into two categories: extrinsic sensors and intrinsic sensors.[76,77]

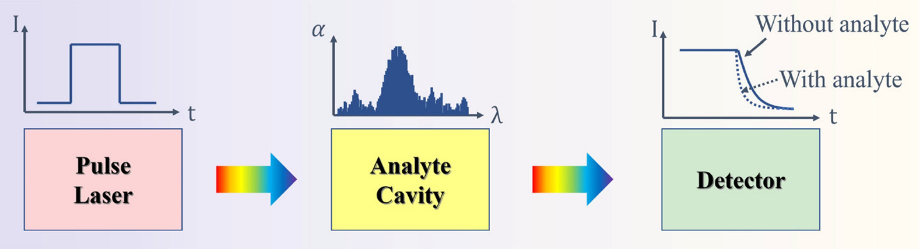

FIG. 6. Schematic of cavity ringdown spectroscopy. Once the cavity achieves stable resonance, the incident light is extinguished, and the decay time is measured under both conditions: with and without the analyte. The species properties are deduced by comparing these decay times. I: light intensity. t: time. λ: wavelength. α: absorbance.

In extrinsic fiber-based sensors, fibers primarily serve as interconnectors between components.[76] In this configuration, light is directed to an external sensing cell where it interacts with external transduction elements. The output signal is then coupled back into fibers for analysis. Extrinsic sensors are generally cost-effective and simpler in structures, although precision alignment of input and output fibers can pose challenges. These sensors find widespread use in measuring speed, rotation, displacement, and acceleration.[77,78] When applied to VOC sensing, guided light passes through the target analyte directly or interacts with absorption transduction elements in the gas cell. Despite being labeled as "fiber-based" sensors, their use of optical fibers often leverages advantages such as low attenuation, enabling remote sensing, and the potential for multiplexing in creating multipoint sensor networks.[79] In some cases, optical fibers are merely tools for light delivery in scenarios where miniaturization is not a requirement.

In intrinsic fiber-based sensors, fibers not only transmit signals but also act as sensing cells.[76] In these sensors, the guided light is modulated within a specially designed sensing region of the fiber. For VOC sensing, researchers alter the characteristics of light by studying and exploiting the physical properties of fibers. These developed fiber structures aim to achieve better LOD and selectivity. While manufacturing challenges may arise, intrinsic sensors eliminate the need for precise fiber alignment by avoiding external gas cells, facilitating sensor miniaturization.

A fundamental theory in fiber sensors is fiber evanescent wave spectroscopy (FEWS), where light propagation is based on attenuated total reflection (ATR) principles.[80] Analyte sensing is accomplished by utilizing the evanescent field generated by ATR, occurring at the interface between the fiber core and the surrounding layer, typically penetrating a few micrometers into the adjacent sensing layer.

The Beer–Lambert law, employed in intrinsic fiber-based sensors using unclad fibers with a special sensing medium (Fig. 7), describes the attenuation of the evanescent field[81]

$$I_{out} = I_{in} e^{-\xi(n_a)L_a}. \tag{8}$$

Here, $\xi(n)$ is the decay coefficient of the evanescent field as a function of the refractive index of the surrounding sensing medium n_a that absorbs analytes, and L_a is the length of the sensing film.

The attenuation results from the interaction between the evanescent field and surrounding analytes, and the decay coefficient is represented as[81]

$$\xi(n_a) = \frac{n_a \tau \lambda \cos^2\theta_i}{2r\pi(n_r^2 - n_a^2)\sin\theta_i}, \tag{9}$$

where τ is the bulk decay coefficient of the analyte, r is the radius of the fiber core, n_r is the corresponding refractive index of the unclad fiber, and θ_i is the incidence angle at the core-medium interface.

1. Single-mode solid fiber (SMF)

For MIR optical fiber sensors based on FEWS, selected fibers generally fall into two categories: solid fibers, further classified as glass-like fibers, polycrystalline fibers, and hollow fibers. Among solid fibers, the prevalent glass-like material in the MIR region is ChG, with a maximum transmission region exceeding 20 μm.[82–84] Another noteworthy example is polycrystalline fiber, exemplified by silver halide (AgX), providing a broad transmission range of 3–18 μm,[85] covering a significant portion of the MIR spectrum.

Sensors employing these solid fibers are typically categorized based on fiber geometry standards.[86] In 1988, the first chemical optical sensor using ChG fiber was introduced for butanone characterization.[87] These fibers, maintaining a straight geometry, form the basic type used in FEWS sensors. In this context, various polymers are chosen and coated on the fiber core to enhance selectivity and enrich the analyte within the sensing region. For instance, Krska *et al.* combined FTIR with ATR optical fiber to design a sensor based on low-density polyethylene-coated AgX fiber, enabling the first *in situ* ppm level detection of chlorinated hydrocarbons (CHCs) in water.[36] Su *et al.* introduced a sensor using a novel Ge-As-Se-Te ChG fiber coated with polydopamine for *in situ* sensitive detection of p-xylene in water [Fig. 8(a)].[37] The polydopamine coating significantly amplified absorbance at the absorption line by 18 times and improved the detection limit by 40 times. Howley *et al.* designed a sensor based on polydimethylsiloxane (PDMS)-coated sapphire fibers for hydrocarbon detection, proving its capability to detect ppm levels.[33] Other polymers, such as PMMA, PAB, PSB, and polyethylene, have been explored for various targeted analytes,[88–96] significantly enhancing sensing performance.

To further enhance sensing performance, alternative fiber geometries have been developed. Bending the fiber, formed through geometrical deformation, has demonstrated improved performance by enhancing the penetration depth of the evanescent field.[97] Houizot *et al.* demonstrated a sensor based on ChG fiber for ethanol sensing [Fig. 8(b)].[98] In this study, the fiber was meticulously shaped into a compact loop with a 2 mm diameter. The results were compelling; when compared to a single U-turn geometry, the fabricated three full loops of fiber exhibited superior global sensitivity. A mechanical robustness test further underscored the durability of this design,

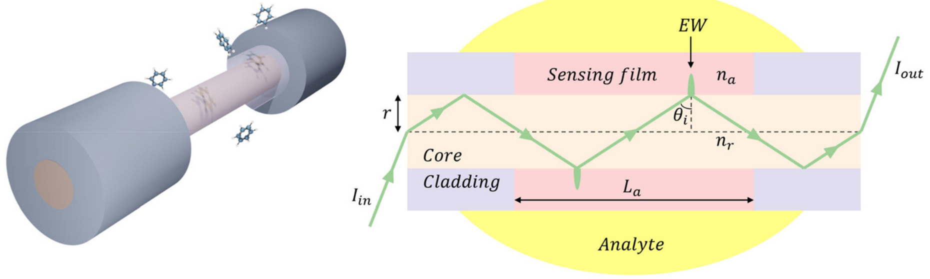

FIG. 7. Schematic of fiber sensor and evanescent wave spectroscopy. In the sensing region, the sensing film surrounds the fiber core rather than the cladding. The analyte interacts with the evanescent wave in the sensing film.

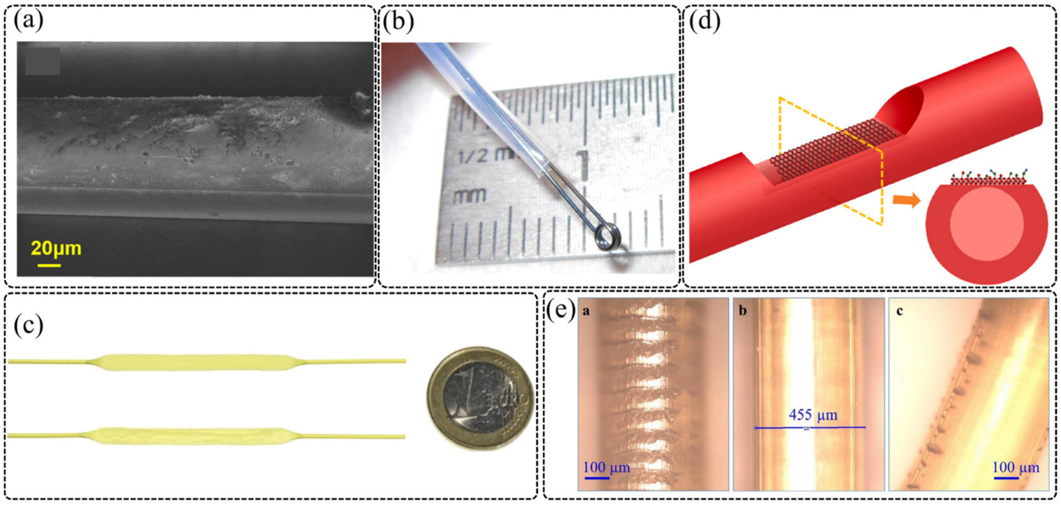

FIG. 8. Fiber sensors based on fiber evanescent wave spectroscopy. (a) Scanning electron microscope (SEM) image of a ChG fiber coated with polydopamine.[37] Reprinted with permission from Su *et al.*, Opt. Express **28**(1), 184 (2020). Copyright 2020 The Optical Society.[37] (b) Schematic of the ChG fiber loop.[98] Reprinted with permission from Houizot *et al.*, Sensors **14**(10), 17905–17914 (2014). Copyright 2014 Authors, licensed under a Creative Commons Attribution (CC BY) license.[98] (c) Image of modified AgX fibers with a planar sensing region with (top) and without (bottom) coated polymer.[88] Reprinted with permission from Lu *et al.*, Nat. Protoc. **11**(2), 377–386 (2016). Copyright 2016 Springer Nature.[88] (d) Schematic of side-polished ChG fiber coated with graphene oxide.[103] Reprinted with permission from Yang *et al.*, Ceram. Int. **49**(1), 1291–1297 (2023). Copyright 2023 Elsevier.[103] (e) Images of AgX fibers with different lateral surfaces.[104] Reprinted with permission from Korsakova *et al.*, Infrared Phys. Technol. **128**, 104529 (2023). Copyright 2023 Elsevier.[104]

revealing that a complete loop of fiber could withstand forces 130 times greater than those tolerated by the classical ChG fiber.

Another method involves reducing the diameter of one section of the fiber to less than that of the core of the original uniform fiber. Fibers with this specific geometry are referred to as tapered sensors, as the heated uniform fiber is pulled to create a thin taper waist. Mizaikoff and his group designed a series of sensors, [Fig. 8(c)], using modified AgX fibers for more sensitive detection of VOC in water. This includes CHCs like monochlorobenzene (MCB), dichlorobenzene (DCB), trichloroethylene (TCE), chloroform (CF), and monocyclic aromatic hydrocarbons such as benzene, toluene, o-, p-, and m-xylene.[80,88,99,100] The diameter of a specific fiber section was intentionally decreased to amplify the evanescent field, and a polymer membrane was applied to enhance selectivity in water. The coated polymer not only facilitated analyte enrichment but also provided improved mechanical robustness for their specially structured fiber. In addition to these two strategies, another approach involved introducing a planar sensing region into the fiber to increase the number of internal reflections. This technique, reported in another work[101] by the same group, revealed the observation of surface-enhanced infrared absorption (SEIRA) on nonmetallic substrates for the first time. All these three strategies were employed to improve the sensor's performance, ultimately achieving a significant improvement in the detection limit to the parts per billion level.

Utilizing side polishing of fibers is another effective method to enhance the limit of detection (LOD). These side-polished fibers (SPF) with a D-shape geometry facilitate easier leakage of evanescent waves, increasing the contact area between the wave and the analyte, thereby enhancing the interaction with the analyte. For example, Goya *et al.* developed a sensor using fluoride SPF, employing fluoride fibers for MIR online sensing systems.[102] Compared to other MIR optical fibers, fluoride fibers can be produced on a commercial scale. Yang *et al.* designed a sensor using a ChG SPF for highly sensitive butane sensing, as depicted in Fig. 8(d).[103] The sensing area was coated with graphene oxide, a novel 2D material with abundant oxygen-containing functional groups that enhance the absorption of specific organic compounds. Its structure offers a large contact area with gas molecules. Concerns about the response time and repeatability were also addressed. Additionally, Korsakova *et al.* demonstrated a sensor based on AgX fibers with lateral notches for ethanol detection, illustrated in Fig. 8(e).[104] In this study, the LOD was improved by leveraging the optimized bending radius and the notched lateral fiber surface.

For fiber-based sensors utilizing DAS or WMS, the focus is on enhancing the interaction between light and analyte per unit absorption path length. Typical resonant structures of fibers, such as fiber Bragg gratings (FBGs) and long-period gratings (LPGs), are commonly applied in sensors based on interferometry strategies that depend on changes in refractive index. In absorption spectroscopy, these structures are often adopted in sensors based on CRDS.

As mentioned before, compared to TDLAS, CRDS can reduce non-absorbing interferences since it does not rely on the direct changes of detected intensity.[105] At present, many works on all-fiber CRDS, also known as fiber loop ringdown spectroscopy (FLRDS), are focused on the NIR region. In this context, we will delve into several notable works with the aim of inspiring related endeavors in the MIR. For example, Pu *et al.* proposed a method to enhance the interaction between light and analyte while averting the compromise of mechanical robustness resulting from fiber geometry modifications.[106] By incorporating a pair of LPG into the fiber link, over 99% of the light was coupled out from the fiber core to the cladding, facilitating interaction with the analyte. This engineered LPG cavity ensured a low insertion loss for the sensing unit, a design validated in an FLRDS sensing system. In this system, the conventional highly reflecting mirrors found in free-space CRDS setups were replaced with two 1 × 2 couplers with a 1%/99% ratio, commonly used in FLRDS sensors. Experimental results demonstrated that this sensor could detect 1-octyne at a minimal concentration of 0.62%. Another advancement was showcased by Hu *et al.* in the form of an all-fiber wavelength-scanned cavity ringdown sensor.[107] This system featured an automatic wavelength scanning process that enabled the acquisition of both the empty cavity loss and the absorption spectrum within the same scanning operation. The operation wavelength was determined by stretching the FBG using a piezoelectric transducer.

2. Microstructured hollow fiber

Hollow fiber, also known as microstructured optical fiber, is characterized by a core (solid or hollow) with distributed holes along its length, allowing the formation of a low-volume analyte cell for sensing applications. Two main types of hollow fibers are prevalent in MIR sensing: photonic crystal fiber (PCF) and inhibited coupling fiber (ICF), distinguished by their respective guiding principles.

In PCFs, air holes are arranged periodically in the cladding, as exemplified by those with solid cores [Fig. 9(a)].[108] The higher refractive index of the core section, compared to the surrounding air holes, enables light confinement within the core through total internal reflection (TIR).[109–114] This index guided TIR-PCF has been demonstrated in MIR sensing applications with low confinement loss, showcasing the potential for fiber sensors.[115] Nevertheless, the majority of PCFs feature hollow-cores [Fig. 9(b)], guiding light through the photonic bandgap (PBG) effect.[116–118] The PBG fiber, utilizing traditional materials, offers a large overlap between the analyte and sensing light due to its ability to guide light in the air core. This approach provides lower transmission loss in the MIR region. Gayraud *et al.* designed a methane sensor using PBG-PCF, where the adopted silica-based PBG fiber exhibited a low transmission loss of approximately 2.6 dB/m around a 3 μm wavelength.[119] Compared with traditional optical fibers, PCF allows more flexible adjustment of optical properties, such as core size, numerical aperture, nonlinearity, and dispersion. However, it is noteworthy that currently widely used hollow-core PBG-PCFs support multiple guided modes, leading to intermodal interferences that can curtail sensor performance.[120] For instance, in the NIR region, several studies have explored the impact of modal interference in a widely used commercial PBG-PCF HC-1550-02 on VOC sensing.[121–123]

ICFs, another crucial type of hollow fiber, rely on inhibited coupling between core and cladding modes. The Kagome hollow-core fiber, the first reported ICF,[124] offers enhanced modal stability.[125] Applications of ICF in methane sensing have been demonstrated, particularly using Kagome hollow-core fiber for absorption spectroscopy, as shown in Fig. 9(c).[126] Here, WMS was employed to mitigate the influence of interference fringes, achieving a LOD at the ppmv level. An alternative structure within the ICF realm is the anti-resonant hollow-core fiber (ARHCF), which can be viewed as a simplified ICF structure.[127] This configuration comprises a cladding formed by several circular capillaries,[128–130] allowing for single-mode propagation with a relatively larger hollow-core diameter than PCF [Fig. 9(d)]. ARHCF has been reported to exhibit good modal stability.[120] For instance, Gomolka *et al.* designed a highly sensitive methane sensor based on ARHCF paired with an MIR interband cascade laser.[131] The implemented WMS system demonstrated experimentally verified parts per billion -level detection limits and continuous week-long monitoring of ambient methane proved feasible. Several recent works in this domain are summarized in Table III.

B. Integrated photonic devices-based IR absorption sensors

In addition to the fiber structure, extensive efforts have been directed toward miniaturizing optical VOC sensors by utilizing the photonic integrated circuit (PIC) platform. Contrasted with fibers, PIC occupies a smaller footprint and offers greater flexibility in implementing intricate structures. Among these structures, the optical waveguide, serving as a fundamental unit in PIC, is crucial for controlling the optical flow. Optical modes in the photonic waveguide are categorized into transverse electric (TE) mode and transverse magnetic (TM) mode based on the direction of the electrical field [Fig. 10(a)]. Similar to optical fibers, these modes are not entirely confined to the waveguide core. The confinement factor or sensing overlap Γ is chosen to measure the evanescent field of the propagation mode in the analyte, assessing light–matter interaction.[135,136] This is expressed as the following equation:

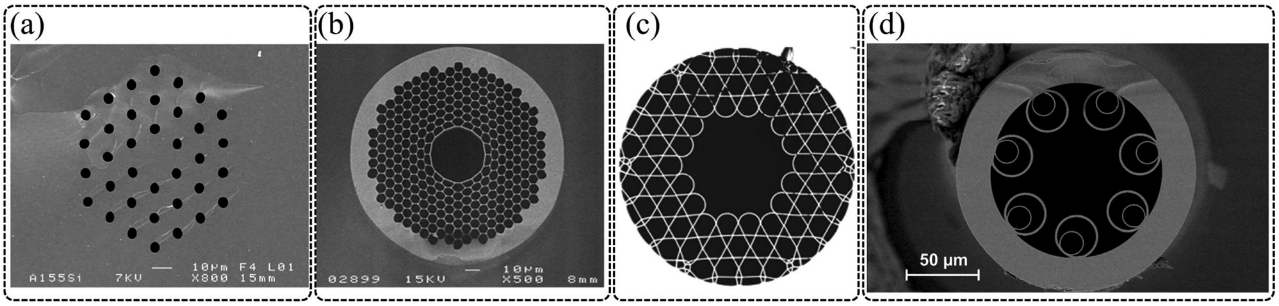

FIG. 9. Fiber sensors based on microstructured optical fiber. (a) SEM image of a solid core PCF for sensing purposes.[114] Reprinted with permission from Konorov *et al.*, Opt. Express **13**(9), 3454 (2005). Copyright 2005 The Optical Society.[114] (b) SEM image of a hollow-core PCF tailored for sensing application.[118] Reprinted with permission from Dhawan *et al.*, Optik **124**(18), 3671–3673 (2013). Copyright 2012 Elsevier.[118] (c) SEM image of a Kagome ICF for sensing purposes.[126] Reprinted with permission from Nikodem *et al.*, Opt. Express **26**(17), 21843 (2018).[126] (d) SEM image featuring an ARHCF for sensing, considered as a simplified ICF.[130] Reprinted with permission from Gomółka *et al.*, Opt. Laser Technol. **170**, 110323 (2024). Copyright 2024 Elsevier.[130]

TABLE III. Performance of fiber-based IR absorption VOC sensors. L: liquid, G: gas, RT: response time, and AT: average time.

Work	Structure	Method	Waveband (μm)	Phase	LOD (analyte)	RT/AT
132	Straight AgX fiber with a polymer coating (Epoxidized polybutadiene, EPB)	DAS	3.4–3.47	L	46 ppb (Crude oil)	A few seconds (RT)
37	Tapered ChG fiber with a polymer coating (Polydopamine)	DAS	6.596	L	50 μg/ml (P-xylene)	575 s (AT)
99	Straight AgX fiber having a planar sensing region with a polymer coating (Ethylene/propylene copolymer, E/P-co)	DAS	2.5–12.66	L	1.385 ppm (1,3-dichlorobenzene) 0.669 ppm (p-cymene)	N/A
102	Side-polished fluoride fiber	DAS	2.515–3.735	L, G	0.52% (methane)	N/A
103	Side-polished ChG fiber with graphene oxide coating	DAS	3.37	G	0.5 vol.% (butane)	195 s (RT)
106	Looped fiber with LPG	CRDS	1.5332–1.5354	L	0.62% (1-octyne)	N/A
131	Silica-based ARHCF	DAS	3.27	G	1.54 ppbv (methane)	20 s (AT)
133	Silica-based ARHCF	WMS	3.334	G	24 ppbv (methane)	40 s (AT)
134	ChG based ARCHF	WMS	10.5	G	10 ppb (ethylene)	80 s (AT)
126	Kagome ICF	WMS	3.33	G	0.505 ppmv (methane)	N/A
119	Silica-based hollow-core PCF	DAS	3.2	G	50 ppm (methane)	N/A

$$\Gamma = \frac{n_g \iint_A \varepsilon |E|^2 dxdy}{n_A \iint_\infty \varepsilon |E|^2 dxdy}. \tag{10}$$

Here, E represents the amplitude of the electrical field, ε denotes the permittivity of the material, A refers to the mode area requiring evaluation, and n_g and n_A represent the optical mode group index and refractive index, respectively. In a waveguide sensor, A stands for the analyte cladding region interacting with the evanescent field. The Beer–Lambert law can be reformulated as the following equation:

$$I_{out} = I_{in} e^{-(\Gamma C + \alpha) L_a}, \tag{11}$$

where C is the gas concentration, α is the waveguide loss, and L_a is the absorption length. Therefore, Eq. (11) indicates that certain degrees of freedom, as illustrated in Fig. 10, can be adjusted to achieve higher sensing performance.

1. Evanescent field enhancement

a. Conventional photonic waveguide structures. To enhance VOC sensing performance, the initial focus is on improving the confinement factor Γ. In PIC fabrication, the thickness of the standard wafer is typically 220 nm, leading to a lower height than the width in a conventional rectangle waveguide [Fig. 10(a)]. This shape strongly confines the lateral electrical field, making the TE polarization mode used in PIC due to its lower propagation loss. However, the TM polarization

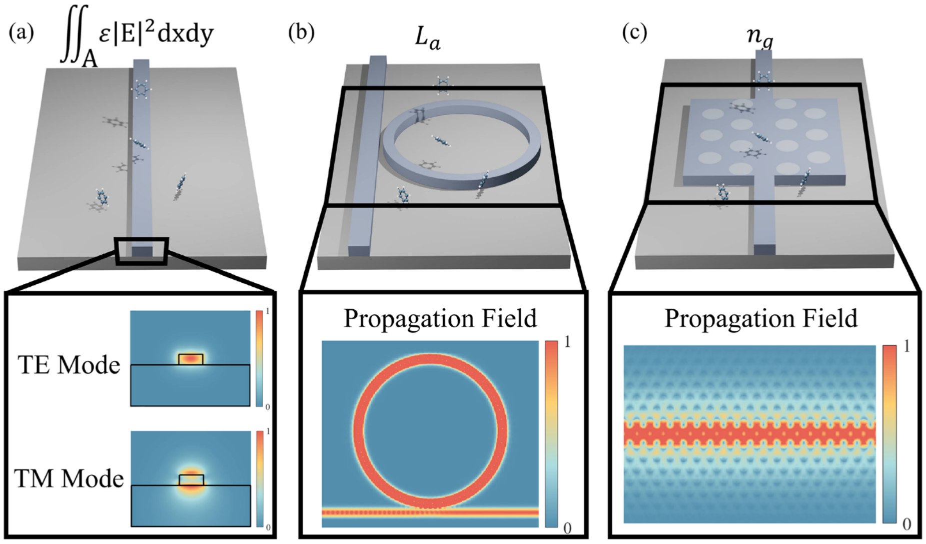

FIG. 10. The substance absorbs the evanescent wave outside the photonic structures. Three optimization strategies are used in integrated photonic sensors for enhanced analyte detection, including increasing (a) mode field confinement, (b) effective optical path, and (c) group index.

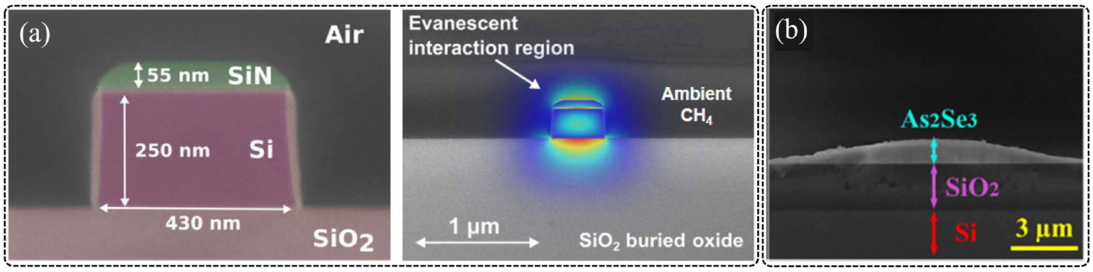

FIG. 11. Straight waveguide sensors on different material platforms. (a) Left: false-color cross section of the Si waveguide methane sensor. Right: mode profile optimized for larger Γ.[137] Reprinted with permission from Tombez *et al.*, Optica **4**(11), 1322 (2017). Copyright 2017 The Optical Society.[137] (b) ChG waveguide on SiO_2.[140] Reprinted with permission from Jin *et al.*, Anal. Chem. **91**(1), 817–822 (2019). Copyright 2019 American Chemical Society.[140]

mode leaves a larger evanescent field E in the air or analyte, resulting in a higher Γ compared to the TE mode. TM mode is thus widely applied in most straight waveguide sensors. The left panel of Fig. 11(a) illustrates commonly used high refractive index material waveguides, such as Si ($n \sim 3.43$), fabricated through etching processes, specifically designed for IR VOC sensing. A 250-nm-thick Si waveguide with a 55 nm SiN layer on top is designed near the cutoff of TM mode to achieve higher Γ, as shown in the right panel of Fig. 11(a).[137] The sensor's optimal performance was observed in the NIR $2\nu_3$ overtone band of CH_4 through TDLAS, reaching an LOD of 20 ppmv over an integration time of 1000 s. Additionally, research involving materials like Ge ($n \sim 4.02$)[138] and HgCdTe (MCT, $n \sim 3.5$)[139] shows waveguide designs for methane and acetone sensing in the MIR, respectively.

It is noteworthy that employing a lower refractive index material for TM mode waveguides contributes to a larger evanescent field and higher sensitivity. Jin *et al.* demonstrated a MIR chip sensor utilizing As_2Se_3 thin-film waveguides, as depicted in Fig. 11(b).[140] With a refractive index of 2.79, lower than that of Si or Ge, As_2Se_3 facilitates a larger evanescent field and a higher confinement factor, enhancing absorption efficiency. The substantial index contrast between As_2Se_3 and SiO_2, coupled with a thin-film semielliptical ridge structure, ensures MIR wave propagation. Utilizing deposition instead of etching in the fabrication process results in smoother waveguide edges and surfaces, reducing TM wave propagation loss to 0.16 dB/cm. This diminished propagation loss directs the attenuation of light intensity primarily toward molecule absorption rather than scattering losses, extending absorption paths for VOCs and correlating with lower LOD and heightened sensitivity.

In TDLAS measurements, an IR camera replaces the IR detector. Acetone and ethanol vapor absorption intensities were measured at different wavelengths from 3.4 to 3.5 μm by recording mode images and intensities, with a 5-s response time for VOC detection. Mixtures of ethanol vapor and N_2, ranging from 0% to 100% concentration in 20% steps, were also measured. Alternative technologies addressing propagation losses, such as the deposition of ChG and magnesium fluoride (MgF_2) on Si wafers, provide a viable solution to mitigate constraints posed by SiO2 absorption issues at longer MIR wavelengths. Specifically, the WMS detection method is employed for this ChG-on-MgF_2 methane sensor.[66] In addition to ChG, materials like silicon nitride (SiN, $n \sim 1.94$),[141] aluminum nitride (AlN, $n \sim 1.97$),[142] and niobium pentoxide (Nb_2O_5, $n \sim 2$)[143] also provide a lower core index, making them promising candidates for waveguide VOC sensors.

b. Hollow-waveguide structures. In addition to the methods discussed previously, an alternative approach to enhance sensitivity and lower the LOD involves direct absorption of IR light by VOCs, akin to spatial optics, as opposed to relying on evanescent field sensing. Hollow-core waveguides, similar to hollow fibers, could be employed for sensor miniaturization while ensuring promising light propagation. For example, Bürger *et al.* designed a type of 3D-nanoprinted anti-resonant hollow-core micro gap waveguides and detected the absorption spectroscopy of ammonia using the TDLAS method [Fig. 12(a)].[144]

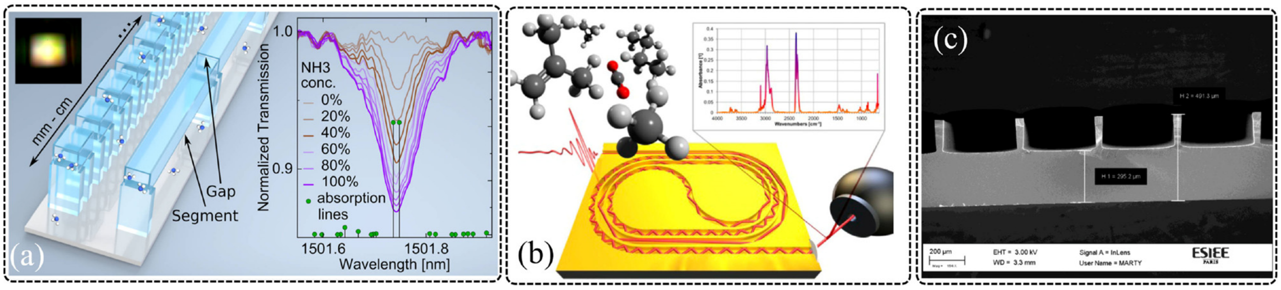

FIG. 12. Hollow-core waveguide structures enabling direct interaction between light with the analyte. (a) Anti-resonant hollow-core micro gap waveguide absorption sensor.[144] Reprinted with permission from Bürger *et al.*, ACS Photonics **9**(9), 3012–3024 (2022). Copyright 2022 American Chemical Society.[144] (b) Layered structure iHWG with yin-yang waveguide shapes.[145] Reprinted with permission from Wilk *et al.*, Anal. Chem. **85**(23), 11205–11210 (2013). Copyright 2013 American Chemical Society.[145] (c) SEM image of Fabricated Si-iHWG (after dicing).[147] Reprinted with permission from Fathy *et al.*, Proc. SPIE **11355**, 113550T (2020). Copyright 2020 SPIE.[147]

Thanks to label-free detection, the sensor can be readily adapted for VOC vapor detection.

Another notable hollow-waveguide type is the substrate-integrated hollow waveguide (iHWG), a hollow channel with light propagating through it, directly fabricated in a solid substrate material with a layered structure. Wilk and colleagues[145] introduced a VOC sensor utilizing an iHWG constructed from an Au-coated $AlMg_3$ alloy. This waveguide exhibits a yin-yang shape and is fabricated on an Al substrate, offering a sensor with a centimeter-level footprint [Fig. 12(b)]. IR total reflection occurs on the Au surface. The device boasts a nominal optical absorption path length of over 22 cm and can be configured with an FTIR spectrometer. The certified gas mixture, including isobutylene, methane, cyclopropane, and butane, is analyzed with around 6–11 ppmv LOD. In addition, it is worth mentioning that for the Si-integrated iHWG sensor, Zheng *et al.* demonstrated an NDIR iHWG gas sensor on the Si substrate.[146] After the Si etching process, metal is deposited on the surface. The wafer bonding process was then utilized to bond two wafers with the mirror waveguide channel. NDIR detection is available by employing off-chip sources and detectors. Moreover, Fig. 12(c) illustrates a cross-sectional SEM of the Si-iHWG sensor demonstrated by Fathy *et al.* This 2-cm-length iHWG shows the possibility of integration with a micro-electromechanical systems (MEMS) FTIR.[147] After interacting with butane, the MEMS FTIR could reconstruct the butane absorption spectra ranging from 2 to 4.5 μm.

In these chip-sized hollow-core waveguides, fabrication (e.g., 3D-print) and customization are more accessible and cost-effective. Compared to dielectric core waveguides, these waveguides exhibit insensitive to wavelength variation, with their core serving as the light–matter interaction region. Furthermore, they are easily coupled with off-chip sources and detectors, and both LAS and BAS can be configured with different measurement setups. However, challenges such as lower propagation and bend loss, as well as packaging with IR sources and detectors, still await exploration.

c. Slot and subwavelength structure waveguides. Although the confinement factor Γ in TE mode is not as high as in TM mode, there is a growing interest in exploring TE mode in waveguide sensing to avoid mode conversion from TM to TE for other devices on the same chip. To enhance the sensing effect of TE mode, additional techniques are employed.[148] The middle and right panels in Fig. 13(a) show the potential of energy confinements in slot waveguides and subwavelength structure waveguides (SSWs), aiming to improve the interaction between TE mode and VOCs.[135] Kita *et al.* introduced a judgment

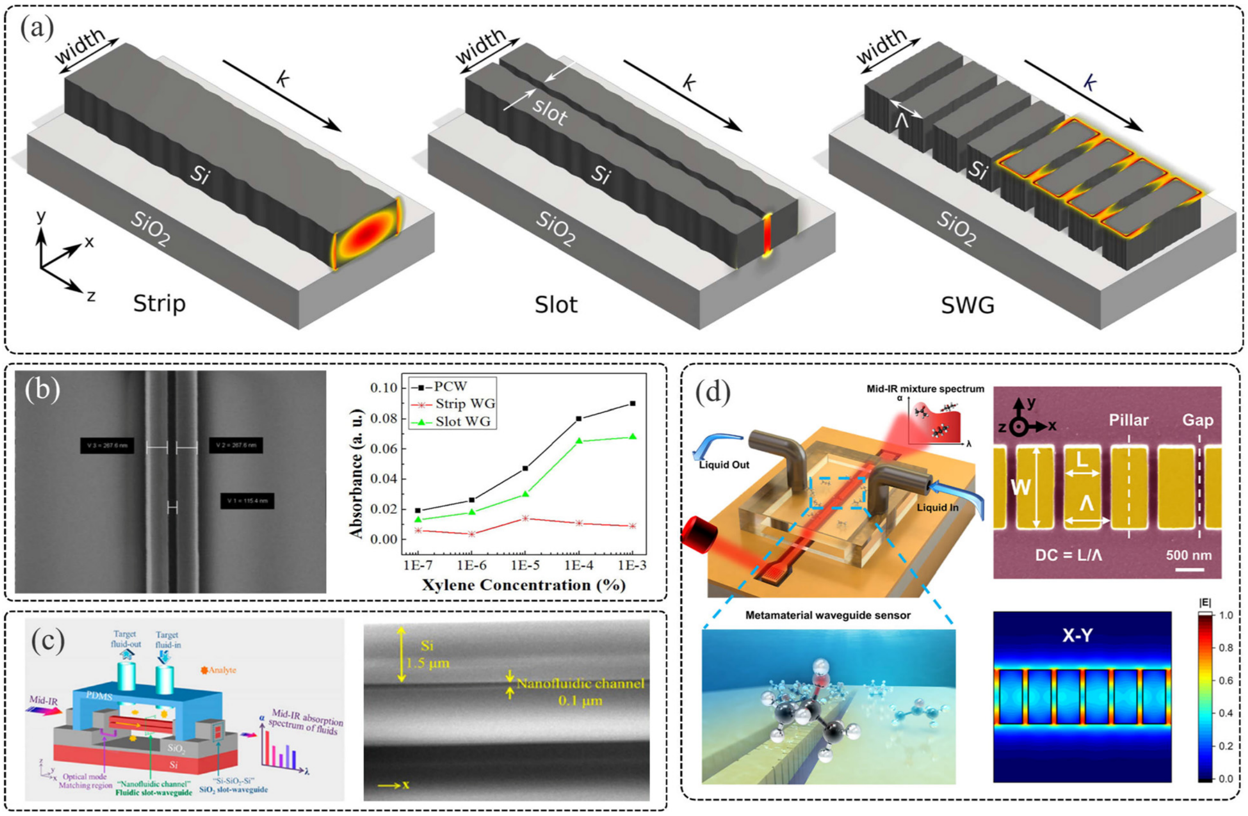

FIG. 13. (a) Electrical field confinement in different waveguides.[135] Left: strip waveguide. Middle: Slot waveguide. Right: SSW. Reprinted with permission from Kita *et al.*, Optica **5**(9), 1046 (2018). Copyright 2018 The Optical Society.[135] (b) NIR slot waveguide-based VOC sensors and Xylene absorbance between different structures.[150] Reprinted with permission from Lai *et al.*, Proc. SPIE **8990**, 89900Z (2014). Copyright 2014 SPIE.[150] (c) Nanofluidic slot waveguide.[151] Reprinted with permission from Lin *et al.*, Nano Lett. **14** (1), 231–238 (2014). Copyright 2014 American Chemical Society.[151] (d) 3D and SEM images of SSW sensor. The energy is mainly confined to the air gap.[157] Reprinted with permission from Zhou *et al.*, ACS Nano **17**(1), 711–724 (2023). Copyright 2023 American Chemical Society.[157]

method, Γ/α, and asserted that a conventional straight waveguide is more suitable for TM mode sensing due to lower loss and higher Γ compared to TE mode, while TE mode achieves higher sensitivity enhancement in slot waveguides and SSWs.[135]

For TE mode in the slot waveguide, the optical energy can be effectively confined in the air slot [the middle panel of Fig. 13(a)].[149] Exploiting this characteristic, Lai *et al.* demonstrated a 300-μm-long NIR slot waveguide absorption spectroscopy liquid sensor.[150] The light–matter interaction between xylene and the NIR light was strengthened 10 times compared to the strip waveguide, achieving an impressive around 1 ppb LOD in the liquid phase, as illustrated in Fig. 13(b). In MIR, Lin *et al.* introduced a MIR nanofluidic channel structure [Fig. 13(c)]. The core sensor device consists of a vertical Si slot waveguide covered by PDMS.[151] When an unknown VOC liquid fills the waveguide slot, it serves to confine the MIR optical energy, enhancing the interaction between the analyte and light. Through measurements of the output power at 3.25 and 3.45 μm (the absorption peaks of n-bromohexane, isopropanol, and toluene) using the TDLAS method, the study successfully demonstrated an enhanced LOD by a factor of 50 compared to air-clad pedestal Si waveguides.

For SWW sensing structures, when the feature size is significantly smaller than the wavelength in the propagation direction (i.e., in the deep-subwavelength region), each element composed of periodic nanostructures in the SWW can be treated as a uniform dielectric element with an effective refractive index value. This structure allows for the energy to exist in the air gaps of subwavelength structure in each effective dielectric element, showing an improved optical spatial overlap and, consequently, enhanced interaction with VOC molecules [the right panel of Fig. 13(a)]. The Bloch mode in periodic structures of SWW plays a crucial role, and the confinement factor Γ is expressed in a 3D form using perturbation theory:

$$\Gamma = \frac{n_g \iiint_A \varepsilon |E|^2 dxdydz}{n_A \iiint_\infty \varepsilon |E|^2 dxdydz}. \tag{12}$$

The energy distribution in the propagation direction must also be taken into account. With a growing demand for NIR PIC, various subwavelength structure devices have been designed for the NIR range.[152–156] In MIR, Zhou *et al.* experimentally demonstrated an SSW sensor on the silicon-on-insulator (SOI) platform within the wavelength range of 3.708–3.803 μm.[157] As shown in Fig. 13(d), the period of these subwavelength structures was designed to be smaller than the Bragg period, ensuring the device operates in the deep-subwavelength region. In addition, the Γ and propagation loss were optimized to confine the energy into the air gap and improve the sensing LOD. With the help of both the machine learning algorithms and this SSW, the ternary mixture (acetone, IPA, glycerin) in water with different mix ratios could be effectively differentiated and broken down into individual component spectra. This approach enables the extraction of individual component spectra below the LOD of 972 ppm (based on a 3σ criterion). Furthermore, Ruan *et al.*[158] designed a subwavelength slot waveguide to further confine the energy in the analyte. Using a strip-to-subwavelength slot mode converter, the mode confinement in Si decreases from 90.9% to 33.8%. However, it is noteworthy that the losses of the slot waveguides and SSWs are higher than conventional strip and ridge waveguides. Particularly in the MIR, significant losses can potentially overshadow the small sensing signal with environmental thermal noise. Therefore, a careful trade-off is necessary to maximize VOC absorption rather than incurring additional transmission loss when designing a corresponding type of VOC sensor.

d. Suspended membrane waveguide. An alternative way to improve Γ involves the use of suspended membrane waveguides, promoting molecule interaction with the entire evanescent field surrounding the waveguide.[159] In particular, employing a suspended Si waveguide on the SOI platform reduces substrate absorption effects, especially at wavelengths exceeding 3.6 μm, while retaining the advantages of the SOI platform. Ottonello-Briano *et al.* developed an MIR absorption spectroscopy sensor featuring a suspended Si waveguide, eliminating substrate restrictions at 4.26 μm [Fig. 14(a)].[160] This free-standing design enhances performance, and a low-index material suspended membrane was also demonstrated. Vlk *et al.* utilized a free-standing high-aspect-ratio tantalum pentoxide (Ta_2O_5) membrane [Fig. 14(b)]. A shallow rib is employed to constrain the TM mode laterally, achieving a TM mode Γ larger than 100%.[161] The suspended membrane reduces TM mode interaction with the substrate, yielding a 2 cm waveguide with a 7-ppm acetylene detection limit at 2.566 μm.

Several studies have explored the combination of subwavelength structures with suspended waveguides. The subwavelength structure is recognized as an effective dielectric to provide optical lateral confinement and mechanical support. Liu *et al.* designed a suspended Si waveguide sensor on a SOI platform at 6 μm, incorporating subwavelength structures [Fig. 14(c)].[162] A spiral structure minimizes device size occupation, and the suspended membrane enhances light–toluene interaction, achieving a 75 ppm LOD at the 6.65 μm absorption peak, with a rapid 0.8 s response time and a 3.4 s recovery time. Additionally, the same group proposed a suspended subwavelength comb waveguide[163] [Fig. 14(d)] operating in the deep-subwavelength region. This design exhibits smaller optical loss, reaching up to 114% Γ and demonstrating a 10 ppm fast detection LOD for acetone at 7.33 μm within 3.8 s response time and a 2.5 ppm LOD within a 20 s average time. Another ultra-broadband suspended rib-SSW sensor on the SOI platform shows multi-VOC spectroscopic sensing potential.[165] At most times, mature SOI platforms and fabrications ensure cost-effectiveness for VOC sensors compared to other platforms. However, Yoo *et al.* expanded the gas sensor to the InGaAs-InP platform for integration with light sources and detectors.[164] Utilizing a suspended SSW [Fig. 14(e)] at 6.15 μm, this platform, transparent across the entire molecular fingerprint region, supports both TE and TM modes, with a 3 mm sensing length achieving 5 ppm sensing LOD. It is crucial to consider structural stability in suspended sensor designs to prevent changes in performance due to external factors such as collisions.

2. Absorption path length enhancement

a. Conventional compact waveguides. While the fabrication of waveguide structures is straightforward, achieving longer absorption path L_a is often required to improve LOD and sensitivity, which can be at odds with the goal of maintaining a small size. In an effort to extend the sensing path, Tombez *et al.* presented a 10 cm long zigzag-shaped methane waveguide sensor [Fig. 15(a)].[137] Much of the research on extended-length waveguide sensing predominantly employs spiral waveguide-based approaches. As depicted in Fig. 15(b),

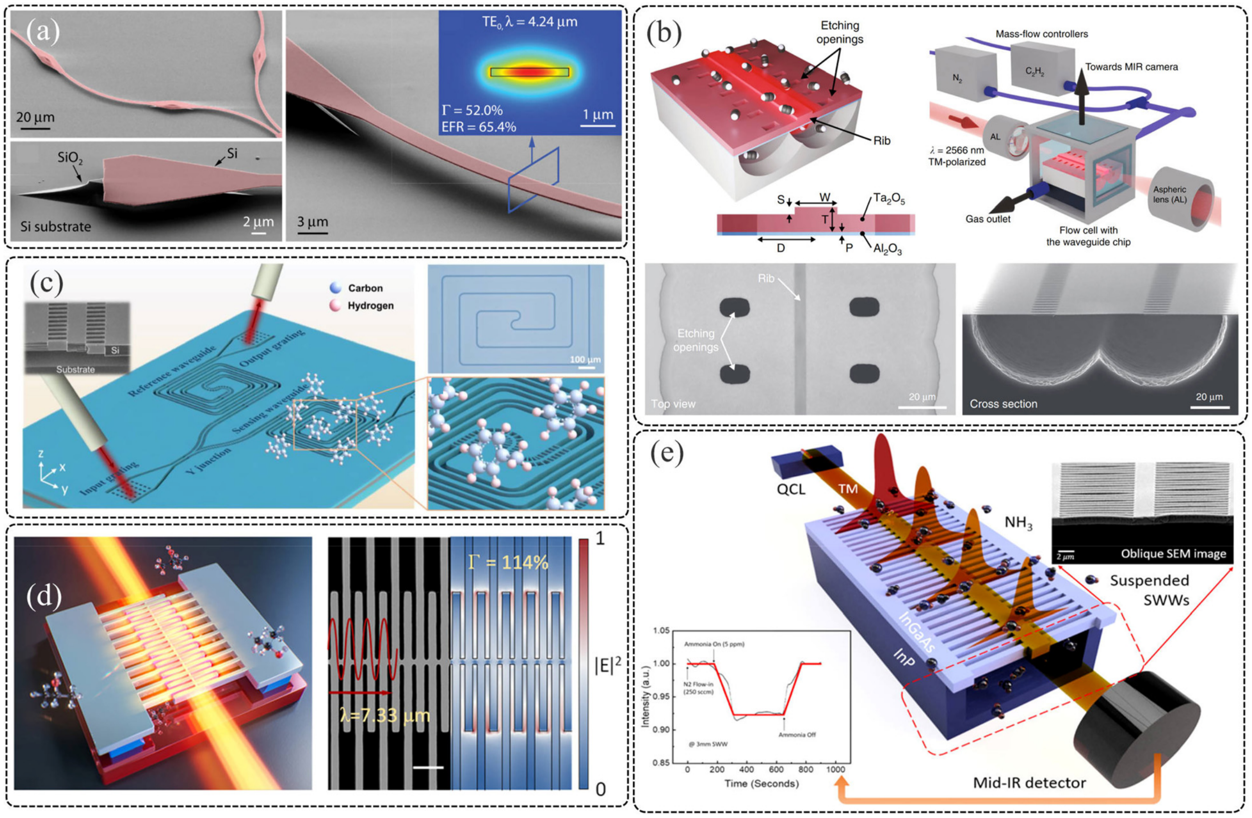

FIG. 14. (a) SEM of suspended membrane waveguides on SOI platform.[160] Reprinted with permission from Ottonello-Briano *et al.*, Opt. Lett. **45**(1), 109 (2019). Copyright 2019 The Optical Society. (b) 3D Views and SEM of suspended tantalum pentoxide membrane waveguides.[161] Reprinted with permission from Vlk *et al.*, Light **10**(1), 26 (2021). Copyright 2021 Authors, licensed under a Creative Commons Attribution (CC BY) license.[161] (c) Suspended membrane spiral waveguides on SOI platform.[162] Reprinted with permission from Liu *et al.*, Nanophotonics **10**(7), 1861–1870 (2021). Copyright 2021 Authors, licensed under a Creative Commons Attribution (CC BY) license.[162] (d) Suspended subwavelength assisted comb waveguides on SOI platform.[163] Reprinted with permission from Liu *et al.*, Nano Lett. **22**(15), 6112–6120 (2022). Copyright 2022 American Chemical Society.[163] (e) Suspended subwavelength membrane waveguides on III–V platform.[164] Reprinted with permission from Yoo *et al.*, ACS Sens. **5**(3), 861–869 (2020). Copyright 2020 American Chemical Society.[164]

Han *et al.* used a broadband ChG spiral waveguide to improve the interaction between methane and the MIR evanescent wave.[53] This design increases the waveguide length while keeping a relatively small footprint. The wavelength range for TDLAS is from 3.28–3.34 μm, with the maximum absorption peak occurring at 3.31 μm, representing methane absorption with a 2.5% LOD. Other platforms, such as germanium-rich silicon–germanium (SiGe) spiral waveguides designed for methane sensing at 5–6 μm, have also been proposed.[138] These waveguides, including

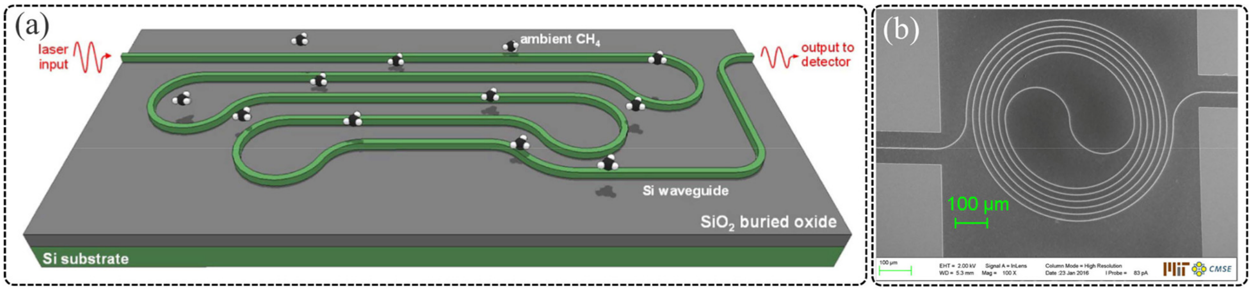

FIG. 15. (a) Zigzag-shaped long Si waveguide methane absorption sensors in the NIR.[137] Reprinted with permission from Tombez *et al.*, Optica **4**(11), 1322 (2017). Copyright 2017 The Optical Society.[137] (b) ChG spiral waveguide methane sensor.[53] Reprinted with permission from Han *et al.*, Appl. Phys. Lett. **108**(14), 141106 (2016). Copyright 2016 AIP Publishing.[53]

bends, contribute to a longer L_a with an acceptable increase in footprint compared to conventional straight waveguides.

b. Cavity-enhanced structures. To achieve a longer absorption length in stringent size constraints, alternative approaches become necessary. The cavity-enhanced technique, known as cavity-enhanced absorption spectroscopy (CEAS), is a widely used method to enhance interaction by significantly increasing the effective optical absorption path length. In free-space optical sensors, the multi-pass gas cell (MPGC) is a representative approach utilizing reflection mirrors to enable light to traverse the sensing cell repeatedly.[166] Another way involves placing the analyte inside the laser cavity, a technique known as intracavity laser sensing.[167] In free-space optical sensors, the Fabry–Pérot cavity is a common choice for CEAS.[166,168–173] For PIC devices, cavities such as ring resonators are commonly employed to effectively increase the optical path length L_a.[174] Taking microring resonators as an example, as shown in Fig. 10(b), this resonator is composed of a bus waveguide, and a waveguide is looped back on itself. When the optical modes meet the condition between resonance wavelengths λ_{res} and round-trip length L,

$$\lambda_{res} = \frac{n_{\mathrm{eff}} L}{m}, \quad m = 1, 2, \ldots, \tag{13}$$

resonance will occur, trapping corresponding energy in the cavity, where n_{eff} is the optical mode effective index and m denotes an integer.[175] The quality factor (Q) is used to measure the sharpness of the resonance at the central wavelength:

$$\mathrm{Q} = \frac{\lambda_{\mathrm{res}}}{\mathrm{FWHM}}, \tag{14}$$

where FWHM denotes full width at half maximum. A higher Q indicates a longer photon lifetime, corresponding to a longer L_a.[175] In the presence of first-order dispersion, the spacing between these resonance wavelengths, which is known as the free spectral range (FSR), is denoted as

$$FSR = \frac{\lambda^2}{n_g L}, \tag{15}$$

where n_g is the mode group index.[175] In addition to adding L_a, this technique supports a resonance linewidth comparable to lasers and thus helps distinguish VOC from spectra.

This extensively studied photonic cavity has reached a high level of maturity and can be readily adapted to various platforms or functional devices in the NIR. Efforts have been made to extend its application into the MIR range. Chen *et al.* demonstrated a heterogeneously integrated cavity sensor for ethanol, toluene, and isopropyl alcohol detection.[176] As shown in Fig. 16(a), the Si microring was transferred from an SOI wafer to a calcium fluoride (CaF_2) substrate. The ring resonator's intrinsic Q is 6.2×10^4 at 5.2 μm, showing a 0.05 ng LOD for liquid-phase ethanol. The discrimination between ethanol and toluene mixtures was achieved by measuring both the resonance wavelength shift and peak extinction ratio change. A related study from the same group reported CHC glass-based resonators with a Q value of 6×10^5 on a CaF_2 substrate.[177] In this case, the measured ethanol absorption was 110 cm^{-1} around 5.2 μm. Additionally, Zhou *et al.* proposed a silicon-rich silicon nitride (SiN_x) serial microring resonator array in MIR.[178] In Fig. 16(b), four different round-trip resonators with different resonance peaks (3.393, 3.416, 3.440, and 3.463 μm) were employed to sample VOCs such as hexane and ethanol. The absorbance ratio between different VOC gases was then compared. It is important to note that in a single sensing cavity, the dynamic sensing range is typically constrained by the FSR. A small FSR may lead to multiple peaks, resulting in the blending of information from different wavelengths. Improving the FSR often requires reducing the cavity length L, but this can decrease the Q due to higher bending loss. Introducing an additional ring with a slightly different FSR coupled to the original resonator, forming a Vernier system, could modify the FSR of this dual-ring system. This alteration allows for a rewritten expression:

$$FSR = \frac{FSR_{\mathrm{ring1}} \times FSR_{\mathrm{ring2}}}{|FSR_{\mathrm{ring1}} + FSR_{\mathrm{ring2}}|}. \tag{16}$$

The cascaded microring resonator will have frequency shifts and peak variations in its resonant peak envelope due to the refractive index change of the cladding and absorption intensity variation caused by the concentration of the VOCs to be measured. The Vernier effect has been experimentally demonstrated in MIR[179] and applied to VOC sensing [Fig. 16(c)].[180] Additionally, thermal-optical (TO) modulation is adopted to achieve overlap between the maximum envelope and absorption peak. In the absorption sensing experiment, the minimum detectable concentration is 1.87% of IPA in acetone.

In addition to the Vernier effect, some structure enhancement methods discussed earlier could also be applied to the microring resonator to improve Γ, such as the slot ring resonator[181] [Fig. 16(d)] and the subwavelength ring resonator[182] [Fig. 16(e)]. These have been experimentally demonstrated in refractive index sensing in the NIR. However, the additional loss introduced by these structures should be considered and optimized to prevent a decrease in Q, resulting in a shorter L_a and wider resonance linewidth. It is worth mentioning another work based on photothermal spectroscopy, as shown in Fig. 16(f), which utilizes a suspended microring cavity as a photothermal spectroscopic transducer on an SOI platform.[183] The transducer relies on a suspended microring resonator with the polymer analyte filling the ring. MIR light is used to heat the analyte, while the NIR light serves as a probe light. This transducer, thanks to temperature sensitivity, bridges the analyte MIR absorption to the power change of the probe without incurring significant additional device costs.

An integrated VOC sensor with CEAS enhancement increases the optical absorption path in a small sensing footprint, and it provides a frequency selection function when using a broadband light source. Nevertheless, it may suffer from temperature-induced stability issues. As environmental temperature changes, the resonance wavelength will shift, causing sensitivity instability. In addition, the components of the underdetermined analytes may contribute to resonance shifts owing to their various refractive indices. However, this influence may be alleviated by employing advanced machine learning algorithms in the analysis of VOCs.

3. Slow-light enhancement

So far, we have explored methods to enhance light–matter interaction primarily based on spatial dimension. Back to the Beer–Lambert law, the group index n_g introduces a temporal dimension, offering an additional avenue for sensitivity improvement. According

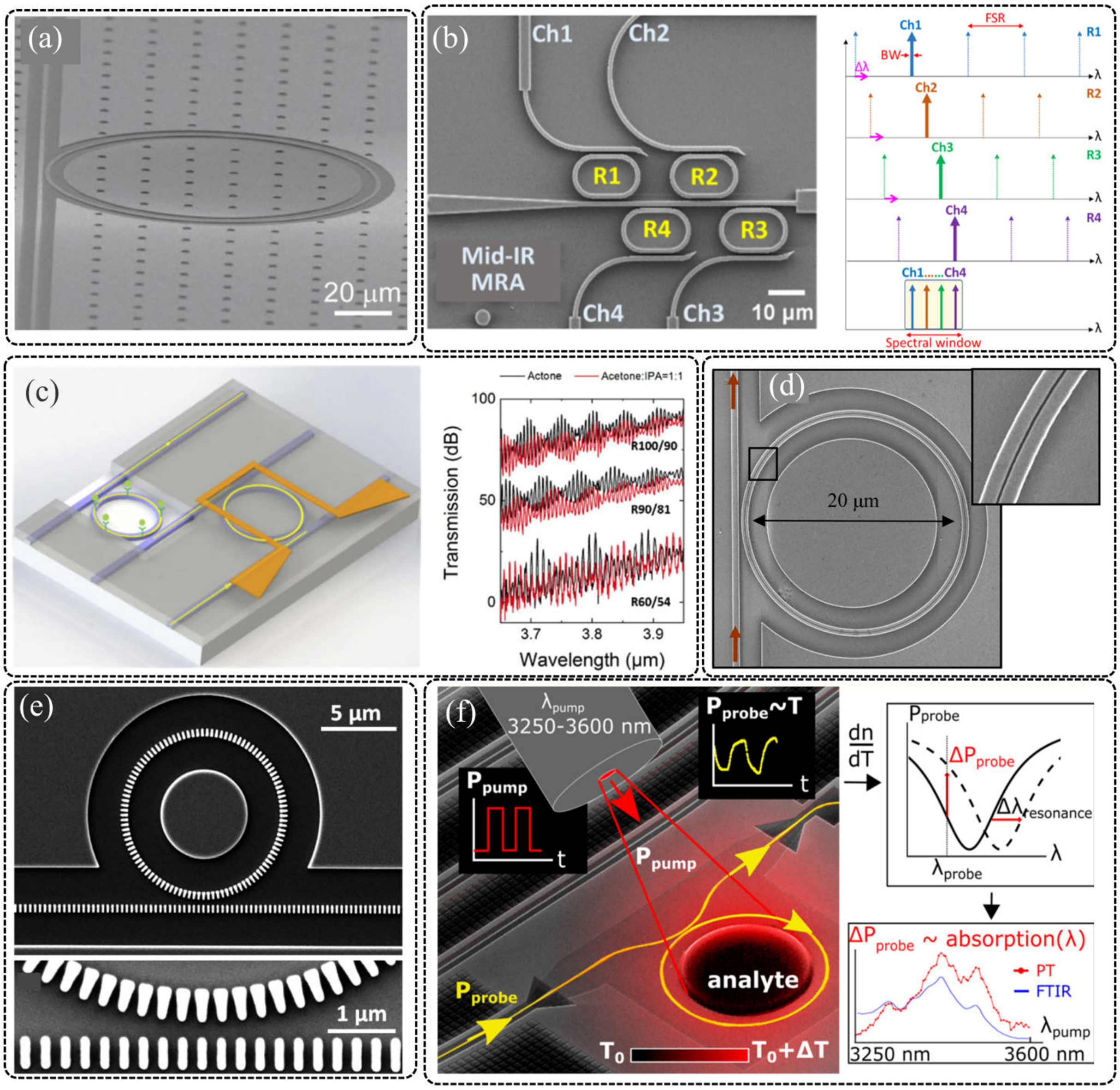

FIG. 16. (a) Heterogeneously integrated Si on CaF_2 substrates CEAS VOCs sensor.[176] Reprinted with permission from Chen *et al.*, ACS Nano **8**(7), 6955–6961 (2014). Copyright 2014 American Chemical Society.[176] (b) SiN_x microring resonator array hexane and ethanol sensor.[178] Reprinted with permission from Zhou *et al.*, Anal. Chem. **94** (31), 11008–11015 (2022). Copyright 2022 American Chemical Society.[178] (c) Vernier effect-based tunable microring MIR sensor.[180] Reprinted with permission from Chang *et al.*, Opt. Express **28**(5), 6251 (2020). Copyright 2020 The Optical Society.[180] (d) Slot ring resonator gas sensor.[181] Reprinted with permission from Robinson *et al.*, Opt. Express **16**(6), 4296–4301 (2008). Copyright 2008 The Optical Society.[181] (e) Subwavelength ring resonator sensor.[182] Reprinted with permission from Wang *et al.*, Opt. Lett. **41**(14), 3375–3378 (2016). Copyright 2016 The Optical Society.[182] (f) IR photothermal spectroscopy gas sensor.[183] Reprinted with permission from Vasiliev *et al.*, ACS Sens. **1** (11), 1301–1307 (2016). Copyright 2016 American Chemical Society.[183]

to the group velocity formula $v_g = c/n_g$, photonic devices with low group velocity, i.e., a high group index, prolong the interaction between energy and matter. This phenomenon, commonly known as the "slow-light effect," extends the duration of light–matter interactions, thereby enhancing sensing performance.

Photonic crystals (PC) are typical slow-light photonic devices, characterized by periodically arranged dielectric media. Designing lattice structures with specific photonic band gaps allows the manipulation of light with different features. When the absorption wavelength is near the PC band edge, the n_g becomes larger, leading to enhanced Γ in the analyte. In the design process of 1D slow-light devices, most previous works employed SSWs as an effective dielectric waveguide, with only a small portion focusing on engineering the 1D slow-light devices.[154,155]

For 2D PCs, hole-type periodic structures are commonly utilized. Introducing a line defect in the bandgap region forms a photonic crystal waveguide (PCW). By choosing a propagation wavelength for this defect mode near the band edge, PCWs exhibit strong light–matter interactions within a compact absorption region [Fig. 10(c)]. Lai *et al.* demonstrated the NIR PCW in liquid xylene spectroscopic sensing, showing superior performance compared to mode confinement enhancement in slot waveguides [Fig. 17(b)].[150] Multiplexed PCWs were employed for simultaneous measurement, achieving a low LOD of 1 ppb for xylene and 10 ppb for trichloroethylene.[184] In the MIR region, Zou *et al.* experimentally demonstrated a PCW on the Si-on-sapphire (SOS) platform [the left panel of Fig. 17(a)], leveraging the slow-light effect to achieve a n_g of ∼30 compared to ∼4 in conventional strip waveguides [the right panel of Fig. 17(a)].[185] To address the challenge of an indistinct band edge caused by the large n_g contrast between PCW and strip waveguides, which influences the sensing wavelength accuracy, a PCW taper was employed to minimize the coupling loss through edge tuning, resulting in sharp band edges.[186] In addition to the hole-type PCW, nanotube PCs were also demonstrated at the wavelength of 5400 nm to detect the propylene with a slow-light effect.[187]

Similarly, the strategies used in conventional waveguides can be extended to the PCWs. Lai *et al.* demonstrated a NIR slot PCW for methane spectroscopic sensing, incorporating a mode converter to transition from common waveguide mode to slot mode [Fig. 17(b)].[188] The combined effects of slow-light and slot enhancement contributed to a low LOD of 100 ppm for methane. The group also conducted a comparative study between slot and holey PCWs on the SOS platform.[189] In this investigation, the electrical field was highly confined in the PCW center, characterized by an air slot or holes [Fig. 17(c)], resulting in a 10 ppm LOD when testing triethyl-phosphate vapor. While slot PCWs exhibited a higher peak electrical field compared to holey PCWs, the propagation loss in holey PCWs (15 dB/cm) was three times lower than that in slot PCWs (55 dB/cm), supporting a higher L_a. Similarly, on a SOI platform, a holey PCW was developed to detecting ethanol at 3.4 μm, featuring a low LOD of 250 ppb.[190] In addition to SSWs discussed in Subsection III B 1, Yoo *et al.* constructed suspended holey PCWs on an InGaAs-InP platform within the same work [Fig. 17(d)].[164] Compared to SWWs requiring a 3 mm length to achieve a 5 ppm LOD, holey PCWs only necessitated a 1 mm length. Nevertheless, despite the 39.1 dB/cm propagation loss in holey PCWs, SWWs exhibited a significantly lower propagation loss of 4.1 dB/cm. Beyond evanescent field enhancement, Shankar *et al.* reported the first L3 PC microcavity on the SOI platform at 4–5 μm with a quality factor of 13 600.[191] Zou *et al.* demonstrated an L21 PC microcavity on the SOS platform with a quality factor of around 3500 at 3.43 μm [Fig. 17(e)].[192] Kassa-Baghdouche simulated the design of the H1 microcavity spectroscopic gas sensor with optimized Q at 3.7 μm.[193] Thanks to their small mode volume and high Q factors, these microcavities could achieve strong light–matter interaction. The combination of microcavity and PCW holds the potential to yield superior sensing outcomes by leveraging the advantages of both slow-light effects and CEAS.

It is important to highlight that while PCs offer significant enhancements in terms of the group index, this improvement is often accompanied by an increase in propagation loss. In this scenario, even when assisted by other methods for evanescent field enhancement, a substantial portion of the improvement comes at the expense of increased propagation loss. As a result, a trade-off of Γ/α must be carefully considered to prevent the loss of sensitivity in the detection of trace VOC gases.

In conclusion, Table IV summarizes the performance of PIC sensors for VOC sensing. In addition, Fig. 18 provides an overview of the corresponding advantages and disadvantages of the discussed enhancement methods.

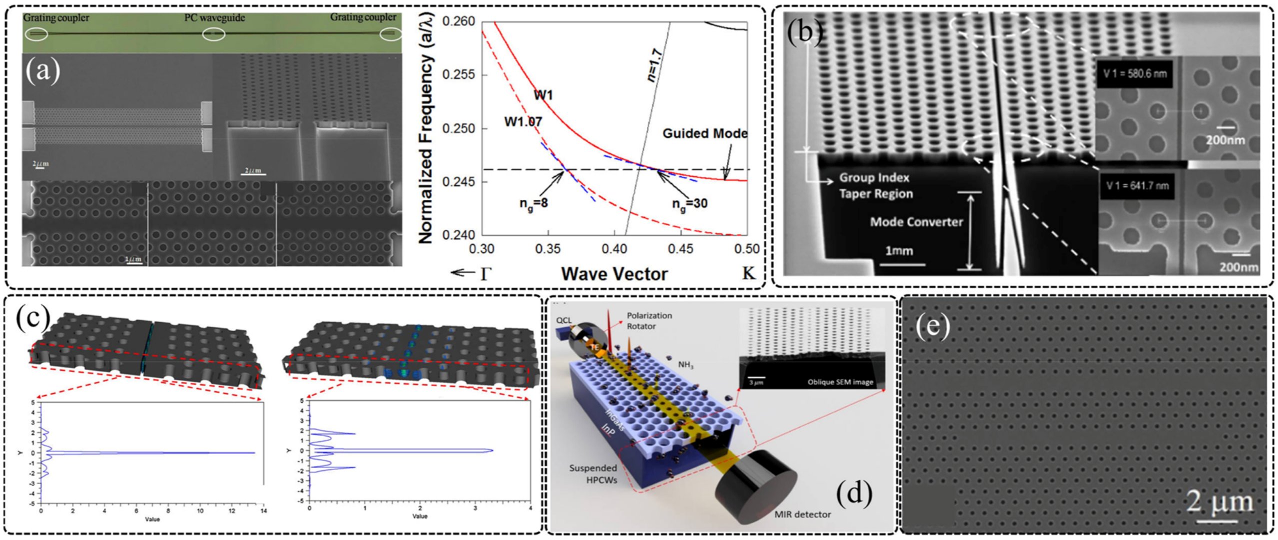

FIG. 17. Various configurations of PCWs and their applications: (a) PCW with a high group index.[185] Reprinted with permission from Zou *et al.*, Opt. Express **23**(5), 6965 (2015). Copyright 2015 The Optical Society.[185] (b) Slot PCW for methane detection.[188] Reprinted with permission from Lai *et al.*, Opt. Lett. **36**(6), 984 (2011). Copyright 2011 The Optical Society.[188] (c) High-energy confinement in slot and holey PCW.[189] Reprinted with permission from Zou *et al.*, Sens. Actuators, B **221**, 1094–1103 (2015). Copyright 2015 Elsevier.[189] (d) Suspended holey PCW on the III–V platform used for gas sensing.[164] Reprinted with permission from Yoo *et al.*, ACS Sens. **5**(3), 861–869 (2020). Copyright 2020 American Chemical Society.[164] (e) SEM image of a microcavity-coupled PCW.[192] Reprinted with permission from Zou *et al.*, Appl. Phys. Lett. **107**(8), 081109 (2015). Copyright 2015 AIP Publishing.[192]

TABLE IV. Performance of PIC-based IR absorption VOC sensors. WG: waveguide, L: liquid, G: gas, RT: response time, and AT: average time.

Work	Structure	Method	Waveband(μm)	Phase	LOD (Analyte)	RT / AT
137	Si WG	DAS	1.65	G	20 ppmv (methane)	10^3 s (AT)
140	ChG WG	DAS	3.4–3.5	G	N/A (acetone and ethanol)	<5 s (RT)
53	ChG WG	DAS	3.28–3.34	G	2.5% (methane)	NA
66	ChG WG	WMS	3.291	G	0.17% (methane)	0.2 s
143	Nb_2O_5 WG	WMS	3.291	G	384 ppm (methane)	61.2 s
150	Si Slot WG	BAS	1.674	L	1 ppb (xylene)	N/A
151	Si Slot WG	DAS	3.1–3.6	L	<5 μl/ml (n-bromohexane, toluene, isopropanol)	N/A
157	Si SSW	DAS	3.708–3.803	L	<972 ppm (glycerin)	NA
145	Au-coated AlMg3 alloy iHWG	FTIR	2.63–16.6	G	6–11 ppmv (cyclopropane, butane, isobutylene, methane)	1200s (AT)
147	Si-iHWG	FTIR	2–4.5	G	N/A (butane)	N/A
161	Ta_2O_5 suspended WG	DAS	2.566	G	7 ppm (acetylene)	25 s (AT)
162	Si suspended SSW	DAS	6.65	G	75 ppm (toluene)	0.8 s
163	Si suspended SSW	DAS	7.33	G	2.5 ppm (acetone)	20 s (AT)
178	SiN_x Ring array	DAS	3.3–3.6	G	N/A (ethanol, hexane)	N/A
176	Si Ring	DAS	5.14–5.26	L	0.05, 0.06, and 0.09 ng (ethanol, toluene, and IPA)	N/A
177	ChG micro-disk	DAS	5.184–5.190	L	N/A (ethanol)	N/A
180	Si cascaded ring	DAS	3.65–3.95	L	1.87 % (IPA)	N/A
150	Si PCW	BAS	1.674	L	1 ppb (xylene)	N/A
184	Si multiplexed PCW	BAS	1.644, 1.674	L	1 ppb (xylene) 10 ppb (Trichloroethylene)	N/A
188	Si slot PCW	BAS	1.665–1.668	G	100 ppm (methane)	N/A
194	Si slot PCW	BAS	1.674	L	100 ppb (xylene)	N/A
189	Si holey PCW	DAS	3.43	G	10 ppm (triethyl phosphate)	N/A
190	Si holey PCW	DAS	3.4	G	250 ppb (ethanol)	20–30 s (RT)

C. Surface-enhanced infrared absorption (SEIRA) sensors

In the 1980s, Hartstein and his team discovered that a randomly arranged thin film of (silver)Ag nanoparticles could significantly enhance IR absorption.[195] Subsequent studies on this phenomenon led to the development of a powerful tool known as surface-enhanced infrared absorption (SEIRA) spectroscopy, demonstrating sensitivity enhancements ranging from 10× to 500×, attributed to surface roughness and plasmon enhancement.[196] Plasmon enhancement, primarily driven by resonance field enhancement, plays a crucial role in improving light–matter interactions.[197] As depicted in Fig. 19, this enhancement manifests in two basic forms in miniaturized sensors: surface plasmon polaritons (SPPs) and localized surface plasmon resonance (LSPR), where plasmon refers to the free electrons oscillation in conducting materials.

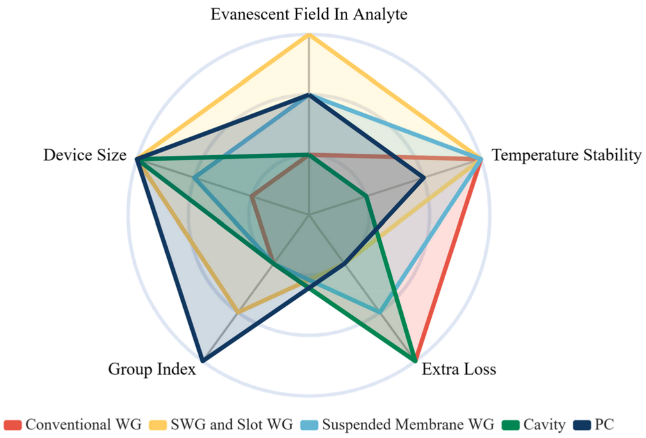

FIG. 18. Structure performance of IR absorption spectroscopy-based PIC sensors. Larger range means better performance.

Total internal reflection typically occurs at the boundary between two dielectric materials, particularly when visible and IR light incident from a medium with a high refractive index to one with a lower refractive index, and the incident angle surpasses the critical angle. However, visible and IR light cannot propagate in metals like Au, resulting in strong reflection at most angles due to the metal's negative permittivity. However, the metal–dielectric boundary supports light propagation, with evanescent fields present on both sides, as shown in Fig. 19(a). Proper excitation through evanescent waves or gratings can lead to a surface-traveling wave, initiating surface plasmon resonance (SPR). The subwavelength confinement at the metal–dielectric boundary allows this traveling wave with a large evanescent field in the dielectric to propagate along the boundary.

An inverse correlation exists between the size of the evanescent field in different materials and the absolute value of their dielectric

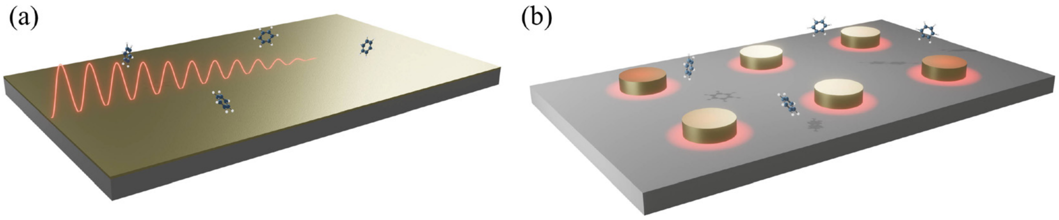

FIG. 19. Illustration of surface plasmon resonance based on-chip absorption spectroscopy. This resonance significantly enhances the interaction between light and the substance at the ultrafine scale. (a) Surface plasmon resonance (SPR). (b) Localized surface plasmon resonance (LSPR).

constant. For common noble metals like Au, the evanescent field in the dielectric could extend to approximately 1 μm in the NIR. However, precise coupling into SPP requires momentum matching, achieved through configurations like Kretschmann or Otto, grating, and others.[198] The incident angle in conventional prism excitation is fixed for the corresponding resonance frequency, often making this condition stringent. Prism configuration SPPs used in VOC detection are typically resonance shift-based, where changes in VOC composition and concentration alter reflection intensity or angle due to wavevector mismatch.

When the SPR travels along the boundary, it experiences high attenuation compared to localized surface plasmon resonance (LSPR) occurring on metallic structures with subwavelength dimensions, as shown in Fig. 19(b). In addition, SPR has limitations compared to LSPR, such as insufficient electrical field enhancement.[199] LSPR offers a resonance field range is around 20 nm, while the electrical field in SPR extends to 1 μm in the NIR. This distinction allows LSPR to mitigate bulk effects that exist in SPR.[200] Consequently, numerous LSPR metasurface devices have been developed for VOC sensing applications and demonstrated in the NIR.[201] Unlike SPR, which relies on a specific coupling angle for a given wavelength, LSPR accommodates broadband sources from the top. As the analyte adheres to the metal surface, the resonance shifts, leading to a decay in intensity due to changes in refractive index. It is essential to note that relying solely on index sensing is limiting due to its lack of selectivity. Incorporating plasmons for absorption spectroscopy in the MIR waveband, i.e., utilization of SEIRA in plasmon resonance in the MIR waveband, would significantly enhance the functionality and precision of measurements.

1. Waveguide-integrated SEIRA

In the realm of waveguide-integrated SEIRA for VOC sensing, SPR can be effectively generated by using plasmonic waveguides.[202] The plasmonic mode is closely bound to the metal while keeping propagation in the waveguide. An illustrative example comes from Luo *et al.*, who showcased an on-chip hybrid photonic–plasmonic light concentrator by incorporating an Au nanotaper onto a Si photonic waveguide [Fig. 20(a)].[203] This Au taper facilitates the seamless transfer of photonic dielectric modes into the plasmonic mode, resulting in an exceptional field enhancement at the taper tip. Meanwhile, Chen *et al.* proposed a waveguide-integrated Au nanorod plasmonic resonator sensor [Fig. 20(b)].[204] A set of Au antennae with a 30 nm slot was intricately fabricated on a Si waveguide. Plasmonic resonance is induced at the nanogap, creating a field hotspot with a remarkable 3600-fold enhancement factor compared to an evanescent waveguide sensor. The nanorod's compact 2 μm^2 footprint contributes to minimizing optical loss. In their TDLAS experiment, organic compound films served as an analyte for detecting C–H bonds.

In addition to Si-metal plasmons, III–V materials offer a suitable platform for SEIRA sensing. Schwarz *et al.* demonstrated a monolithically integrated quantum cascade lasers/detectors (QCL/QCD) SPP absorption sensor operating in the wavelength range of 6.4–6.6 μm on the III–V platform [Fig. 20(c)].[205] Their bi-functional QCL/QCD design facilitates the direct coupling of light to the waveguide. To optimize coupling efficiency, a SiN layer was deposited on the Au layer. The sensor successfully analyzed a liquid mixture of ethanol and water, demonstrating the ability to detect up to 60% H_2O concentration in ethanol with a resolution of 0.06%. Notably, the polarization state of the QCL aligns with the TM mode, which is conducive to SPP coupling in the plasmonic waveguide. Furthermore, Pi *et al.* employed an Ag island film on a ChG waveguide to enhance VOC detection efficiency through waveguide surface resonance [Fig. 20(d)].[206] The 1.8 nm thickness Ag film struck a balance between transmission loss and field enhancement. In DAS experiments, the Ag film demonstrated absorption enhancements exceeding 1.5 for ethanol and 2.3 for methane in NIR and MIR, respectively, compared to waveguides without the film. The response time was approximately 0.2 s.

2. Out-of-surface SEIRA

Another SEIRA sensor type involves out-of-surface detection using metamaterials, which are artificially engineered materials with quasi-homogeneous material properties. The design of the unit cell shape or geometry allows for different functions and optical responses. The resonant behavior in metamaterial, similar to LSPR, amplifies the local field and is influenced by pattern shape, distance, and plasmonic materials.[207] After interacting with the analyte, transmission or reflection spectra of an incident IR beam are measured, often accompanied by techniques like FTIR or filter arrays for broadband sensing results. Dong *et al.* designed a bowtie-shaped Au structure with a sub-3 nm gap to form a hotspot with more than 10^7 SEIRA enhancements.[208] The resonance wavelength can be tuned by changing the geometric parameters, optimized for detecting strong vibrational modes of alkane chains, nitrile groups, and phosphonate compounds for organic compound detection. Brown *et al.*[209] demonstrated fan-shaped Au antennas as a SEIRA sensor [Fig. 21(a)]. In addition to the hotspot between these Au fans, an Au reflection layer was applied as a metamaterial perfect absorber (MPA), making the reflection close to zero to provide additional field enhancement, and then, the C–H bond vibration of octadecanethiol was detected. Machine learning algorithms, such as those used by Ren *et al.*, can be suitable for gas component analysis with metamaterials. They proposed a wavelength multiplexed hook

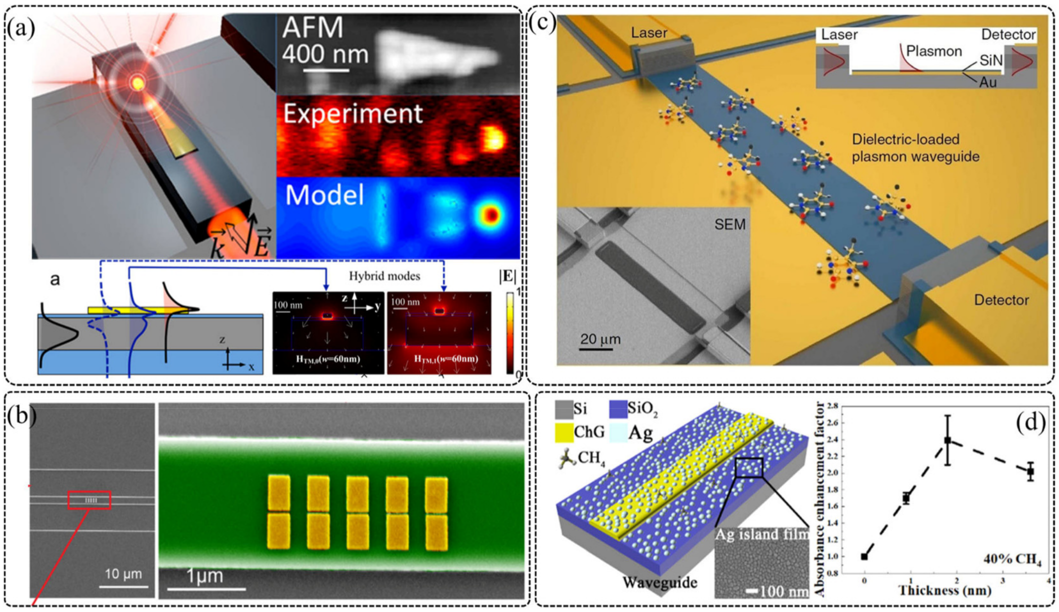

FIG. 20. Plasmonic waveguides. (a) Photonic–plasmonic light concentrator.[203] Reprinted with permission from Luo *et al.*, Nano Lett. **15**(2), 849–856 (2015). Copyright 2015 American Chemical Society.[203] (b) Waveguide-integrated Au nanorod plasmonic resonator sensor.[204] Reprinted with permission from Chen *et al.*, Nano Lett. **18**(12), 7601–7608 (2018). Copyright 2018 American Chemical Society.[204] (c) Plasmonic waveguide sensor integrated with QCL/QCD.[205] Reprinted with permission from Schwarz *et al.*, Nat. Commun. **5**(1), 4085 (2014). Copyright 2014 Authors, licensed under a Creative Commons Attribution (CC BY) license.[205] (d) Ag island film-based SEIRA for methane sensing.[206] Reprinted with permission from Pi *et al.*, ACS Appl. Mater. Interfaces **13**(27), 32555–32563 (2021). Copyright 2021 American Chemical Society.[206]

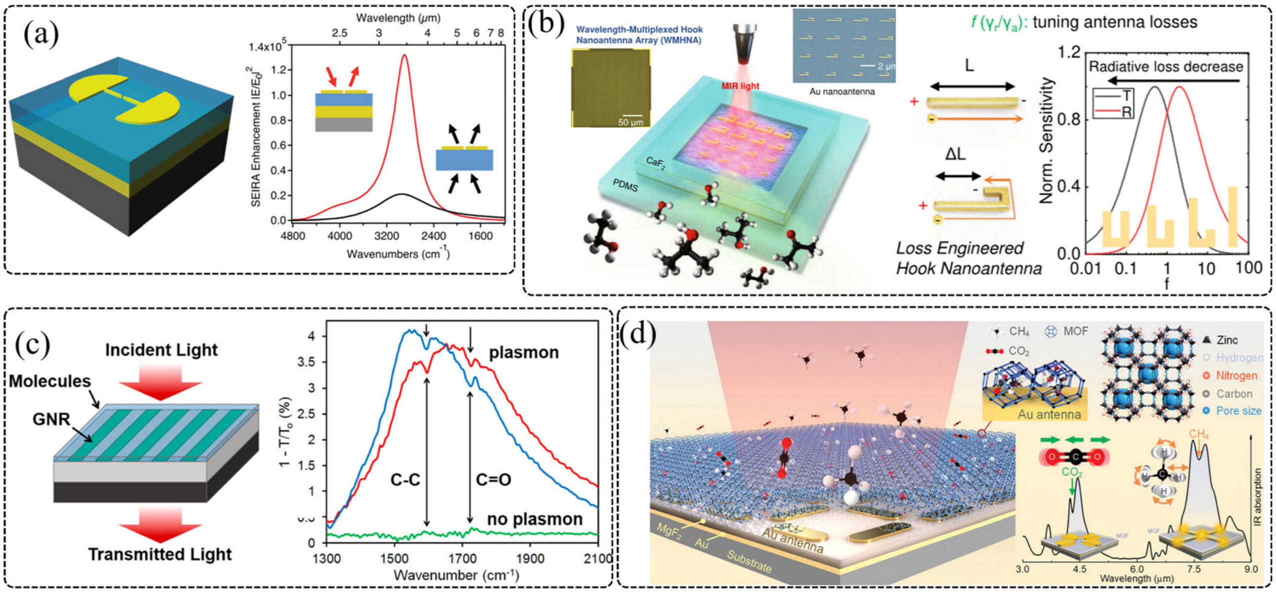

FIG. 21. Metamaterial and 2D material VOC sensor. (a) Fan-shaped plasmonic sensors.[209] Reprinted with permission from Brown *et al.*, Nano Lett. **15**(2), 849–856 (2015). Copyright 2015 American Chemical Society.[209] (b) Hook nanoantenna array metasurface sensor.[210] Reprinted with permission from Ren *et al.*, Nat. Commun. **13**(1), 3859 (2022). Copyright 2022 Authors, licensed under a Creative Commons Attribution (CC BY) license.[210] (c) Ribbon-shaped graphene plasmonic sensor for organic vapor sensing.[219] Reprinted with permission from Farmer *et al.*, ACS Photonics **3**(4), 553–557 (2016). Copyright 2016 American Chemical Society.[219] (d) MOF-assisted SEIRA metamaterial multi-gas sensors.[224] Reprinted with permission from Zhou *et al.*, Adv. Sci. **7**(20), 2001173 (2020). Copyright 2020 Authors, licensed under a Creative Commons Attribution (CC BY) license.[224]

nanoantenna array metasurface to implement molecular recognition from mixed VOCs.[210] Sixteen Au hook antennas with a gradient change of length were fabricated on a CaF_2 substrate and applied in the 6–9 μm sensing wavelength range [Fig. 21(b)]. A radiative loss-tuning engineer was adopted to optimize the absorption signal by changing ΔL, and the simulated field enhancement could achieve 10^5 orders. The proposed metamaterial has been functionalized for microfluidic VOC detection purpose. Reflection spectra were measured to recover the composition. By leveraging principal component analysis (PCA) in tandem with support vector machine (SVM) algorithms, a discernment accuracy of 100% becomes achievable in distinguishing various VOCs (such as methanol, ethanol, and isopropanol), despite their closely resembling absorption features.

While many metal species have been applied to NIR LSPR,[211] free charge carriers in these metals decide the plasma wavelengths, and they may have different optical responses in the MIR.[212] The larger negative permittivity of metals, e.g., Au, contributes to a weak bound in the MIR and a large mode volume.[213] Materials whose plasma frequencies are close to the MIR work better for VOC sensing. Thus, materials like doped III–V semiconductor[214] and high-doped Si[215] are alternatives for MIR plasmon. Additionally, 2D materials have been explored in IR as a type of plasmon material due to their favorable features. Graphene, a typical 2D material, has high electron mobility and a zero-energy bandgap at the Dirac point, supporting MIR plasmonic mode.[216] This graphene plasmonic mode provides an ideal platform for SEIRA.[217] There exists a direct correlation between the doping level in graphene and the plasma frequency. Achieving a spectrometer-free SEIRA by controlling and monitoring doping levels is possible.[218] Farmer *et al.* reported a MIR gas sensor based on graphene plasmons with a 50 zeptomol/μm^2 LOD [Fig. 21(c)].[219] The graphene nanoribbons are located on the top of the SiO_2/Si substrate, and a 0.6-nm-thick perylene-3,4,9,10-tetracarboxylic dianhydride (PTCDA) deposited on the graphene could be detected. In addition, the vibration absorption spectra of C=O and C−C from acetone and hexane vapor are analyzed by FTIR from 1300 to 2700 cm^{-1}. Graphene was also used directly or integrated with polyethylenimine (PEI) to analyze other molecules like SO_2 and CO_2.[220,221]

Metal-organic frameworks (MOFs), another 2D material type, exhibit high performance in terms of gas affinity, absorption selectivity, and reverse interaction.[222] Composed of organic ligands and inorganic metal clusters, MOFs can be customized for specific molecules, and their porous structure enhances sensing absorption signals. Numerous gas-sensing applications using MOFs have been proven effective. For instance, the zeolitic imidazolate framework (ZIF-8) boasts a high surface area (1840 m^2/g), good water stability, and high light transmittance in the NIR. MOF photonic index sensing for VOCs has demonstrated the detection of various VOCs at levels ranging from 29 to 99 ppb, showing its accessibility.[223] A MOF-SEIRA study also illustrates its effectiveness in greenhouse gas detection. Zhou *et al.*[224] demonstrated the use of porous ZIF-8 attached to an Au resonance antenna metasurface. In comparison with conventional SEIRA approaches, MOFs selectively eliminate absorption noise signals from other gas molecules in the spectrum. As depicted in Fig. 21(d), the target gas capture feature of MOFs enhances the absorption coupling between gas and IR light. This structure provides two sensing wavebands of CH_4 and CO_2, achieving a maximum 1500-fold near-field intensity enhancement.

For waveguide-integrated SEIRA, achieving a fully miniaturized VOC sensing system is more feasible. However, consideration must be given to the power budget and SNR. In the context of surface detection SEIRA, losses become a secondary mitigating factor. Typically, the light from the integrated source within a chip cannot directly propagate through the sensor unit. An alternative way is to fabricate thermal emitters and sensors in a reflectance cavity.

IV. RESTRICTION AND PERSPECTIVES

In Secs. II and III, we review the IR absorption-based sensing mechanism and the miniaturization engineering efforts aimed at developing techniques to enable label-free optical sensing systems, respectively. However, for a comprehensive sensing system, it is imperative to consider not only the interactive structure but also the source and detection components. While out-of-chip sources and detecting systems could fulfill the functions, a monolithic integrated system offers certain advantages, such as structural stability and a reduced footprint cost. Therefore, as illustrated in Fig. 22, we aim to provide an extended review of the progress in chip-integrated light sources and detection devices.

A. Light source

In sensing applications, light sources are categorized into two main types: narrowband and broadband sources, aligning with the measurement strategies outlined in Sec. II. The high luminous efficiency of both types significantly benefits the detection power budget, particularly for PIC-type sensors. Increased output power directly enhances the SNR, thereby improving the LOD.

In narrowband measurement configurations, a tunable laser emits coherent, highly directional, and high-energy-density light from its FP cavity. These light sources in the NIR are well-developed for commercial applications and index-based sensing. Current research focuses on developing monolithic integrated lasers. While the Si-based platform is mature and cost-effective for passive devices, Si's low light-emitting efficiency as a laser source, owing to its indirect band,[234] presents a challenge. In addition, the lattice mismatch between Si and material like III–V hinders the direct fabrication of laser source on Si. Two current approaches to monolithic integration involve using a platform with the same or cognate material as the source, such as InP,[205] or employing heterogeneous integration by bonding the III–V layer on Si or direct heteroepitaxial growing III–V on Si.[235] Since the primary vibration regions of most organic molecules are in the MIR, tunable MIR lasers, specifically III–V compound semiconductor (InP, GaSb, InAs/GaInSb) QCL and interband cascade lasers (ICL), are essential for VOC detection.[236] While some QCL and ICL discrete MIR laser sources are commercially available, monolithic integrated MIR sources are still in the research phase.

Broadband light sources, such as SiC blackbody thermal radiation, are widely employed in sensing systems, e.g., FTIR system, to cover a wide wavelength range. However, the spectral power distribution of this emitter may not be sufficient for a miniaturized optical sensor system[237] due to poor coupling efficiency between the thermal source and integrated devices. In miniaturized VOC sensor systems, either coupling or transmission incurs losses, making trace-level VOC detection challenging. Furthermore, low power consumption, corresponding to high luminous efficiency, is crucial for an integrated optical sensor. In one study, a MEMS thermal emitter demonstrated a

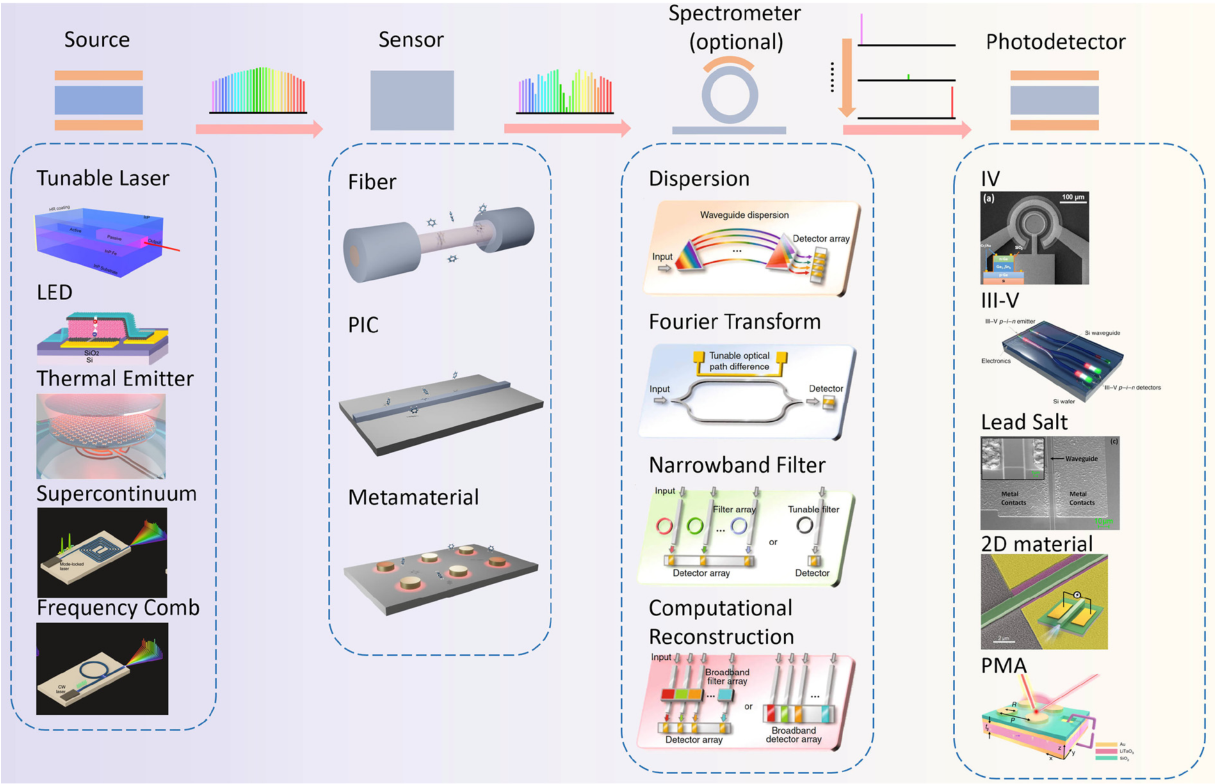

FIG. 22. Perspectives of miniaturized integration VOC sensing system configuration.[45,225–233] Reprinted with permission from Wang *et al.*, ACS Photonics **9**(2), 426–431 (2022). Copyright 2022 American Chemical Society.[225] Reprinted with permission from Chang *et al.*, Nano Lett. **20**(9), 6824–6830 (2020). Copyright 2020 American Chemical Society.[226] Reprinted with permission from Lochbaum *et al.*, ACS Photonics **4**(6), 1371–1380 (2017). Copyright 2017 American Chemical Society.[227] Reprinted with permission from Gaeta *et al.*, Nat. Photonics **13**(3), 158–169 (2019). Copyright 2019 Springer Nature.[228] Reprinted with permission from Li *et al.*, Light **11**(1), 174 (2022). Copyright 2022 Authors, licensed under a Creative Commons Attribution (CC BY) license.[45] Reprinted with permission from Tran *et al.*, Front. Mater. **6**, (2019). Copyright 2019 Authors, licensed under a Creative Commons Attribution (CC BY) license.[229] Reprinted with permission from Mauthe *et al.*, Nat. Commun. **11**(1), 4565 (2020). Copyright 2020 Authors, licensed under a Creative Commons Attribution (CC BY) license.[230] Reprinted with permission from Han *et al.*, Appl. Phys. Lett. **109**(7), 071111 (2016). Copyright 2016 AIP Publishing.[231] Reprinted with permission from Lin *et al.*, Nat. Photonics **11**(12), 798–805 (2017). Copyright 2017 Springer Nature.[232] Reprinted with permission from Tan *et al.*, Nat. Commun. **11**(1), 5245 (2020). Copyright 2020 Authors, licensed under a Creative Commons Attribution (CC BY) license.[233]

blueprint for a low-cost gas sensor integrating a metamaterial sensing chip in a gas cell for out-of-plane detection.[227] In the NIR, LEDs, particularly those made of direct bandgap semiconductors like gallium arsenide (GaAs) or aluminum gallium arsenide (AlGaAs), are widely used broadband sources. For the MIR spectrum, InGaAsSb-based LED sources have been applied to gas and liquid sensors.[238] Additionally, 2D materials, such as waveguide-integrated black phosphorus MIR LED based on van der Waals heterostructures,[226] offer relatively straightforward chip-integrated methods and operate at room temperature However, the luminous power for MIR LEDs remains a challenge, limiting the LOD of sensing systems.

Beyond traditional sources, nonlinear processes like supercontinuum and frequency comb (FC), offer alternatives for building miniaturized broadband light sources. Most miniaturized supercontinuum light sources are fiber-based, utilizing materials like ChG fiber to generate spectra ranging from 2 to 12 μm through nonlinear processes like self-phase modulation (SPM). Recently, on-chip supercontinuum generations in IR using Ge-rich graded SiGe[54] and Si_3N_4[239] were demonstrated. On-chip FCs, generated using microring resonators and based on the Kerr effect,[240] show potential not only in the NIR but also in the MIR spectrum on ChG and III–V chips for VOC absorption sensing.[225,241] These nonlinear processes, requiring a light pump rather than an electrical pump, necessitate a front-mounted laser. Notably, there has been a successful demonstration of a monolithic integrated laser alongside an optical frequency comb,[242] offering a powerful tool for miniaturized multi-VOC identification for their direct broadband spectrum generation in a waveguide.

B. Photodetectors

Optical detection plays a critical role in a VOC sensing system, complementing the importance of light sources for signal readout. A swift detector response is particularly crucial for real-time monitoring of hazardous VOCs, e.g., flammable gas detection. Additionally, in scenarios where the source may not provide sufficient power for the sensor, background thermal noise could overshadow the signal. A high-sensitivity detector alleviates the need for ample source power, improves the SNR, and enables trace VOC analysis. Commercially available high-speed and sensitive photodiodes in the NIR meet the demands of optical communication. However, miniaturized absorption measurement in the MIR presents challenges. Achieving low dark current and noise often requires temperature control, sometimes even under extremely cryogenic conditions. Yet, for practical field applications, operating at room temperature is essential, contributing to the realization of compact and portable VOC sensing systems.

Ge-based photodetectors have demonstrated high responsibility, fast response, and low noise in the NIR.[243] An advantage feature is Ge is CMOS-compatible, being in the same group as Si, making it widely used in PICs. In the MIR, GeSn alloy with varying Sn compositions enables detection beyond the 3-μm region.[244] III–V material-based photodiodes, including InGaAs p–i–n photodiodes,[230] find frequent use in the NIR detection. In addition, type-II superlattice MIR detectors based on III–V material have shown advanced progress.[245] For MIR waveguide detection, heterogeneous integration methods, similar to those employed for light sources, offer effective pathways for achieving monolithic integration.[246] The HgCdTe alloy (MCT) proposed by Lawson *et al.* is a well-established option with mature commercial schemes.[247] Its direct bandgap is instrumental in achieving high quantum efficiency, and its tunable bandgap width allows coverage across a broad MIR spectrum. With attributes like high electron mobility, fast response, and low dark current, MCT stands as the primary method for MIR detection.[248] Lead salt (PbTe) detectors, known for low cost, room temperature operation, and high detectivity, offer a cost-effective waveguide-integrated solution and find extensive use in the 1–5 μm spectral range.[231,249–251] Nevertheless, their response time limitations restrict their application to low-speed scenarios. Two-dimensional (2D) materials show advantages not only in IR sources but also in detection,[252] especially for waveguide integration.[253] Miniaturized waveguide-integrated detectors have been applied not only to Si platforms but also to ChG glass, extending wavelength sensing. Graphene-based detectors have been demonstrated.[232,253] Black phosphorus with an electrostatically tunable energy band allows detection wavelengths ranging from 2 to 10 μm.[254] Other materials, such as WS_2, have been shown for room temperature detection.[252] It is noteworthy that plasmonic metamaterial absorbers (PMAs) hold promise in IR light detection. Configurations like metal–dielectric–metal (MIM) structures are conducive for SEIRA, facilitating enhanced surface signals and simultaneous signal readout. Achieving resonance absorption by aligning resonance wavelengths with the absorption peaks of multiple gases presents potential applications in VOC sensing.[233] Importantly, these designs are amenable to miniaturization and integration with sensing units and MEMS thermal emitters while maintaining cost-effectiveness.

C. Spectrometer

The spectrometer is a key device in BAS, serving as a crucial substitute for TDLAS to quantitatively analyze VOCs. While FTIR is a widely used spectrometer for organic compound analysis, commercial spectrometers predominantly rely on spatial light. To achieve an on-chip broadband VOC sensor system, four basic types of spectrometers, namely, dispersion, Fourier transform, filters, and computational reconstruction,[255] are considered, as illustrated in Fig. 22. Research on pure dispersion structures, such as on-chip dispersive grating and AWG, has been reported.[256,257] However, the finite chip space constrains the optical path, leading to reduced resolution. This challenge becomes more pronounced for longer wavelengths in the MIR due to the scaling-up footprint. The on-chip Fourier transform spectrometer encounters similar hurdles, with the added issue of substantial modulation power consumption, resulting in increased propagation losses from longer propagation lengths and a reduction in SNR.

In photonics, alternative strategies involve narrowband filters and computational reconstruction. On-chip resonators, e.g., microring, leveraging resonance structures to create a lengthy optical path with a manageable footprint, are commonly employed for constructing On-chip narrowband filters. The approach draws an analogy to CEAS, where cavities within a spectrometer amplify the optical path, leading to a higher Q-factor and improved spectral resolution. Several accomplishments have been documented in the domain of resonance filters.[258,259] Additionally, computational reconstruction represents a relatively recent approach, resembling a tailored wavelength response.[254,260–262] Many studies have grounded their designs in the intrinsic features of the device, while others have used inverse design strategies. By ensuring channel responses align with a set of orthogonal bases or exhibit low cross correlation, these designs can yield a broadband and relatively high-resolution spectrometer with a compact footprint and low modulation power consumption, contrasting with traditional dispersive and Fourier spectrometers.[263] When combined with a broadband source, this approach facilitates the realization of a miniaturized VOCs analysis system capable of multi-composition analysis.

It is worth noting that a dual-comb spectrometer (DCS) can function as both a source and a spectrometer.[264] The two combs, with a small repetition frequency difference, encode spectral information after interacting with VOC analytes. This information can be mapped into the radio frequency (RF) region through temporal beating. However, DCS may require a relatively longer measurement time compared to one-shot measurement arrays, particularly for coherent averages in large noisy scenes.

D. Perspective

IR absorption spectroscopy is one of the most powerful tools for component analysis. In the ongoing maturation of sensor technology, there is a discernible shift toward miniaturization and portability in the development of VOC IR spectroscopic sensors. In this paper, we systematically review IR correlative absorption methods, with a focus on miniaturized interactive devices for VOC sensing. Given the volatility of VOC, investigations can target both the liquid and vapor phases. NIR absorption emerges as a cost-effective solution, utilizing advanced CMOS processes or fiber fabrication techniques. The MIR region, with its fundamental bands, offers stronger vibrations compared to the overtones in the NIR, establishing itself as a key region for VOC spectroscopic sensing technology, especially for gas-phase VOC measurement. Nevertheless, the presence of material absorption like SiO_2 poses limitations on longer wavelength sensing applications, prompting a quest for new material platforms. Different material platforms for MIR VOC sensor require distinct fabrication processes, urging advanced techniques to reduce loss, enhance LOD, and enable features like multiplexing. The coupling strategy on diverse material platforms requires redesign and optimization, emphasizing the need for low-loss, broadband, and functional passive sensing devices.

Moreover, combined with other sensing enhancement technologies like microfluidics, micro-gas chromatography (μ-GC), and functional thin-film materials can be beneficial for molecule capture and LOD improvement. Ensuring the robustness of VOC sensors will increase the veracity of sensing results and lifetime. For example, in the previous description, CEAS is widely used to increase sensitivity and decrease the footprint of sensors. However, due to the high TO coefficient of Si, the cavities can be influenced by temperature easily. Apart from this, active components like phase shifters may produce heat perturbation. Factors such as humidity, pressure, and causticity should also be considered for developing stable VOC sensors, necessitating compensation designs or calibration algorithms to guarantee measurement reliability.

In addition to sensing units, devices required for highly integrated miniaturized sensing systems, such as sources, detectors, and spectrometers, are introduced in this paper. These peripheral devices provide multi-component VOC analysis ability. A chip-integrated laser with high luminous efficiency and stability contributes to robust and efficient analysis results. On-chip LED, supercontinuum, and frequency comb sources are powerful tools with a large detection range, contributing to high selectivity. Advances in low-loss materials and advanced manufacturing processes showcase the potential of on-chip optical frequency comb sensing systems for miniaturized VOC sensing applications. However, achieving low-cost and long-life monolithic integration remains to be studied. In addition, a dynamic spectrometer with high resolution is essential to match the requirements of the broadband source. Combining dispersion and resonance may yield interesting results. By leveraging AI algorithms for functions such as improving SNR, reconstructing high-resolution spectra, and precise gas recognition, high-performance VOC sensors can be achieved with lower hardware requirements. In essence, various efforts across multiple aspects need to converge to achieve a miniaturized and fully integrated VOC detection system.

ACKNOWLEDGMENTS

The research was sponsored by the Natural Science Foundation of Shanghai (21ZR1443100) and the National Natural Science Foundation of China (NSFC) (61705099). B.W. acknowledges the partial supports from the U.S. National Science Foundation CAREER Award No. 2340060, Oklahoma Center for the Advancement of Science and Technology's Research Grant No. AR21-052, and the University of Oklahoma Big Idea Challenge Program. The authors thank the ShanghaiTech University Quantum Device Lab (SQDL) and Max-Optics Corporation for technique support.

AUTHOR DECLARATIONS

Conflict of Interest

The authors have no conflicts to disclose.

Author Contributions

Lipeng Xia and Yuheng Liu contributed equally to this work.

Lipeng Xia: Conceptualization (equal); Data curation (equal); Investigation (equal); Validation (equal); Writing – original draft (equal). **Yuheng Liu:** Conceptualization (equal); Data curation (equal); Investigation (equal); Validation (equal); Writing – original draft (equal). **Ray T. Chen:** Conceptualization (supporting); Supervision (supporting); Writing – review & editing (supporting). **Binbin Weng:** Conceptualization (equal); Funding acquisition (lead); Investigation (equal); Project administration (equal); Resources (equal); Supervision (equal); Writing – review & editing (equal). **Yi Zou:** Conceptualization (lead); Funding acquisition (lead); Investigation (equal); Project administration (equal); Resources (lead); Supervision (equal); Writing – review & editing (equal).

DATA AVAILABILITY

The data that support the findings of this study are available within the article.

REFERENCES

[1] See https://www.epa.gov/indoor-air-quality-iaq/technical-overview-volatile-organic-compounds for "Technical Overview of Volatile Organic Compounds."

[2] See https://www.eea.europa.eu/help/glossary/other-eea-terms/volatile-organic-compound for "Volatile Organic Compound."

[3] J. Kesselmeier and M. Staudt, "Biogenic volatile organic compounds (VOC): An overview on emission, physiology and ecology," J. Atmos. Chem. **33**, 23–88 (1999).

[4] N. Dudareva, A. Klempien, J. K. Muhlemann, and I. Kaplan, "Biosynthesis, function and metabolic engineering of plant volatile organic compounds," New Phytol. **198**(1), 16–32 (2013).

[5] V. Ninkovic, D. Markovic, and M. Rensing, "Plant volatiles as cues and signals in plant communication," Plant Cell Environ. **44**(4), 1030–1043 (2021).

[6] W. A. Dement, B. J. Tyson, and H. A. Mooney, "Mechanism of monoterpene volatilization in *Salvia mellifera*," Phytochemistry **14**(12), 2555–2557 (1975).

[7] J. K. Holopainen and J. Gershenzon, "Multiple stress factors and the emission of plant VOCs," Trends Plant Sci. **15**(3), 176–184 (2010).

[8] A. Manolls, "The diagnostic potential of breath analysis," Clin. Chem. **29**(1), 5 (1983).

[9] S. Chen, L. Zieve, and V. Mahadevan, "Mercaptans and dimethyl sulfide in the breath of patients with cirrhosis of the liver: Effect of feeding methionine," J. Lab. Clin. Med. **75**(4), 628–635 (1970), see https://www.translationalres.com/article/0022-2143(70)90161-7/abstract.

[10] B. Wzorek, P. Mochalski, I. Śliwka, and A. Amann, "Application of GC-MS with a SPME and thermal desorption technique for determination of dimethylamine and trimethylamine in gaseous samples for medical diagnostic purposes," J. Breath Res. **4**(2), 026002 (2010).

[11] M. Phillips, K. Gleeson, J. M. B. Hughes, J. Greenberg, R. N. Cataneo, L. Baker, and W. P. McVay, "Volatile organic compounds in breath as markers of lung cancer: A cross-sectional study," Lancet **353**(9168), 1930–1933 (1999).

[12] M. Shirasu and K. Touhara, "The scent of disease: Volatile organic compounds of the human body related to disease and disorder," J. Biochem. **150**(3), 257–266 (2011).

[13] P. Kuśtrowski, A. Rokicińska, and T. Kondratowicz, in *Advances in Inorganic Chemistry* (Academic Press, 2018), pp. 385–419.

[14] N. T. Kim Oanh, A. Tipayarom, T. L. Bich, D. Tipayarom, C. D. Simpson, D. Hardie, and L.-J. Sally Liu, "Characterization of gaseous and semi-volatile organic compounds emitted from field burning of rice straw," Atmos. Environ. **119**, 182–191 (2015).

[15] V. Fetisov, A. M. Gonopolsky, H. Davardoost, A. R. Ghanbari, and A. H. Mohammadi, "Regulation and impact of VOC and CO_2 emissions on low-carbon energy systems resilient to climate change: A case study on an environmental issue in the oil and gas industry," Energy Sci. Eng. **11**(4), 1516–1535 (2023).

[16] B.-R. Kim, "VOC emissions from automotive painting and their control: A review," Environ. Eng. Res. **16**(1), 1–9 (2011).

[17] A. L. Clobes, G. P. Ananth, A. L. Hood, J. A. Schroeder, and K. A. Lee, "Human activities as sources of volatile organic compounds in residential environments," Ann. N. Y. Acad. Sci. **641**(1), 79–86 (1992).

[18] M. Mahilang, M. K. Deb, and S. Pervez, "Biogenic secondary organic aerosols: A review on formation mechanism, analytical challenges and environmental impacts," Chemosphere **262**, 127771 (2021).

[19] L. Mølhave, G. Clausen, B. Berglund, J. De Ceaurriz, A. Kettrup, T. Lindvall, M. Maroni, A. C. Pickering, U. Risse, H. Rothweiler, B. Seifert, and M. Younes, "Total volatile organic compounds (TVOC) in indoor air quality investigations," Indoor Air **7**(4), 225–240 (1997).

[20] T. Salthammer, "TVOC - Revisited," Environ. Int. **167**, 107440 (2022).

[21] See https://www.eea.europa.eu/data-and-maps/figures/variations-1990-2020-2000-2020 for "Variations (1990–2020, 2000–2020 for PM10/PM2.5) in the Emissions of Pollutants From Transport by Mode in EU-27."

[22] See https://www.cdc.gov/niosh/docs/92-100/default.html for "NIOSH Recommendations for Occupational Safety and Health. Compendium of Policy Documents and Statements."

[23] See https://public.wmo.int/en/resources/bulletin/changing-volatile-organic-compound-emissions-urban-environments-many-paths for "Changing Volatile Organic Compound Emissions in Urban Environments: Many Paths to Cleaner Air."

[24] A. H. Jalal, F. Alam, S. Roychoudhury, Y. Umasankar, N. Pala, and S. Bhansali, "Prospects and challenges of volatile organic compound sensors in human healthcare," ACS Sens. **3**(7), 1246–1263 (2018).

[25] M. Khatib and H. Haick, "Sensors for volatile organic compounds," ACS Nano **16**(5), 7080–7115 (2022).

[26] See https://www.mordorintelligence.com/industry-reports/volatile-organic-compound-gas-sensor-market for "Global Volatile Organic Compound Gas Sensor Market (2021–2026), Mordor Intelligence."

[27] See https://resources.perkinelmer.com/lab-solutions/resources/docs/AASensitivityvsDetectionLimitTechNote.pdf for "Sensitivity Versus Detection Limit."

[28] K. Tang, M. Qin, W. Fang, J. Duan, F. Meng, K. Ye, H. Zhang, P. Xie, Y. He, W. Xu, J. Liu, and W. Liu, *Simultaneous Detection of Atmospheric HONO and NO2 Utilizing an IBBCEAS System Based on an Iterative Algorithm* (Gases/In Situ Measurement/Instruments and Platforms, 2020).

[29] S. Khan, S. Le Calvé, and D. Newport, "A review of optical interferometry techniques for VOC detection," Sens. Actuators, A **302**, 111782 (2020).

[30] Z. Chen, J. Zeng, M. He, X. Zhu, and Y. Shi, "Portable ppb-level carbon dioxide sensor based on flexible hollow waveguide cell and mid-infrared spectroscopy," Sens. Actuators, B **359**, 131553 (2022).

[31] R. St-Gelais, G. Mackey, J. Saunders, J. Zhou, A. Leblanc-Hotte, A. Poulin, J. A. Barnes, H.-P. Loock, R. S. Brown, and Y.-A. Peter, "Gas sensing using polymer-functionalized deformable Fabry–Perot interferometers," Sens. Actuators, B **182**, 45–52 (2013).

[32] A. K. Pathak and C. Viphavakit, "A review on all-optical fiber-based VOC sensors: Heading towards the development of promising technology," Sens. Actuators, A **338**, 113455 (2022).

[33] R. Howley, B. D. MacCraith, K. O'Dwyer, H. Masterson, P. Kirwan, and P. McLoughlin, "Determination of hydrocarbons using sapphire fibers coated with poly(dimethylsiloxane)," Appl. Spectrosc. **57**(4), 400–406 (2003).

[34] C.-B. Yu, Y. Wu, C. Li, F. Wu, J.-H. Zhou, Y. Gong, Y.-J. Rao, and Y.-F. Chen, "Highly sensitive and selective fiber-optic Fabry-Perot volatile organic compounds sensor based on a PMMA film," Opt. Mater. Express **7**(6), 2111 (2017).

[35] J. Nuñez, A. Boersma, J. Grand, S. Mintova, and B. Sciacca, "Thin functional zeolite layer supported on infrared resonant nano-antennas for the detection of benzene traces," Adv. Funct. Mater. **31**(24), 2101623 (2021).

[36] R. Krska, K. Taga, and R. Kellner, "New IR fiber-optic chemical sensor for *in situ* measurements of chlorinated hydrocarbons in water," Appl. Spectrosc. **47**(9), 1484–1487 (1993).

[37] J. Su, S. Dai, and N. Gan, "Optimized Ge-As-Se-Te chalcogenide glass fiber sensor with polydopamine-coated tapered zone for the highly sensitive detection of p-xylene in waters," Opt. Express **28**(1), 184 (2020).

[38] T. Liu, J. Han, and H. Hu, "Optical current sensor with dual-wavelength configuration for improving temperature robustness," IEEE Photonics J. **9**(1), 6800210 (2017).

[39] L. Fernandez, A. Gutierrez-Galvez, and S. Marco, "Robustness to sensor damage of a highly redundant gas sensor array," Procedia Eng. **87**, 851–854 (2014).

[40] J. Fonollosa, A. Vergara, and R. Huerta, "Algorithmic mitigation of sensor failure: Is sensor replacement really necessary?," Sens. Actuators, B **183**, 211–221 (2013).

[41] J. Wu, G. Yue, W. Chen, Z. Xing, J. Wang, W. R. Wong, Z. Cheng, S. Y. Set, G. Senthil Murugan, X. Wang, and T. Liu, "On-chip optical gas sensors based on group-IV materials," ACS Photonics **7**(11), 2923–2940 (2020).

[42] H. Lin, Z. Luo, T. Gu, L. C. Kimerling, K. Wada, A. Agarwal, and J. Hu, "Mid-infrared integrated photonics on silicon: A perspective," Nanophotonics **7**(2), 393–420 (2017).

[43] Y. Zou, S. Chakravarty, C.-J. Chung, X. Xu, and R. T. Chen, "Mid-infrared silicon photonic waveguides and devices [Invited]," Photonics Res. **6**(4), 254 (2018).

[44] A. Schliesser, N. Picqué, and T. W. Hänsch, "Mid-infrared frequency combs," Nat. Photonics **6**(7), 440–449 (2012).

[45] A. Li, C. Yao, J. Xia, H. Wang, Q. Cheng, R. Penty, Y. Fainman, and S. Pan, "Advances in cost-effective integrated spectrometers," Light **11**(1), 174 (2022).

[46] Y. Ma, B. Dong, and C. Lee, "Progress of infrared guided-wave nanophotonic sensors and devices," Nano Convergence **7**(1), 12 (2020).

[47] A. B. Dahlin, "Size matters: Problems and advantages associated with highly miniaturized sensors," Sensors **12**(3), 3018–3036 (2012).

[48] V. Singh, P. T. Lin, N. Patel, H. Lin, L. Li, Y. Zou, F. Deng, C. Ni, J. Hu, J. Giammarco, A. P. Soliani, B. Zdyrko, I. Luzinov, S. Novak, J. Novak, P. Wachtel, S. Danto, J. D. Musgraves, K. Richardson, L. C. Kimerling, and A. M. Agarwal, "Mid-infrared materials and devices on a Si platform for optical sensing," Sci. Technol. Adv. Mater. **15**(1), 014603 (2014).

[49] Y. Ozaki, "Infrared spectroscopy—Mid-infrared, near-infrared, and far-infrared/terahertz spectroscopy," Anal. Sci. **37**(9), 1193–1212 (2021).

[50] S. Türker-Kaya and C. W. Huck, "A review of mid-infrared and near-infrared imaging: Principles, concepts and applications in plant tissue analysis," Molecules **22**(1), 168 (2017).

[51] R. Soref, "Mid-infrared photonics in silicon and germanium," Nat. Photonics **4**(8), 495–497 (2010).

[52] M. Nedeljkovic, A. Z. Khokhar, Y. Hu, X. Chen, J. S. Penades, S. Stankovic, H. M. H. Chong, D. J. Thomson, F. Y. Gardes, G. T. Reed, and G. Z. Mashanovich, "Silicon photonic devices and platforms for the mid-infrared," Opt. Mater. Express **3**(9), 1205 (2013).

[53] Z. Han, P. Lin, V. Singh, L. Kimerling, J. Hu, K. Richardson, A. Agarwal, and D. T. H. Tan, "On-chip mid-infrared gas detection using chalcogenide glass waveguide," Appl. Phys. Lett. **108**(14), 141106 (2016).

[54] M. Montesinos-Ballester, C. Lafforgue, J. Frigerio, A. Ballabio, V. Vakarin, Q. Liu, J. M. Ramirez, X. L. Roux, D. Bouville, A. Barzaghi, C. Alonso-Ramos, L. Vivien, G. Isella, and D. Marris-Morini, "On-chip mid-infrared supercontinuum generation from 3 to 13 μm wavelength," ACS Photonics **7**(12), 3423–3429 (2020).

[55] See https://cdxapps.epa.gov/oms-substance-registry-services/substance-details/761346 for information about related VOC substances from the list (EPA ID: E761346).

[56] See https://webbook.nist.gov/chemistry/cas-ser/ for information about IR spectra of substances.

[57] G. Li, Y. Wu, Z. Zhang, X. Zhang, K. Ma, Y. Jiao, J. Li, Y. Liu, Y. Song, H. Zhao, S. Zhai, and Q. Li, "WMS based dual-range real-time trace sensor for ethane detection in exhaled breath," Opt. Lasers Eng. **159**, 107222 (2022).

[58] P. Kluczynski, J. Gustafsson, Å. M. Lindberg, and O. Axner, "Wavelength modulation absorption spectrometry—An extensive scrutiny of the generation of signals," Spectrochim. Acta, Part B **56**(8), 1277–1354 (2001).

[59] T. Berg, H. Voges, O. Thiele, V. Beushausen, W. Hentschel, and F. Kallmeyer, *IEEE Sensors* (IEEE, Irvine, CA, 2005), pp. 983–986.

[60] M. D. Ruesch, G. C. Mathews, R. J. Tancin, S. F. Son, and C. S. Goldenstein, "Wavelength-modulation spectroscopy in the mid-infrared for temperature and HCl measurements in aluminum-lithium composite-propellant flames," Combust. Flame **242**, 112180 (2022).

[61] M. Raza, L. Ma, C. Yao, M. Yang, Z. Wang, Q. Wang, R. Kan, and W. Ren, "MHz-rate scanned-wavelength direct absorption spectroscopy using a distributed feedback diode laser at 2.3 μm," Opt. Laser Technol. **130**, 106344 (2020).

[62] C. S. Goldenstein, R. M. Spearrin, J. Jeffries, and R. K. Hanson, "Infrared laser-absorption sensing for combustion gases," Prog. Energy Combust. Sci. **60**, 132–176 (2017).

[63] H. Teichert, T. Fernholz, and V. Ebert, "Simultaneous *in situ* measurement of CO, H_2O, and gas temperatures in a full-sized coal-fired power plant by near-infrared diode lasers," Appl. Opt. **42**(12), 2043 (2003).

[64] H. Ma, M. Sun, S. Zhan, Q. Zhang, S. Zha, G. Wang, K. Liu, M. Yi, and Z. Cao, "Compact dual-gas sensor for simultaneous measurement of atmospheric methane, and water vapor using a 3.38 μm antimonide-distributed feedback laser diode," Spectrochim. Acta, Part A **226**, 117605 (2020).

[65] S. Feng, X. Qiu, G. Guo, E. Zhang, Q. He, X. He, W. Ma, C. Fittschen, and C. Li, "Palm-sized laser spectrometer with high robustness and sensitivity for trace gas detection using a novel double-layer toroidal cell," Anal. Chem. **93**(10), 4552–4558 (2021).

[66] M. Pi, Y. Huang, H. Zhao, Z. Peng, J. Lang, J. Ji, L. Teng, F. Song, L. Liang, Y. Zhang, C. Zheng, Y. Wang, and F. K. Tittel, "Theoretical and experimental investigation of on-chip mid-infrared chalcogenide waveguide CH_4 sensor based on wavelength modulation spectroscopy," Sens. Actuators, B **362**, 131782 (2022).

[67] G. B. Rieker, J. B. Jeffries, and R. K. Hanson, "Calibration-free wavelength-modulation spectroscopy for measurements of gas temperature and concentration in harsh environments," Appl. Opt. **48**(29), 5546 (2009).

[68] C. S. Goldenstein, C. L. Strand, I. A. Schultz, K. Sun, J. B. Jeffries, and R. K. Hanson, "Fitting of calibration-free scanned-wavelength-modulation spectroscopy spectra for determination of gas properties and absorption lineshapes," Appl. Opt. **53**(3), 356 (2014).

[69] A. Upadhyay, D. Wilson, M. Lengden, A. L. Chakraborty, G. Stewart, and W. Johnstone, "Calibration-free WMS using a cw-DFB-QCL, a VCSEL, and an edge-emitting DFB laser with in-situ real-time laser parameter characterization," IEEE Photonics J. **9**(2), 6801217 (2017).

[70] C. S. Goldenstein, C. A. Almodóvar, J. B. Jeffries, R. K. Hanson, and C. M. Brophy, "High-bandwidth scanned-wavelength-modulation spectroscopy sensors for temperature and H_2O in a rotating detonation engine," Meas. Sci. Technol. **25**(10), 105104 (2014).

[71] D. T. Cassidy and J. Reid, "Atmospheric pressure monitoring of trace gases using tunable diode lasers," Appl. Opt. **21**(7), 1185–1190 (1982).

[72] A. Klein, O. Witzel, and V. Ebert, "Rapid, time-division multiplexed, direct absorption- and wavelength modulation-spectroscopy," Sensors **14**(11), 21497–21513 (2014).

[73] Y. Du, Z. Peng, and Y. Ding, "Wavelength modulation spectroscopy for recovering absolute absorbance," Opt. Express **26**(7), 9263 (2018).

[74] S. H. Schlindwein, *About Spectral Resolution in FT-IR Spectroscopy* (Bruker Optics Blog, 2020).

[75] A. Karabchevsky, A. Katiyi, A. S. Ang, and A. Hazan, "On-chip nanophotonics and future challenges," Nanophotonics **9**(12), 3733–3753 (2020).

[76] H. B. Qazi, A. B. bin Mohammad, and M. Akram, "Recent progress in optical chemical sensors," Sensors **12**(12), 16522–16556 (2012).

[77] A. D. Kersey and A. Dandridge, in *Proceedings of the 39th Electronic Components Conference* (IEEE, Houston, TX, 1989), pp. 472–478.

[78] B. Culshaw, "Fiber optics in sensing and measurement," IEEE J. Sel. Top. Quantum Electron. **6**(6), 1014–1021 (2000).

[79] P. Lu, N. Lalam, M. Badar, B. Liu, B. T. Chorpening, M. P. Buric, and P. R. Ohodnicki, "Distributed optical fiber sensing: Review and perspective," Appl. Phys. Rev. **6**(4), 041302 (2019).

[80] R. Lu, B. Mizaikoff, W.-W. Li, C. Qian, A. Katzir, Y. Raichlin, G.-P. Sheng, and H.-Q. Yu, "Determination of chlorinated hydrocarbons in water using highly sensitive mid-infrared sensor technology," Sci. Rep. **3**(1), 2525 (2013).

[81] L. Jiao, N. Zhong, X. Zhao, S. Ma, X. Fu, and D. Dong, "Recent advances in fiber-optic evanescent wave sensors for monitoring organic and inorganic pollutants in water," TrAC. Trends Anal. Chem. **127**, 115892 (2020).

[82] S. Maurugeon, B. Bureau, C. Boussard-Plédel, A. J. Faber, P. Lucas, X. H. Zhang, and J. Lucas, "Selenium modified $GeTe_4$ based glasses optical fibers for far-infrared sensing," Opt. Mater. **33**(4), 660–663 (2011).

[83] B. Bureau, S. Maurugeon, F. Charpentier, J.-L. Adam, C. Boussard-Plédel, and X.-H. Zhang, "Chalcogenide glass fibers for infrared sensing and space optics," Fiber Integr. Opt. **28**(1), 65–80 (2009).

[84] S. Cui, C. Boussard-Plédel, J. Lucas, and B. Bureau, "Te-based glass fiber for far-infrared biochemical sensing up to 16 μm," Opt. Express **22**(18), 21253 (2014).

[85] B. Mizaikoff, "Peer reviewed: Mid-IR fiber-optic sensors," Anal. Chem. **75**(11), 258 A–267 A (2003).

[86] A. K. Sharma, J. Gupta, and I. Sharma, "Fiber optic evanescent wave absorption-based sensors: A detailed review of advancements in the last decade (2007–18)," Optik **183**, 1008–1025 (2019).

[87] D. A. C. Compton, S. L. Hill, N. A. Wright, M. A. Druy, J. Piche, W. A. Stevenson, and D. W. Vidrine, "*In situ* FT-IR analysis of a composite curing reaction using a mid-infrared transmitting optical fiber," Appl. Spectrosc. **42**(6), 972–979 (1988).

[88] R. Lu, W.-W. Li, B. Mizaikoff, A. Katzir, Y. Raichlin, G.-P. Sheng, and H.-Q. Yu, "High-sensitivity infrared attenuated total reflectance sensors for *in situ* multicomponent detection of volatile organic compounds in water," Nat. Protoc. **11**(2), 377–386 (2016).

[89] K. Flavin, H. Hughes, V. Dobbyn, P. Kirwan, K. Murphy, H. Steiner, B. Mizaikoff, and P. Mcloughlin, "A comparison of polymeric materials as pre-concentrating media for use with ATR/FTIR sensing," Int. J. Environ. Anal. Chem. **86**(6), 401–415 (2006).

[90] R. Howley, B. D. MacCraith, K. O'Dwyer, P. Kirwan, and P. McLoughlin, "A study of the factors affecting the diffusion of chlorinated hydrocarbons into polyisobutylene and polyethylene-co-propylene for evanescent wave sensing," Vib. Spectrosc. **31**(2), 271–278 (2003).

[91] B. Murphy and P. Mcloughlin, "Determination of chlorinated hydrocarbon species in aqueous solution using Teflon coated ATR waveguide/FTIR spectroscopy," Int. J. Environ. Anal. Chem. **83**(7–8), 653–662 (2003).

[92] R. Göbel, R. W. Seitz, S. A. Tomellini, R. Krska, and R. Kellner, "Infrared attenuated total reflection spectroscopic investigations of the diffusion behaviour of chlorinated hydrocarbons into polymer membranes," Vib. Spectrosc. **8**(2), 141–149 (1995).

[93] R. Göbel, R. Krska, R. Kellner, R. W. Seitz, and S. A. Tomellini, "Investigation of different polymers as coating materials for IR/ATR spectroscopic trace analysis of chlorinated hydrocarbons in water," Appl. Spectrosc. **48**(6), 678–683 (1994).

[94] R. Göbel, R. Krska, S. Neal, and R. Kellner, "Performance studies of an IR fiber optic sensor for chlorinated hydrocarbons in water," Fresenius' J. Anal. Chem. **350**(7–9), 514–519 (1994).

[95] M. Jakusch, B. Mizaikoff, R. Kellner, and A. Katzir, "Towards a remote IR fiber-optic sensor system for the determination of chlorinated hydrocarbons in water," Sens. Actuators, B **38**(1–3), 83–87 (1997).

[96] B. Mizaikoff, "Mid-infrared fiber optic sensors: Potential and perspectives," Proc. SPIE **3849**, 7–18 (1999).

[97] S. F. Memon, E. Lewis, M. M. Ali, J. T. Pembroke, and B. S. Chowdhry, in *IEEE Sensors Applications Symposium (SAS)* (IEEE, Glassboro, NJ, 2017).

[98] P. Houizot, M.-L. Anne, C. Boussard-Plédel, O. Loréal, H. Tariel, J. Lucas, and B. Bureau, "Shaping of looped miniaturized chalcogenide fiber sensing heads for mid-infrared sensing," Sensors **14**(10), 17905–17914 (2014).

[99] C. Dettenrieder, Y. Raichlin, A. Katzir, and B. Mizaikoff, "Toward the required detection limits for volatile organic constituents in marine environments with infrared evanescent field chemical sensors," Sensors **19**(17), 3644 (2019).

[100] R. Lu, G. Sheng, W. Li, H. Yu, Y. Raichlin, A. Katzir, and B. Mizaikoff, "IR-ATR chemical sensors based on planar silver halide waveguides coated with an ethylene/propylene copolymer for detection of multiple organic contaminants in water," Angew. Chem., Int. Ed. **52**(8), 2265–2268 (2013).

[101] E. M. Kosower, G. Markovich, Y. Raichlin, G. Borz, and A. Katzir, "Surface-enhanced infrared absorption and amplified spectra on planar silver halide fiber," J. Phys. Chem. B **108**(34), 12633–12636 (2004).

[102] K. Goya, Y. Koyama, Y. Nishijima, S. Tokita, R. Yasuhara, and H. Uehara, "A fluoride fiber optics in-line sensor for mid-IR spectroscopy based on a side-polished structure," Sens. Actuators, B **351**, 130904 (2022).

[103] Y. Yang, K. Ge, P. Tao, S. Dai, X. Wang, W. Zhang, T. Xu, Y. Wang, T.-J. Lin, and P. Zhang, "Mid-infrared evanescent wave sensor based on side-polished chalcogenide fiber," Ceram. Int. **49**(1), 1291–1297 (2023).

[104] E. Korsakova, A. Yuzhakova, D. Salimgareev, A. Lvov, L. Zhukova, and A. Korsakov, "Mid-infrared silver halide fibre-optic sensor with lateral notches for evanescent wave spectroscopy," Infrared Phys. Technol. **128**, 104529 (2023).

[105] P. B. Tarsa, P. Rabinowitz, and K. K. Lehmann, "Evanescent field absorption in a passive optical fiber resonator using continuous-wave cavity ring-down spectroscopy," Chem. Phys. Lett. **383**(3–4), 297–303 (2004).

[106] S. Pu and X. Gu, "Fiber loop ring-down spectroscopy with a long-period grating cavity," Opt. Lett. **34**(12), 1774 (2009).

[107] M. Hu, M. Hu, W. Wang, and Q. Wang, "Wavelength-scanned all-fiber cavity ring-down gas sensing using an L-band active fiber loop," Appl. Phys. B **128**(2), 30 (2022).

[108] S. Cui, R. Chahal, C. Boussard-Plédel, V. Nazabal, J.-L. Doualan, J. Troles, J. Lucas, and B. Bureau, "From selenium- to tellurium-based glass optical fibers for infrared spectroscopies," Molecules **18**(5), 5373–5388 (2013).

[109] Z. Hui, Y. Zhang, and A.-H. Soliman, "Mid-infrared dual-rhombic air hole Ge$_{20}$Sb$_{15}$Se$_{65}$ chalcogenide photonic crystal fiber with high birefringence and high nonlinearity," Ceram. Int. **44**(9), 10383–10392 (2018).

[110] L. Brilland, J. Troles, P. Houizot, F. Désévédavy, Q. Coulombier, G. Renversez, T. Chartier, T. N. Nguyen, J.-L. Adam, and N. Traynor, "Interfaces impact on the transmission of chalcogenides photonic crystal fibres," J. Ceram. Soc. Jpn. **116**(1358), 1024–1027 (2008).

[111] J. C. Knight, "Photonic crystal fibres," Nature **424**(6950), 847–851 (2003).

[112] P. Russell, "Photonic crystal fibers," Science **299**(5605), 358–362 (2003).

[113] M. De, T. K. Gangopadhyay, and V. K. Singh, "Prospects of photonic crystal fiber as physical sensor: An overview," Sensors **19**(3), 464 (2019).

[114] S. O. Konorov, A. M. Zheltikov, and M. Scalora, "Photonic-crystal fiber as a multifunctional optical sensor and sample collector," Opt. Express **13**(9), 3454 (2005).

[115] S. Hossain, S. Shah, and M. Faisal, "Ultra-high birefringent, highly nonlinear Ge$_{20}$Sb$_{15}$Se$_{65}$ chalcogenide glass photonic crystal fiber with zero dispersion wavelength for mid-infrared applications," Optik **225**, 165753 (2021).

[116] J. D. Shephard, W. N. MacPherson, R. R. J. Maier, J. D. C. Jones, D. P. Hand, M. Mohebbi, A. K. George, P. J. Roberts, and J. C. Knight, "Single-mode mid-IR guidance in a hollow-core photonic crystal fiber," Opt. Express **13**(18), 7139 (2005).

[117] Ł. W. Kornaszewski, N. Gayraud, J. M. Stone, W. N. MacPherson, A. K. George, J. C. Knight, D. P. Hand, and D. T. Reid, "Mid-infrared methane detection in a photonic bandgap fiber using a broadband optical parametric oscillator," Opt. Express **15**(18), 11219 (2007).

[118] R. Dhawan, M. Khan, N. Panwar, U. Tiwari, R. Bhatnagar, and S. C. Jain, "A low loss mechanical splice for gas sensing using Hollow-Core Photonic Crystal Fibre," Optik **124**(18), 3671–3673 (2013).

[119] N. Gayraud, Ł. W. Kornaszewski, J. M. Stone, J. C. Knight, D. T. Reid, D. P. Hand, and W. N. MacPherson, "Mid-infrared gas sensing using a photonic bandgap fiber," Appl. Opt. **47**(9), 1269 (2008).

[120] P. Jaworski, K. Krzempek, G. Dudzik, P. J. Sazio, and W. Belardi, "Nitrous oxide detection at 5.26 μm with a compound glass antiresonant hollow-core optical fiber," Opt. Lett. **45**(6), 1326 (2020).

[121] F. Yang, W. Jin, Y. Cao, H. L. Ho, and Y. Wang, "Towards high sensitivity gas detection with hollow-core photonic bandgap fibers," Opt. Express **22**(20), 24894 (2014).

[122] J. P. Parry, B. C. Griffiths, N. Gayraud, E. D. McNaghten, A. M. Parkes, W. N. MacPherson, and D. P. Hand, "Towards practical gas sensing with micro-structured fibres," Meas. Sci. Technol. **20**(7), 075301 (2009).

[123] W. Jin, H. L. Ho, Y. C. Cao, J. Ju, and L. F. Qi, "Gas detection with micro- and nano-engineered optical fibers," Opt. Fiber Technol. **19**(6), 741–759 (2013).

[124] F. Benabid, J. C. Knight, G. Antonopoulos, and P. St. J. Russell, "Stimulated Raman scattering in hydrogen-filled hollow-core photonic crystal fiber," Science **298**(5592), 399–402 (2002).

[125] K. Krzempek, K. Abramski, and M. Nikodem, "Kagome hollow core fiber-based mid-infrared dispersion spectroscopy of methane at sub-ppm levels," Sensors **19**(15), 3352 (2019).

[126] M. Nikodem, K. Krzempek, G. Dudzik, and K. Abramski, "Hollow core fiber-assisted absorption spectroscopy of methane at 3.4 μm," Opt. Express **26**(17), 21843 (2018).

[127] A. D. Pryamikov, A. S. Biriukov, A. F. Kosolapov, V. G. Plotnichenko, S. L. Semjonov, and E. M. Dianov, "Demonstration of a waveguide regime for a silica hollow - core microstructured optical fiber with a negative curvature of the core boundary in the spectral region > 35 μm," Opt. Express **19**(2), 1441 (2011).

[128] M. Klimczak, D. Dobrakowski, A. N. Ghosh, G. Stępniewski, D. Pysz, G. Huss, T. Sylvestre, and R. Buczyński, "Nested capillary anti-resonant silica fiber with mid-infrared transmission and low bending sensitivity at 4000 nm," Opt. Lett. **44**(17), 4395 (2019).

[129] M. Nikodem, G. Gomółka, M. Klimczak, D. Pysz, and R. Buczyński, "Demonstration of mid-infrared gas sensing using an anti-resonant hollow core fiber and a quantum cascade laser," Opt. Express **27**(25), 36350 (2019).

[130] G. Gomółka, D. Pysz, R. Buczyński, and M. Nikodem, "Wavelength modulation spectroscopy of oxygen inside anti-resonant hollow-core fiber-based gas cell," Opt. Laser Technol. **170**, 110323 (2024).

[131] G. Gomółka, G. Stępniewski, D. Pysz, R. Buczyński, M. Klimczak, and M. Nikodem, "Highly sensitive methane detection using a mid-infrared interband cascade laser and an anti-resonant hollow-core fiber," Opt. Express **31**(3), 3685 (2023).

[132] Y. Luzinova, B. Zdyrko, I. Luzinov, and B. Mizaikoff, "In situ trace analysis of oil in water with mid-infrared fiberoptic chemical sensors," Anal. Chem. **84**(3), 1274–1280 (2012).

[133] P. Jaworski, P. Kozioł, K. Krzempek, D. Wu, F. Yu, P. Bojęś, G. Dudzik, M. Liao, K. Abramski, and J. Knight, "Antiresonant hollow-core fiber-based dual gas sensor for detection of methane and carbon dioxide in the near- and mid-infrared regions," Sensors **20**(14), 3813 (2020).

[134] M. Hu, A. Ventura, J. Grigoleto Hayashi, F. Poletti, and W. Ren, "Mid-infrared absorption spectroscopy of ethylene at 10.5 μm using a chalcogenide hollow-core antiresonant fiber," Opt. Laser Technol. **158**, 108932 (2023).

[135] D. M. Kita, J. Michon, S. G. Johnson, and J. Hu, "Are slot and sub-wavelength grating waveguides better than strip waveguides for sensing?," Optica **5**(9), 1046 (2018).

[136] J. T. Robinson, K. Preston, O. Painter, and M. Lipson, "First-principle derivation of gain in high-index-contrast waveguides," Opt. Express **16**(21), 16659 (2008).

[137] L. Tombez, E. J. Zhang, J. S. Orcutt, S. Kamlapurkar, and W. M. J. Green, "Methane absorption spectroscopy on a silicon photonic chip," Optica **4**(11), 1322 (2017).

[138] Q. Liu, J. M. Ramirez, V. Vakarin, X. Le Roux, A. Ballabio, J. Frigerio, D. Chrastina, G. Isella, D. Bouville, L. Vivien, C. A. Ramos, and D. Marris-Morini, "Mid-infrared sensing between 5.2 and 6.6 μm wavelengths using Ge-rich SiGe waveguides [Invited]," Opt. Mater. Express **8**(5), 1305 (2018).

[139] X. Wang, J. Antoszewski, G. Putrino, W. Lei, L. Faraone, and B. Mizaikoff, "Mercury–Cadmium–telluride waveguides—A novel strategy for on-chip mid-infrared sensors," Anal. Chem. **85**(22), 10648–10652 (2013).

[140] T. Jin, J. Zhou, H.-Y. G. Lin, and P. T. Lin, "Mid-infrared chalcogenide waveguides for real-time and nondestructive volatile organic compound detection," Anal. Chem. **91**(1), 817–822 (2019).

[141] J. Zhou, D. Al Husseini, J. Li, Z. Lin, S. Sukhishvili, G. L. Coté, R. Gutierrez-Osuna, and P. T. Lin, "Detection of volatile organic compounds using mid-infrared silicon nitride waveguide sensors," Sci. Rep. **12**(1), 5572 (2022).

[142] T. Jin, H.-Y. G. Lin, T. Tiwald, and P. T. Lin, "Flexible mid-infrared photonic circuits for real-time and label-free hydroxyl compound detection," Sci. Rep. **9**(1), 4153 (2019).

[143] R. Bi, M. Pi, C. Zheng, H. Zhao, L. Liang, F. Song, D. Wang, Y. Zhang, Y. Wang, and F. K. Tittel, "A niobium pentoxide waveguide sensor for on-chip mid-infrared absorption spectroscopic methane measurement," Sens. Actuators, B **382**, 133567 (2023).

[144] J. Bürger, V. Schalles, J. Kim, B. Jang, M. Zeisberger, J. Gargiulo, L. d S. Menezes, M. A. Schmidt, and S. A. Maier, "3D-nanoprinted antiresonant hollow-core microgap waveguide: An on-chip platform for integrated photonic devices and sensors," ACS Photonics **9**(9), 3012–3024 (2022).

[145] A. Wilk, J. C. Carter, M. Chrisp, A. M. Manuel, P. Mirkarimi, J. B. Alameda, and B. Mizaikoff, "Substrate-integrated hollow waveguides: A new level of integration in mid-infrared gas sensing," Anal. Chem. **85**(23), 11205–11210 (2013).

[146] S. Zheng, H. Cai, L. Xu, N. Li, Z. Gu, Y. Zhang, W. Chen, Y. Zhou, Q. Zhang, and L. Y. T. Lee, "Silicon substrate-integrated hollow waveguide for miniaturized optical gas sensing," Photonics Res. **10**(1), 261 (2022).

[147] A. Fathy, Y. Sabry, F. Marty, D. Khalil, and T. Bourouina, "Silicon based integrated hollow waveguide for gas sensing applications," Proc. SPIE **11355**, 113550T (2020).

[148] J. Ji, Y. Huang, M. Pi, H. Zhao, Z. Peng, C. Li, Q. Wang, Y. Zhang, Y. Wang, and C. Zheng, "Performance improvement of on-chip mid-infrared waveguide methane sensor using wavelet denoising and Savitzky-Golay filtering," Infrared Phys. Technol. **127**, 104469 (2022).

[149] Y. Zou, H. Subbaraman, S. Chakravarty, X. Xu, A. Hosseini, W.-C. Lai, P. Wray, and R. T. Chen, "Grating-coupled silicon-on-sapphire integrated slot waveguides operating at mid-infrared wavelengths," Opt. Lett. **39**(10), 3070 (2014).

[150] W.-C. Lai, Y. Zou, S. Chakravarty, L. Zhu, and R. T. Chen, "Comparative sensitivity analysis of integrated optical waveguides for near-infrared volatile organic compounds with 1ppb detection," Proc. SPIE **8990**, 89900Z (2014).

[151] P. T. Lin, S. W. Kwok, H.-Y. G. Lin, V. Singh, L. C. Kimerling, G. M. Whitesides, and A. Agarwal, "Mid-infrared spectrometer using opto-nanofluidic slot-waveguide for label-free on-chip chemical sensing," Nano Lett. **14**(1), 231–238 (2014).

[152] A. Zhang, L. Xia, T. Li, C. Chang, P. Zhou, X. Xu, and Y. Zou, "Ultra-compact polarization-independent 3 dB power splitter in silicon," Opt. Lett. **46**(19), 5000–5003 (2021).

[153] W. He, Y. Sun, P. Zhou, L. Xia, T. Li, Q. Yi, L. Shen, Z. Cheng, and Y. Zou, "Subwavelength structure engineered passband filter for the 2-μm wave band," Opt. Lett. **48**(3), 827 (2023).

[154] G. Xu, J. Wang, Q. Ji, M. Yang, T. Huang, J. Pan, Y. Xie, and P. P. Shum, "Design and analysis of slow-light Bloch slot waveguides for on-chip gas sensing," J. Opt. Soc. Am. B **37**(2), 257 (2020).

[155] A. Gervais, P. Jean, W. Shi, and S. LaRochelle, "Design of slow-light subwavelength grating waveguides for enhanced on-chip methane sensing by absorption spectroscopy," IEEE J. Sel. Top. Quantum Electron. **25**(3), 5200308 (2019).

[156] Y. Hu, W. He, Y. Sun, Q. Yi, S. Xing, Z. Yan, L. Xia, T. Li, P. Zhou, J. Zhang, L. Shen, and Y. Zou, "High-efficient subwavelength structure engineered grating couplers for 2-μm waveband high-speed data transmission," Opt. Express **31**(23), 39079–39087 (2023).

[157] J. Zhou, Z. Zhang, B. Dong, Z. Ren, W. Liu, and C. Lee, "Midinfrared spectroscopic analysis of aqueous mixtures using artificial-intelligence-enhanced metamaterial waveguide sensing platform," ACS Nano **17**(1), 711–724 (2023).

[158] Z. Ruan, L. Shen, S. Zheng, and J. Wang, "Subwavelength grating slot (SWGS) waveguide on silicon platform," Opt. Express **25**(15), 18250 (2017).

[159] M. Pi, C. Zheng, R. Bi, H. Zhao, L. Liang, Y. Zhang, Y. Wang, and F. K. Tittel, "Design of a mid-infrared suspended chalcogenide/silica-on-silicon slot-waveguide spectroscopic gas sensor with enhanced light-gas interaction effect," Sens. Actuators, B **297**, 126732 (2019).

[160] F. Ottonello-Briano, C. Errando-Herranz, H. Rödjegård, H. Martin, H. Sohlström, and K. B. Gylfason, "Carbon dioxide absorption spectroscopy with a mid-infrared silicon photonic waveguide," Opt. Lett. **45**(1), 109 (2020).

[161] M. Vlk, A. Datta, S. Alberti, H. D. Yallew, V. Mittal, G. S. Murugan, and J. Jágerská, "Extraordinary evanescent field confinement waveguide sensor for mid-infrared trace gas spectroscopy," Light **10**(1), 26 (2021).

[162] W. Liu, Y. Ma, Y. Chang, B. Dong, J. Wei, Z. Ren, and C. Lee, "Suspended silicon waveguide platform with subwavelength grating metamaterial cladding for long-wave infrared sensing applications," Nanophotonics **10**(7), 1861–1870 (2021).

[163] W. Liu, Y. Ma, X. Liu, J. Zhou, C. Xu, B. Dong, and C. Lee, "Larger-than-unity external optical field confinement enabled by metamaterial-assisted comb waveguide for ultrasensitive long-wave infrared gas spectroscopy," Nano Lett. **22**(15), 6112–6120 (2022).

[164] K. M. Yoo, J. Midkiff, A. Rostamian, C. Chung, H. Dalir, and R. T. Chen, "InGaAs membrane waveguide: A promising platform for monolithic integrated mid-infrared optical gas sensor," ACS Sens. **5**(3), 861–869 (2020).

[165] T. Li, P. Zhou, and Y. Zou, "Suspended subwavelength grating waveguides on SOI for ultra-broadband operation," Proc. SPIE **11285**, 112850P (2020).

[166] F. Nadeem, J. Mandon, S. M. Cristescu, A. Khodabakhsh, and F. J. M. Harren, "Experimental-based comparison between off-axis integrated cavity output spectroscopy and multipass-assisted wavelength modulation spectroscopy at 77 μm," OSA Continuum **2**(9), 2667 (2019).

[167] B. Löhden, S. Kuznetsova, K. Sengstock, V. M. Baev, A. Goldman, S. Cheskis, and B. Pálsdóttir, "Fiber laser intracavity absorption spectroscopy for in situ multicomponent gas analysis in the atmosphere and combustion environments," Appl. Phys. B **102**(2), 331–344 (2011).

[168] K. Wang, L. Shao, J. Chen, G. Wang, K. Liu, T. Tan, J. Mei, W. Chen, and X. Gao, "A dual-laser sensor based on off-axis integrated cavity output spectroscopy and time-division multiplexing method," Sensors **20**(21), 6192 (2020).

[169] J. Wang, X. Tian, Y. Dong, G. Zhu, J. Chen, T. Tan, K. Liu, W. Chen, and X. Gao, "Enhancing off-axis integrated cavity output spectroscopy (OA-ICOS) with radio frequency white noise for gas sensing," Opt. Express **27**(21), 30517 (2019).

[170] Y. A. Bakhirkin, A. A. Kosterev, C. Roller, R. F. Curl, and F. K. Tittel, "Mid-infrared quantum cascade laser based off-axis integrated cavity output spectroscopy for biogenic nitric oxide detection," Appl. Opt. **43**(11), 2257 (2004).

[171] Q. He, C. Zheng, K. Zheng, and F. K. Tittel, "Off-axis integrated cavity output spectroscopy for real-time methane measurements with an integrated wavelength-tunable light source," Infrared Phys. Technol. **115**, 103705 (2021).

[172] J. B. Leen and A. O'Keefe, "Optical re-injection in cavity-enhanced absorption spectroscopy," Rev. Sci. Instrum. **85**(9), 093101 (2014).

[173] S. Maithani, A. Maity, and M. Pradhan, "A perspective on the evolving role of stable isotope analysis and the emergence of cavity enhanced spectroscopy as a potent tool," J. Anal. At. Spectrom. **36**(9), 1813–1825 (2021).

[174] K. E. Arledge, B. Uchoa, Y. Zou, and B. Weng, "Topological sensing with photonic arrays of resonant circular waveguides," Phys. Rev. Res. **3**(3), 033106 (2021).

[175] W. Bogaerts, P. De Heyn, T. Van Vaerenbergh, K. De Vos, S. Kumar Selvaraja, T. Claes, P. Dumon, P. Bienstman, D. Van Thourhout, and R. Baets, "Silicon microring resonators," Laser Photonics Rev. **6**(1), 47–73 (2012).

[176] Y. Chen, H. Lin, J. Hu, and M. Li, "Heterogeneously integrated silicon photonics for the mid-infrared and spectroscopic sensing," ACS Nano **8**(7), 6955–6961 (2014).

[177] H. Lin, Y. Xiang, L. Li, K. McLaughlin, Y. Liu, Y. Chillakuru, E. Koontz, J. D. Musgraves, K. Richardson, C. Ni, and J. Hu, in *IEEE Photonics Society Summer Topical Meeting Series* (IEEE, Montreal, QC, Canada, 2014), pp. 61–62.

[178] J. Zhou, D. A. Husseini, J. Li, Z. Lin, S. Sukhishvili, G. L. Coté, R. Gutierrez-Osuna, and P. T. Lin, "Mid-infrared serial microring resonator array for real-time detection of vapor-phase volatile organic compounds," Anal. Chem. **94**(31), 11008–11015 (2022).

[179] B. Troia, A. Z. Khokhar, M. Nedeljkovic, J. S. Penades, V. M. N. Passaro, and G. Z. Mashanovich, "Cascade-coupled racetrack resonators based on the Vernier effect in the mid-infrared," Opt. Express **22**(20), 23990 (2014).

[180] Y. Chang, B. Dong, Y. Ma, J. Wei, Z. Ren, and C. Lee, "Vernier effect-based tunable mid-infrared sensor using silicon-on-insulator cascaded rings," Opt. Express **28**(5), 6251 (2020).

[181] J. T. Robinson, L. Chen, and M. Lipson, "On-chip gas detection in silicon optical microcavities," Opt. Express **16**(6), 4296–4301 (2008).

[182] Z. Wang, X. Xu, D. Fan, Y. Wang, and R. T. Chen, "High quality factor subwavelength grating waveguide micro-ring resonator based on trapezoidal silicon pillars," Opt. Lett. **41**(14), 3375–3378 (2016).

[183] A. Vasiliev, A. Malik, M. Muneeb, B. Kuyken, R. Baets, and G. Roelkens, "On-chip mid-infrared photothermal spectroscopy using suspended silicon-on-insulator microring resonators," ACS Sens. **1**(11), 1301–1307 (2016).

[184] W.-C. Lai, S. Chakravarty, Y. Zou, and R. T. Chen, "Multiplexed detection of xylene and trichloroethylene in water by photonic crystal absorption spectroscopy," Opt. Lett. **38**(19), 3799 (2013).

[185] Y. Zou, S. Chakravarty, P. Wray, and R. T. Chen, "Experimental demonstration of propagation characteristics of mid-infrared photonic crystal waveguides in silicon-on-sapphire," Opt. Express **23**(5), 6965 (2015).

[186] Y. Zou, S. Chakravarty, L. Zhu, and R. T. Chen, "The role of group index engineering in series-connected photonic crystal microcavities for high density sensor microarrays," Appl. Phys. Lett. **104**(14), 141103 (2014).

[187] C. Kraeh, J. L. Martinez-Hurtado, A. Popescu, H. Hedler, and J. J. Finley, "Slow light enhanced gas sensing in photonic crystals," Opt. Mater. **76**, 106–110 (2018).

[188] W.-C. Lai, S. Chakravarty, X. Wang, C. Lin, and R. T. Chen, "On-chip methane sensing by near-IR absorption signatures in a photonic crystal slot waveguide," Opt. Lett. **36**(6), 984 (2011).

[189] Y. Zou, S. Chakravarty, P. Wray, and R. T. Chen, "Mid-infrared holey and slotted photonic crystal waveguides in silicon-on-sapphire for chemical warfare simulant detection," Sens. Actuators, B **221**, 1094–1103 (2015).

[190] A. Rostamian, E. Madadi-Kandjani, H. Dalir, V. J. Sorger, and R. T. Chen, "Towards lab-on-chip ultrasensitive ethanol detection using photonic crystal waveguide operating in the mid-infrared," Nanophotonics **10**(6), 1675–1682 (2021).

[191] R. Shankar, R. Leijssen, I. Bulu, and M. Lončar, "Mid-infrared photonic crystal cavities in silicon," Opt. Express **19**(6), 5579 (2011).

[192] Y. Zou, S. Chakravarty, and R. T. Chen, "Mid-infrared silicon-on-sapphire waveguide coupled photonic crystal microcavities," Appl. Phys. Lett. **107**(8), 081109 (2015).

[193] L. Kassa-Baghdouche, "High-sensitivity spectroscopic gas sensor using optimized H1 photonic crystal microcavities," J. Opt. Soc. Am. B **37**(11), A277 (2020).

[194] W.-C. Lai, S. Chakravarty, X. Wang, C. Lin, and R. T. Chen, "Photonic crystal slot waveguide absorption spectrometer for on-chip near-infrared spectroscopy of xylene in water," Appl. Phys. Lett. **98**(2), 023304 (2011).

[195] A. Hartstein, J. R. Kirtley, and J. C. Tsang, "Enhancement of the infrared absorption from molecular monolayers with thin metal overlayers," Phys. Rev. Lett. **45**(3), 201–204 (1980).

[196] S. A. Johnson, N.-H. Pham, V. J. Novick, and V. A. Maroni, "Application of surface-enhanced infrared absorption spectroscopy as a sensor for volatile organic compounds," Appl. Spectrosc. **51**(9), 1423–1426 (1997).

[197] J.-F. Masson, "Portable and field-deployed surface plasmon resonance and plasmonic sensors," Analyst **145**(11), 3776–3800 (2020).

[198] J. Zhang, L. Zhang, and W. Xu, "Surface plasmon polaritons: Physics and applications," J. Phys. D **45**(11), 113001 (2012).

[199] H.-L. Wang, E.-M. You, R. Panneerselvam, S.-Y. Ding, and Z.-Q. Tian, "Advances of surface-enhanced Raman and IR spectroscopies: From nano/microstructures to macro-optical design," Light **10**(1), 161 (2021).

[200] A. Asghari, C. Wang, K. M. Yoo *et al.*, "Fast, accurate, point-of-care COVID-19 pandemic diagnosis enabled through advanced lab-on-chip optical biosensors: Opportunities and challenges," Appl. Phys. Rev. **8**(3), 031313 (2021).

[201] A. Monkawa, T. Nakagawa, H. Sugimori, E. Kazawa, K. Sibamoto, T. Takei, and M. Haruta, "With high sensitivity and with wide-dynamic-range localized surface-plasmon resonance sensor for volatile organic compounds," Sens. Actuators, B **196**, 1–9 (2014).

[202] A. B. Ayoub and M. A. Swillam, "Silicon plasmonics on-chip mid-IR gas sensor," IEEE Photonics Technol. Lett. **30**(10), 931–934 (2018).

[203] Y. Luo, M. Chamanzar, A. Apuzzo, R. Salas-Montiel, K. N. Nguyen, S. Blaize, and A. Adibi, "On-chip hybrid photonic–plasmonic light concentrator for nanofocusing in an integrated silicon photonics platform," Nano Lett. **15**(2), 849–856 (2015).

[204] C. Chen, D. A. Mohr, H.-K. Choi, D. Yoo, M. Li, and S.-H. Oh, "Waveguide-integrated compact plasmonic resonators for on-chip mid-infrared laser spectroscopy," Nano Lett. **18**(12), 7601–7608 (2018).

[205] B. Schwarz, P. Reininger, D. Ristanić, H. Detz, A. M. Andrews, W. Schrenk, and G. Strasser, "Monolithically integrated mid-infrared lab-on-a-chip using plasmonics and quantum cascade structures," Nat. Commun **5**(1), 4085 (2014).

[206] M. Pi, C. Zheng, J. Ji, H. Zhao, Z. Peng, J. Lang, L. Liang, Y. Zhang, Y. Wang, and F. K. Tittel, "Surface-enhanced infrared absorption spectroscopic chalcogenide waveguide sensor using a silver island film," ACS Appl. Mater. Interfaces **13**(27), 32555–32563 (2021).

[207] H. Zhou, D. Li, X. Hui, and X. Mu, "Infrared metamaterial for surface-enhanced infrared absorption spectroscopy: Pushing the frontier of ultrasensitive on-chip sensing," Int. J. Optomechatronics **15**(1), 97–119 (2021).

[208] L. Dong, X. Yang, C. Zhang, B. Cerjan, L. Zhou, M. L. Tseng, Y. Zhang, A. Alabastri, P. Nordlander, and N. J. Halas, "Nanogapped Au antennas for ultrasensitive surface-enhanced infrared absorption spectroscopy," Nano Lett. **17**(9), 5768–5774 (2017).

[209] L. V. Brown, X. Yang, K. Zhao, B. Y. Zheng, P. Nordlander, and N. J. Halas, "Fan-shaped gold nanoantennas above reflective substrates for surface-enhanced infrared absorption (SEIRA)," Nano Lett. **15**(2), 1272–1280 (2015).

[210] Z. Ren, Z. Zhang, J. Wei, B. Dong, and C. Lee, "Wavelength-multiplexed hook nanoantennas for machine learning enabled mid-infrared spectroscopy," Nat. Commun. **13**(1), 3859 (2022).

[211] N. Liu, M. Mesch, T. Weiss, M. Hentschel, and H. Giessen, "Infrared perfect absorber and its application as plasmonic sensor," Nano Lett. **10**(7), 2342–2348 (2010).

[212] S. Law, V. Podolskiy, and D. Wasserman, "Towards nano-scale photonics with micro-scale photons: The opportunities and challenges of mid-infrared plasmonics," Nanophotonics **2**(2), 103–130 (2013).

[213] R. Stanley, "Plasmonics in the mid-infrared," Nat. Photonics **6**(7), 409–411 (2012).

[214] P. Fehlen, G. Thomas, F. Gonzalez-Posada, J. Guise, F. Rusconi, L. Cerutti, T. Taliercio, and D. Spitzer, "Gas sensing of organophosphorous compounds with III–V semiconductor plasmonics," Sens. Actuators, B **376**, 132987 (2023).

[215] R. Jannesari, G. Pühringer, T. Grille, and B. Jakoby, in IEEE Sensors, 2019.

[216] Y. Zhong, S. D. Malagari, T. Hamilton, and D. Wasserman, "Review of mid-infrared plasmonic materials," J. Nanophotonics **9**(1), 093791 (2015).

[217] L. Zundel and A. Manjavacas, "Spatially resolved optical sensing using graphene nanodisk arrays," ACS Photonics **4**(7), 1831–1838 (2017).

[218] X. Yang, Z. Sun, T. Low, H. Hu, X. Guo, F. J. García de Abajo, P. Avouris, and Q. Dai, "Nanomaterial-based plasmon-enhanced infrared spectroscopy," Adv. Mater. **30**(20), 1704896 (2018).

[219] D. B. Farmer, P. Avouris, Y. Li, T. F. Heinz, and S.-J. Han, "Ultrasensitive plasmonic detection of molecules with graphene," ACS Photonics **3**(4), 553–557 (2016).

[220] N. Bareza, Jr., K. K. Gopalan, R. Alani, B. Paulillo, and V. Pruneri, "Mid-infrared gas sensing using graphene plasmons tuned by reversible chemical doping," ACS Photonics **7**(4), 879–884 (2020).

[221] H. Hu, X. Yang, X. Guo, K. Khaliji, S. R. Biswas, F. J. García De Abajo, T. Low, Z. Sun, and Q. Dai, "Gas identification with graphene plasmons," Nat. Commun. **10**(1), 1131 (2019).

[222] L. E. Kreno, J. T. Hupp, and R. P. Van Duyne, "Metal−organic framework thin film for enhanced localized surface plasmon resonance gas sensing," Anal. Chem. **82**(19), 8042–8046 (2010).

[223] J. Tao, X. Wang, T. Sun, H. Cai, Y. Wang, T. Lin, D. Fu, L. L. Y. Ting, Y. Gu, and D. Zhao, "Hybrid photonic cavity with metal-organic framework coatings for the ultra-sensitive detection of volatile organic compounds with high immunity to humidity," Sci. Rep. **7**(1), 41640 (2017).

[224] H. Zhou, X. Hui, D. Li, D. Hu, X. Chen, X. He, L. Gao, H. Huang, C. Lee, and X. Mu, "Metal–organic framework-surface-enhanced infrared absorption platform enables simultaneous on-chip sensing of greenhouse gases," Adv. Sci. **7**(20), 2001173 (2020).

[225] R. Wang, P. Täschler, Z. Wang, E. Gini, M. Beck, and J. Faist, "Monolithic integration of mid-infrared quantum cascade lasers and frequency combs with passive waveguides," ACS Photonics **9**(2), 426–431 (2022).

[226] T.-Y. Chang, Y. Chen, D.-I. Luo, J.-X. Li, P.-L. Chen, S. Lee, Z. Fang, W.-Q. Li, Y.-Y. Zhang, M. Li, A. Majumdar, and C.-H. Liu, "Black phosphorus mid-infrared light-emitting diodes integrated with silicon photonic waveguides," Nano Lett. **20**(9), 6824–6830 (2020).

[227] A. Lochbaum, Y. Fedoryshyn, A. Dorodnyy, U. Koch, C. Hafner, and J. Leuthold, "On-chip narrowband thermal emitter for mid-IR optical gas sensing," ACS Photonics **4**(6), 1371–1380 (2017).

[228] A. L. Gaeta, M. Lipson, and T. J. Kippenberg, "Photonic-chip-based frequency combs," Nat. Photonics **13**(3), 158–169 (2019).

[229] H. Tran, C. G. Littlejohns, D. J. Thomson, T. Pham, A. Ghetmiri, A. Mosleh, J. Margetis, J. Tolle, G. Z. Mashanovich, W. Du, B. Li, M. Mortazavi, and S.-Q. Yu, "Study of GeSn mid-infrared photodetectors for high frequency applications," Front. Mater. **6**, 278 (2019).

[230] S. Mauthe, Y. Baumgartner, M. Sousa, Q. Ding, M. D. Rossell, A. Schenk, L. Czornomaz, and K. E. Moselund, "High-speed III-V nanowire photodetector monolithically integrated on Si," Nat. Commun. **11**(1), 4565 (2020).

[231] Z. Han, V. Singh, D. Kita, C. Monmeyran, P. Becla, P. Su, J. Li, X. Huang, L. C. Kimerling, J. Hu, K. Richardson, D. T. H. Tan, and A. Agarwal, "On-chip chalcogenide glass waveguide-integrated mid-infrared PbTe detectors," Appl. Phys. Lett. **109**(7), 071111 (2016).

[232] H. Lin, Y. Song, Y. Huang, D. Kita, S. Deckoff-Jones, K. Wang, L. Li, J. Li, H. Zheng, Z. Luo, H. Wang, S. Novak, A. Yadav, C.-C. Huang, R.-J. Shiue, D. Englund, T. Gu, D. Hewak, K. Richardson, J. Kong, and J. Hu, "Chalcogenide glass-on-graphene photonics," Nat. Photonics **11**(12), 798–805 (2017).

[233] X. Tan, H. Zhang, J. Li, H. Wan, Q. Guo, H. Zhu, H. Liu, and F. Yi, "Non-dispersive infrared multi-gas sensing via nanoantenna integrated narrowband detectors," Nat. Commun. **11**(1), 5245 (2020).

[234] Y. Han, H. Park, J. Bowers, and K. M. Lau, "Recent advances in light sources on silicon," Adv. Opt. Photonics **14**(3), 404–454 (2022).

[235] A. Malik, A. Spott, E. J. Stanton, J. D. Peters, J. D. Kirch, L. J. Mawst, D. Botez, J. R. Meyer, and J. E. Bowers, "Integration of mid-infrared light sources on silicon-based waveguide platforms in 3.5–4.7 μm wavelength range," IEEE J. Sel. Top. Quantum Electron. **25**(6), 1–9 (2019).

[236] E. Tournié, L. Monge Bartolome, M. Rio Calvo, Z. Loghmari, D. A. Díaz-Thomas, R. Teissier, A. N. Baranov, L. Cerutti, and J.-B. Rodriguez, "Mid-infrared III–V semiconductor lasers epitaxially grown on Si substrates," Light **11**(1), 165 (2022).

[237] J. Haas and B. Mizaikoff, "Advances in mid-infrared spectroscopy for chemical analysis," Annu. Rev. Anal. Chem. **9**(1), 45–68 (2016).

[238]B. A. Matveev, G. A. Gavrilov, V. V. Evstropov, N. V. Zotova, S. A. Karandashov, G. Sotnikova, N. M. Stus', G. N. Talalakin, and J. Malinen, "Mid-infrared (3–5 μm) LEDs as sources for gas and liquid sensors," Sens. Actuators, B **39**(1), 339–343 (1997).

[239]D. Grassani, E. Tagkoudi, H. Guo, C. Herkommer, F. Yang, T. J. Kippenberg, and C.-S. Brès, "Mid infrared gas spectroscopy using efficient fiber laser driven photonic chip-based supercontinuum," Nat. Commun. **10**(1), 1553 (2019).

[240]A. Dutt, C. Joshi, X. Ji, J. Cardenas, Y. Okawachi, K. Luke, A. L. Gaeta, and M. Lipson, "On-chip dual-comb source for spectroscopy," Sci. Adv. **4**(3), e1701858 (2018).

[241]L. A. Sterczewski, M. Fradet, C. Frez, S. Forouhar, and M. Bagheri, "Battery-operated mid-infrared diode laser frequency combs," Laser Photonics Rev. **17**(1), 2200224 (2023).

[242]C. Xiang, J. Liu, J. Guo, L. Chang, R. N. Wang, W. Weng, J. Peters, W. Xie, Z. Zhang, J. Riemensberger, J. Selvidge, T. J. Kippenberg, and J. E. Bowers, "Laser soliton microcombs heterogeneously integrated on silicon," Science **373**(6550), 99–103 (2021).

[243]N. Na, Y.-C. Lu, Y.-H. Liu, P.-W. Chen, Y.-C. Lai, Y.-R. Lin, C.-C. Lin, T. Shia, C.-H. Cheng, P.-Y. Huang, L. Wang, and S.-L. Chen, in *IEEE Silicon Photonics Conference (SiPhotonics)* (IEEE, Washington, DC, 2023).

[244]H. Tran, T. Pham, J. Margetis, Y. Zhou, W. Dou, P. C. Grant, J. M. Grant, S. Al-Kabi, G. Sun, R. A. Soref, J. Tolle, Y.-H. Zhang, W. Du, B. Li, M. Mortazavi, and S.-Q. Yu, "Si-based GeSn photodetectors toward mid-infrared imaging applications," ACS Photonics **6**(11), 2807–2815 (2019).

[245]J. Huang, Z. Dai, Z. Shen, Z. Wang, Z. Zhou, Z. Wang, B. Peng, W. Liu, and B. Chen, "High-speed mid-wave infrared InAs/InAsSb superlattice uni-traveling carrier photodetectors with different absorber doping," IEEE Trans. Electron Devices **69**(12), 6890–6896 (2022).

[246]M. Muneeb, A. Vasiliev, A. Ruocco, A. Malik, H. Chen, M. Nedeljkovic, J. S. Penades, L. Cerutti, J. B. Rodriguez, G. Z. Mashanovich, M. K. Smit, E. Tourni, and G. Roelkens, "III-V-on-silicon integrated micro-spectrometer for the 3 μm wavelength range," Opt. Express **24**(9), 9465 (2016).

[247]W. D. Lawson, S. Nielsen, E. H. Putley, and A. S. Young, "Preparation and properties of HgTe and mixed crystals of HgTe-CdTe," J. Phys. Chem. Solids **9**(3), 325–329 (1959).

[248]B. Chen, Y. Chen, and Z. Deng, "Recent advances in high speed photodetectors for eSWIR/MWIR/LWIR applications," Photonics **8**(1), 14 (2021).

[249]B. Weng, J. Qiu, Z. Yuan, P. R. Larson, G. W. Strout, and Z. Shi, "Responsivity enhancement of mid-infrared PbSe detectors using CaF_2 nano-structured anti-reflective coatings," Appl. Phys. Lett. **104**(2), 021109 (2014).

[250]B. Weng, J. Qiu, L. Zhao, C. Chang, and Z. Shi, "CdS/PbSe heterojunction for high temperature mid-infrared photovoltaic detector applications," Appl. Phys. Lett. **104**(12), 121111 (2014).

[251]B. Weng, J. Qiu, L. Zhao, Z. Yuan, C. Chang, and Z. Shi, "Recent development on the uncooled mid-infrared PbSe detectors with high detectivity," Proc. SPIE **8993**, 899311 (2013).

[252]J. Wu, N. Wang, X. Yan, and H. Wang, "Emerging low-dimensional materials for mid-infrared detection," Nano Res. **14**(6), 1863–1877 (2021).

[253]Y. Ma, Y. Chang, B. Dong, J. Wei, W. Liu, and C. Lee, "Heterogeneously integrated graphene/silicon/halide waveguide photodetectors toward chip-scale zero-bias long-wave infrared spectroscopic sensing," ACS Nano **15**(6), 10084–10094 (2021).

[254]S. Yuan, D. Naveh, K. Watanabe, T. Taniguchi, and F. Xia, "A wavelength-scale black phosphorus spectrometer," Nat. Photonics **15**(8), 601–607 (2021).

[255]Z. Yang, T. Albrow-Owen, W. Cai, and T. Hasan, "Miniaturization of optical spectrometers," Science **371**(6528), eabe0722 (2021).

[256]J. Brouckaert, W. Bogaerts, P. Dumon, D. Van Thourhout, and R. Baets, "Planar concave grating demultiplexer fabricated on a nanophotonic silicon-on-insulator platform," J. Lightwave Technol. **25**(5), 1269–1275 (2007).

[257]P. Pottier, M. J. Strain, and M. Packirisamy, "Integrated microspectrometer with elliptical Bragg mirror enhanced diffraction grating on silicon on insulator," ACS Photonics **1**(5), 430–436 (2014).

[258]L. Zhang, M. Zhang, T. Chen, D. Liu, S. Hong, and D. Dai, "Ultrahigh-resolution on-chip spectrometer with silicon photonic resonators," Opto-Electron. Adv. **5**(7), 210100 (2022).

[259]H. Xu, Y. Qin, G. Hu, and H. K. Tsang, "Breaking the resolution-bandwidth limit of chip-scale spectrometry by harnessing a dispersion-engineered photonic molecule," Light **12**(1), 64 (2023).

[260]W. Hadibrata, H. Noh, H. Wei, S. Krishnaswamy, and K. Aydin, "Compact, high-resolution inverse-designed on-chip spectrometer based on tailored disorder modes," Laser Photonics Rev. **15**(9), 2000556 (2021).

[261]B. Redding, S. F. Liew, R. Sarma, and H. Cao, "Compact spectrometer based on a disordered photonic chip," Nat. Photonics **7**(9), 746–751 (2013).

[262]T. Liu and A. Fiore, "Designing open channels in random scattering media for on-chip spectrometers," Optica **7**(8), 934 (2020).

[263]A. Li and Y. Fainman, "On-chip spectrometers using stratified waveguide filters," Nat. Commun. **12**(1), 2704 (2021).

[264]T. Lin, A. Dutt, C. Joshi, C. T. Phare, Y. Okawachi, A. L. Gaeta, and M. Lipson, "Broadband ultrahigh-resolution chip-scale scanning soliton dual-comb spectroscopy," arXiv:2001.00869 (2020).